Impact of electric fields on the alignment of clay particles

René C. Castberg

Thesis submitted for the degree of PhD
Faculty of Mathematics and Natural Sciences - Department of Physics
University of Oslo, Norway

March 2014

To Louisa and Gunnar

Acknowledgements

Preface

This work presents experimental work done in the AMKS group at the University of Oslo between 2009 and 2014 under the Supervision of Knut Jørgen Måløy as my main supervisor with co-supervision from Jon Otto Fossum and Eirik Grude Flekkøy. The work was funded by the Norwegian Research Council Nanomat programme 182075 with some additional funding from the group and the University.

The work is primarily based on the orientation and ordering of particles on application of electric fields.

Most of the work was performed either in K. J. Måløy's laboratories at Oslo University or at NTNU Trondheim, in J. O. Fossum's laboratories. In addition some X-ray studies were done at the European Synchrotron radiation facility in Grenoble, France.

Contents

List of Papers

1. **Electric Field nematic alignment of fluorohectorite clay particles in oligomeric matrices**
   Z. Rozynek, R. C. Castberg, A. Mikkelsen, J. O. Fossum.
   J. Matter. Res. **28**, 1349-1355, (2013)

2. **Clay alignment in electric fields**
   R. C. Castberg, Z. Rozynek, J. O. Fossum, K.J. Måløy, P. Dommersnes and E. G. Flekkøy
   Rev. Cub. Fis. **29**, 1E28, (2012)

3. **Dipolar ordering of clay particles in various carrier fluids.**
   Z. Rozynek, H. Maurøy, R. C. Castberg, K. D. Knudsen and J O Fossum
   Rev. Cub. Fis. **29**, 1E37, (2012)

4. **Active structuring of colloidal armour on liquid drops.**
   P. Dommersnes, Z. Rozynek, A. Mikkelsen, R. Castberg, K. Hersvik and J. O. Fossum.
   Nat. Comm. **4**, 2066, (2013)

5. **Insight into the alignment of clay platelets in silicone oil**
   R. C. Castberg, Z. Rozynek, P. Dommersnes, E. G. Flekkøy, K.J. Måløy, and J. O. Fossum,
   To be submitted

My contributions to the manuscripts

Electric field nematic alignment of fluorohectorite clay particles in oligomeric matrices

-Involvement in all of the experiments performed at the ESRF facility, Grenoble

-Involvement in most of the performed experiments

-Involvement in initial data analysis and presentation of results

-Involvement in editing and revision of article

Clay alignment in electric fields

-Involvement in all performed experiments

-Main contributor to data analysis and contributor to presentation of results

-Involvement in writing, editing and corrections of the proceeding

-Handling submission and correspondence with journal

Dipolar ordering of clay particles in various carrier fluids

-Involvement in some of the performed experiments

-Involvement in analysis and presentation of part of the results

-Involvement editing and revision of the manuscript

Active structuring of colloidal armour on liquid drops

-Performed all the presented experiments on the "pupil effect", i.e. Figure 6 in the paper and also involvement in some of the other experiments

-Involvement in analysis of data and presentation of results

-Involvement in writing and discussion towards finalization of article

Insight into the alignment of clay platelets in silicone oil

-Involvement in all performed experiments

-Performed data analysis and presentation of results

-Performed writing, editing and corrections of the proceeding

-I will be handling the submission and correspondence with journal

Chapter 1

Introduction

As our technology develops we are more reliant on smaller structures and more complicated materials. As a result of this, we require materials which are to some extent able to self organise. A few examples of these advances are nanocomposites made by adding nanoparticles to a material to enhance its properties; clutches using electrorheological fluids to react faster; or as a way of a creating a self assembled surface using patchy particles[1].

This work will primarily concentrate on aligning particles using an electric field, but previous studies have aligned clay particles using different methods, namely planar shearing[2], extrusion[3], gravity[4] and magnetic fields[5].

Another area of technology which is developing rapidly is in the use of electrorheological (ER) fluids. These are fluids that can change their viscosities almost instantaneously, typically in the order of milliseconds. Modern cars already use magnetorheological dampers[6] and successful tests have been made with electrorheological dampers[7]. When used in adaptive suspensions they can react to road conditions quickly, typically within $10\,\text{ms}$. ER fluids have also been used in brakes and clutches, and it is expected that there will be many new technologies based on ER fluids in the future[8].

Recently methods of producing a self assembled lattice kagome structure (an arrangement of intertwined triangles), was shown using a bottom up design with patchy colloids[1]. It is expected that these patchy colloids (colloidal particle with attractive spots on the surface) will become an elementary building block of the future. Patchy colloidosomes have already been used as building blocks to produce three dimensional shapes ranging from cubes to tripods[9]. We expect that as the variety of these particles increases the number of possible constructed shapes will increase. This is an exciting prospect for the future. In Paper 4, we have presented one method which should allow these types of particles to be created by using an electric field to induce an electro-hydrodynamic flow inside a drop. There are many methods to produce these particles in this rapidly expanding area of research, for example using "Pickering emulsions"[10], microfluidics[11] and plasma polymerization[12].

Nanocomposites are made in a similar way to modern composites like glass fibre, where a material (polymer) is mixed with filler (glass fibre), only in this case the filler is made from nanoparticles. The fillers typically enhance the material by changing its' physical properties. In 1991 Toyota[13] introduced a nano composite using a clay mineral and nylon-6, with other manufacturers following suite soon after. They reported a significant improvement in a wide range of mechanical properties by adding a small amount of clay mineral (5wt.%) to the ny-
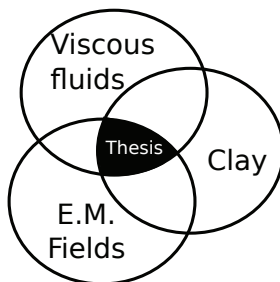
Figure 1.1: Main areas of study.

lon. One of the reasons for the improvement is that the clay that is introduced can be made to both intercalate and exfoliate[14] in the polymer. Combined with their large width/thickness (10-1,000) ratio, this means that the total interface area between the polymer and clay is much greater than for conventional composites like glass fibre[15]. It has also been shown that materials made with a low weight percent (2wt.%) clay filler have a gas permeability 50% lower[16] than those without. This is due to the increased tortuosity, i.e. the increased path length the gas has to follow in order to pass through the material. It has been suggested that the permeability of a material could be controlled by the orientation of the particles used in the filler[15]. Similarly, the elasticity of a magnetisable polymeric material can be increased by aligning the particles in a uniform magnetic field [17].

The work presented in this thesis is based on initial studies done by Z. Rozynek on the alignment of clay particles in electric fields[18] and by K. Hersvik on oil droplet deformation[19], as well as studies performed by A. Mikkelsen[20] and K. Kjerstad[21]. All the projects have been further developed in collaboration with the other co-authors in the papers presented.

The experiments were carried out at the University of Oslo and at NTNU in Trondheim, and WAXS measurements were made in the lab in Trondheim and the ESRF facility in Grenoble, France.

This work is split in three main projects; rotation of clay particles, electric alignment of clay particles in paraffin, and active structuring of colloidal armour on liquid drops. All three of the projects rely on three important components; an electric field to align the particles, a viscous fluid to suspend the particles, and a reaction between the particle and the applied field (Figure 1.1).

1.1 Electrorheological fluids

Fluids have a rheological property called the viscosity. It is defined as the ratio of the shearing stress to the velocity gradient. Generally the viscosity will depend on the composition of the fluid and the temperature. Electrorheological fluids can change their apparent viscosity when an electrical field is applied. Typically, an insulating fluid containing particles with a size range of around $0.04\,\mu$m to $60\,\mu$m [22] can change its viscosity by several orders of magnitude within milliseconds and return to their previous state equally quickly. The dispersed phase can be made up of many different non-conductive materials, ranging from cornstarch to polymers. The

dispersing phase is often a liquid with a very low conductivity and a low dielectric constant, resulting in a high dielectric contrast with the particles.

The method by which the clay particles form an electrorheological fluid can be split into four stages[23], see Figure 1.2. In this work we will be primarily concerned with the first two.
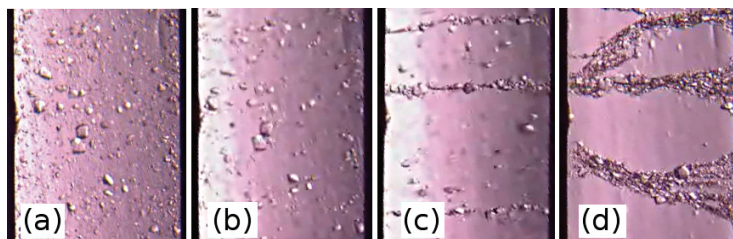
Figure 1.2: Four stages of chain formation, (a) polarisation when electric field is applied, (b) rotation and alignment, (c) onset of chain formation, (d) chain coarsening. Experiment performed by Z. Rozynek at NTNU.

Polarisation: When the electric field is applied there will be an immediate polarisation of the clay particle. This is a process with an approximate time scale of 10^{-5} to 10^{-7} seconds. The mechanisms involved in this process are not well understood but can be due to the polarisation of either the intercalated water or cations.

Rotation and alignment: Particles align with their major axis parallel to the E-field. The time for this to occur is dependent on the viscosity of the carrier fluid and strength of the applied electric field. This process takes on the order of 10^{-3} to 10^1 seconds. This stage has some overlap with the next stage.

Chain formation: Particles will start to form chains, typically after 10^{-1} to 10^1 seconds (depending on particle concentration) and time taken to form chains is proportional to the electric field strength. Most particles will have aligned in this stage.

Chain coarsening: Chains will start to merge, a process that may take longer than the single chain formation. Further alignment will be hindered due to other particles physically blocking further rotation.

1.2 Materials

1.2.1 Clay minerals

In this work various clay minerals have been used and therefore we should define what is meant by this term. According to the Joint nomenclature committees "Clay minerals are a class of hydrated phyllosilicates that make up the fine-grained fraction of rocks, sediments and soils, giving the plasticity to clay, hardening on drying or firing"[24]. This definition is in contrast to the definition of clay, "a naturally occurring material composed primarily of fine-grained minerals, which is generally plastic at appropriate water contents and will harden with (sic)

dried or fired" [24], does not define the size of the particle or the requirement that the material is naturally occurring. For this reason we will be referring to clay minerals whenever we refer to clay as this encompasses both synthetic and naturally occurring phyllosilicates.

Clay minerals can be classified into two distinct classes, 1:1, and 2:1 depending on the layering structure. The first number indicates the number of hydroxide octahedral sheets, and the second indicates the number of tetrahedral silica sheets (see Figure 1.3 for the structure). A 1:1 clay particle is made of repeated layers of one tetrahedral sheet linked to an octahedral sheet with an oxygen atom, whilst a 2:1 clay particle is made up of repeated layers of an octahedral sheet sandwiched between two tetrahedral sheets. Clays are often viewed as a good model for layered and soft materials as they are well characterized, have a well defined size and can be monodisperse (laponite), in addition to which they can be intercalated with molecules allowing you to change their properties[25]. In chapter 2 we worked with 2:1 clays, fluorohectorite and vermiculite, whilst in the chapter 3 we used fluorohectorite, and for chapter 4 we primarily used fluorohectorite, but did some experiments using laponite, montmorillonite, vermiculite, kaolinite, halloysite and quickclay. A brief description of each minerals properties is detailed below.

Fluorohectorite

Fluorohectorite is part of the smectite group of clay minerals, which have a 2:1 structure [26](see Figure 1.3), a sheet of octahedral edge sharing aluminium hydroxide sandwiched between two sheets of corner sharing tetrahedral silica. Fluorohectorite has an isomorphous substitution where a fraction of the Mg^{2+} is replaced with Li^+ resulting in a net negative charge of $1.2e^-$ per unit cell.

The negative charge is balanced out by a shared counter ion located between the lamellar sheets in the galleries and on the surfaces. Fluorohectorite has a general formula $M^{1.2+}[(Mg_{4.8}Li_{1.2})F_4Si_8O_{20}]^{1.2-}$, where M is the charge balancing ion. The charge balancing ion can be exchanged with another ion, for example Li^+ or Na^+

These clays can have an intercalated layer of water so that the more water that is present the larger the separation between the layers will be. In the case of Li^+ and Na^+ fluorohectorite the amount of water in between these layers is defined by the interlayer spacing and is denoted as either 0, 1, (1.5), or 2 water layers[27] corresponding to a separation of approximately 10Å, 12.5Å, (14Å), 15.5Å[28, 29]. The numbers in parentheses are relevant only for the Lithium exchanged clay that has an intermediate state of 1.5 water layers. The number of water layers is dependent on both temperature and humidity[27, 30]. Under typical laboratory conditions we find a preference for a single water layer. With a single water layer the conductivity is around $500\,\mu S/m$[31], and rapidly increases as the water content is increased. From measurements made in the laboratory we found that the conductivity increases in a non-ohmic way as the field is increased.

Vermiculite

Vermiculite was used in two of the datasets in the rotation part of this work (chapters 2.2 and 2.4) and in the colloidal armoured drop experiments (chapter 4). This is a naturally occurring clay and also has a 2:1 layered structure but is not part of the smectite group. It fol-
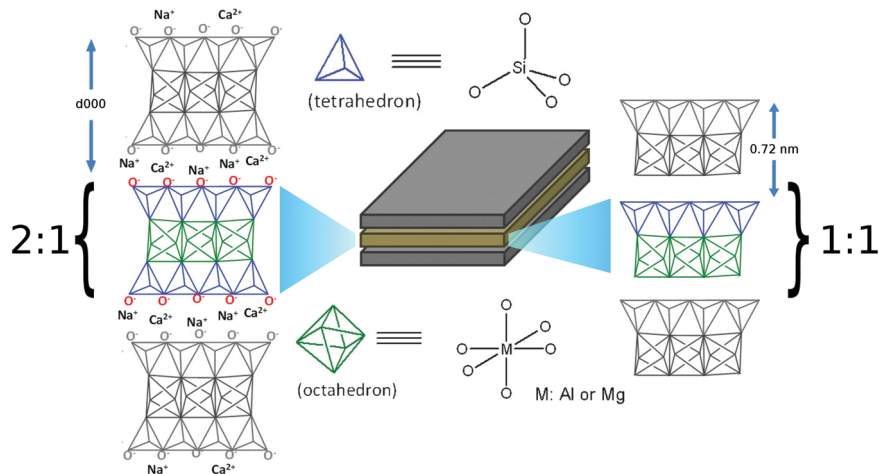
Figure 1.3: The layered structure of a 2:1 clay mineral (left) and a 1:1 clay mineral (right). Centre: three layers of what is usually described as a deck of cards. Each of the layers are made from either the structure on the left or right. (Adapted from reference [32])

lows the same layering structure as shown on the left side in Figure 1.3 and has a formula of $M^{1.24+}[(Mg_5Fe^{2+}_{1.2}Fe^{3+}_{0.8})Si_{5.5}Al_{2.5}O_{20}]^{1.24-}$ where the charge balancing cation (M) in its natural state has a typical composition of $Na_{0.21}K_{0.39}Mg_{0.19}Ca_{0.13}$. It has a charge of between $0.6 - 0.9$ e^- per unit cell[24]. In our case we used a partially substituted vermiculite where most of the cations were exchanged with sodium.

Laponite: Laponite is a synthetic 2:1 phyllosilicate, with an empirical chemical formula of $Na^{0.7+}[Si_8Mg_{5.5}Li_{0.3}O_{20}(OH)_4]^{0.7-}$. The positively charged Na^+ is an interlayer exchangeable cation balancing the negative charge of $0.7e^-$ per unit cell[33]. The laponite particles form discs that are $1\,nm$ thick and have an average diameter of $30\,nm$[34].

Montmorillonite Montmorillonite is a commercially available 2:1 smectite, having a net negative charge of $0.8e^-$[35] resulting from isomorphous substitutions in the octahedral layer. Its' chemical formula is $M_x(Al_{(2-y)}Mg_y)Si_4O_{10}(OH)_2 \cdot nH_2O$ per unit cell, where M is an intercalated cation balancing the charge.

Halloysite Halloysite is a natural 1:1 clay with an interlayer spacing of $1\,nm$ or $0.7\,nm$[24] when dehydrated. Its chemical composition is $Al_2Si_2O_5(OH)_4$, and has no net charge associated with it.

Kaolinite Kaolinite is a natural 1:1 clay with an interlayer spacing of $0.72\,nm$, with the chemical composition of $Al_2Si_2O_5(OH)_4$[24]. Unlike halloysite, kaolinite does not expand when subjected to humidity and in principle has no net charge.

Quick Clay This is a mixture of geologically natural clay. Typically consisting of 70 wt.% non-swelling clays (illite, chlorite and some kaolinite) and a few percent swelling clays (vermiculite and montmorillonite)[36]

1.2.2 Particle structures

The fluorohectorite clay used in chapter 2 has forms; powdered and aggregated platelets. The powdered clay consists milled particles , where the resulting particle diameters are approximately 1 µm to 60 µm. Each of these particles is made of multiple "deck of cards" like structures (Figure 1.4(c)) where each of the layers consists of two tetrahedral and one octahedral sheet. In the rest of this work we will refer to this as powdered clay.
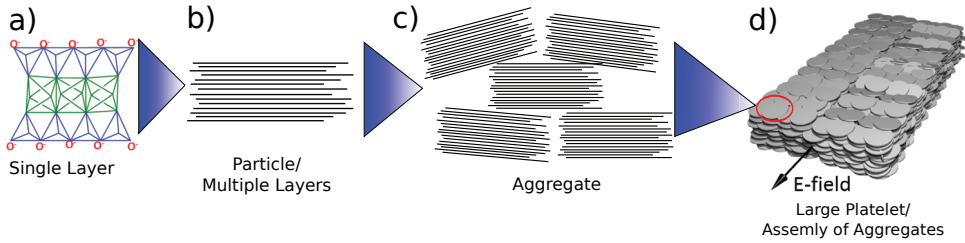
Figure 1.4: The layered structure of a 2:1 clay mineral (a) consisting of two tetrahedral sheets sandwiching one octahedral sheet. This can form what is commonly known as a deck of cards, typically 80-100 sheets (b). Aggregates of the deck of cards (b) can form the individual particles in powdered clay (c). When these are suspended in water and allowed to settle they create a structure as in the (d). (Adapted from [32] and [24]).

In order to construct a larger particle with which we could do repeated measurements we made platelets by allowing a suspension of powdered clay minerals to settle and dry. This creates sheets of fluorohectorite clay which could then be cut into the desired shapes. Each platelet then has all the particles stacked such that the stacking direction is perpendicular to the longest axis (see Figure 1.4(d)). We will be referring to this structure as large platelets in this work. For a detailed description see Paper 5.

1.2.3 Oils

This work used oils which are exposed to high electric fields and act as a medium to suspend the clay, polyethylene or glass spheres. Oils with various viscosities were used in chapter 2. In chapter 4 we required two oils with different conductivities (Castor oil and Silicone oil 100 cSt). A summary of the properties of the oils used herein is contained in Table 1.1.

Oil	Viscosity (cSt)	Density (kg/m^3)	Conductivity (pSm)	Dielectric constant (-)
Silicone 100cSt	100	964	<1	2.75
Silicone 200cSt	200	967	<1	2.75
Silicone 500cSt	500	970	<1	2.75
Silicone 1000cSt	1000	970	<1	2.76
Silicone 10000cSt	10000	971	<1	2.76
Castor oil	1000	961	45	4.7

Table 1.1: Oils and their viscosities as used in the experiments.

1.2.4 Measuring the small structures of clay

In order to ascertain the properties of the clay particles, we need to be able to measure the separation between the layers as this spacing is dependent on temperature and humidity. This is due to the intercalated water content and rearrangement of water in the clay galleries. These measurements can be made using Wide Angle X-ray Scattering (WAXS) which allows us to measure the interlayer spacing and obtain information on the orientation of the platelets. When X-rays are scattered elastically from a material the scattering vector $\mathbf{q}$ is defined as

$$\mathbf{q} = \mathbf{k_s} - \mathbf{k_i}, \tag{1.1}$$

where $\mathbf{k_s}$ and $\mathbf{k_i}$ are the propagation vectors of the scattered and incident beams. We can then find the magnitude of the scattering vector as:

$$q = |\mathbf{q}| = \frac{4\pi \sin \theta}{\lambda}. \tag{1.2}$$

Here 2θ is the angle of the incident beam with respect to the scattered beam and λ is the wavelength of incident beam.

Using Bragg's Law, which is valid for intensity maxima (Bragg peaks).

$$n\lambda = 2d \sin \theta, \tag{1.3}$$

we can find the spacing between the layers. Here n is the order of the reflection and d is the separation between two planes in a crystal. For the Bragg peak we can relate the absolute scattering vector q to the separation between the planes using $d = \frac{2\pi}{q}$.

As the system becomes more anisotropic the intensity of the Bragg pattern will also become more anisotropic, Figure 1.5(B,C). Scattering from an anisotropic material like this aggregate of particles (A) creates a 2D Bragg pattern as in (B). This can either be integrated radially(C) or azimuthally(D). Radial integration allows us to quantify the anisotropy while the azimuthal integration provides information on the interlayer spacing.

Integrating the 2D Bragg pattern radially over a narrow q-range, as defined by the width of the peak in Figure 1.5(D), we obtain a 1-D representation of the 2-D Bragg pattern (shown in Figure 1.5(C)) . This describes the intensity of the scattering as a function of the azimuthal angles as shown in Figure 1.5(C). In this figure we can see a clear anisotropy in the distribution along the azimuthal angle. In this case it is due to an applied external field, but it could also be created by a gravitational or magnetic field. In order to quantify the degree of anisotropy we can attempt to fit the data using a parametric function. One such function is the Maier-Saupe function, defined as $f(\phi)$ below[37]:

$$I_{2\theta}(\phi) \propto f(\alpha_{2\theta}(\phi)) \propto e^{m \cos^2 \alpha_{2\theta}(\phi)} \tag{1.4}$$

where $I_{2\theta}$ is the azimuthal scattering intensity (as shown in Figure 1.5(C)), ϕ is the azimuthal angle and m is the fitting parameter that corresponds to the degree of anisotropy. $\alpha_{2\theta}(\phi)$ is an angle relating to the particle geometry with respect to the incident X-ray beam and that of the crystallites that diffract the beam[37]. Fitting this relationship to the data in Figure 1.5 by a least
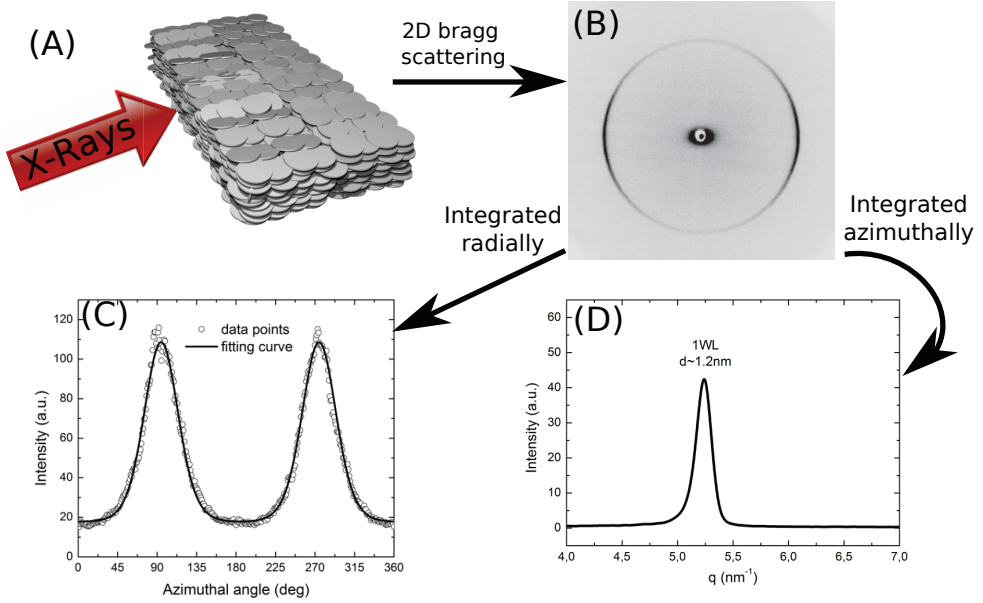
Figure 1.5: WAXS scattering from a sample of sodium fluorohectorite clay. Experiment and data analysis performed by Z. Rozynek.

squares regression, we obtain m, which relates the full width at half maximum to the degree of anisotropy.

We can define the nematic order parameter S_2[38] as

$$S_2 = \pi \int_0^{\pi/2} (3\cos^2\alpha - 1) f(\alpha)\sin\alpha \, d\alpha \tag{1.5}$$

where α is the same angle as defined in Eq. (1.4). For simplicity we have omited writing the subscript 2θ and the functional dependance of ϕ. This function has a range of $-\frac{1}{2}$ to 1, where a value of 1 indicates perfectly ordered platelet particles in the nematic configuration, a value of 0 states no orientational order and a value of $-\frac{1}{2}$ indicates perfectly ordered platelets in the anti-nematic configuration[18]. Although the Maier-Saupe function was intended for a system with completely different interaction energies, specifically liquid crystals, fitting it to the raw data results in good fits and still gives useful information. This is discussed in more detail in [37].

Chapter 2

Rotational alignment

During chain formation, one of the stages was called the rotation and alignment stage (Figure 1.2). In order to learn more about this stage we studied this process in detail.

Initial studies of the rotation of clay was done with two sizes of particles (as described in chapter 1.2.2):

- **Powdered sodium fluorohectorite**, for the initial studies.

- **Large sodium fluorohectorite platelets**, for the results presented in the Papers 2 and 5.

2.1   Initial studies

For the case of powered clay (section 1.2.2) in silicone oil, the particles we studied had a mean size of $30\,\mu$m and a size distribution of $11\,\mu$m to $66\,\mu$m (calculated from measurements of experimental data).

2.1.1   Experimental setup

Our initial studies were performed using powdered sodium fluorohectorite clay. The setup is shown in Figure 2.1(A). The first studies were done with a glass plate attached to the electrodes as seen in Figure 2.1(B). The glass plate attached to the bottom of the electrodes had the unfortunate side effect that the particle would settle onto the glass plate and the friction from the contact would slow the rotation rate. After removing the glass plate (Figure 2.1(C)) and leaving the liquid hanging between the two electrodes by surface tension alone we no longer observed any sticking.

The experiments were filmed using an microscope with magnification of between 5x to 20x. On the microscope a Photron Fastcam Ultima APX was mounted after a 10x lens. The frame rate used on the camera varied depending on the size of the electric field, and was between 50 and 2000 frames per second for the lowest and highest electric fields, respectively.

2.1.2   Solutions to issues encountered with powdered clay

We had some issues with this experimental procedure, which are outlined below along with our solutions.
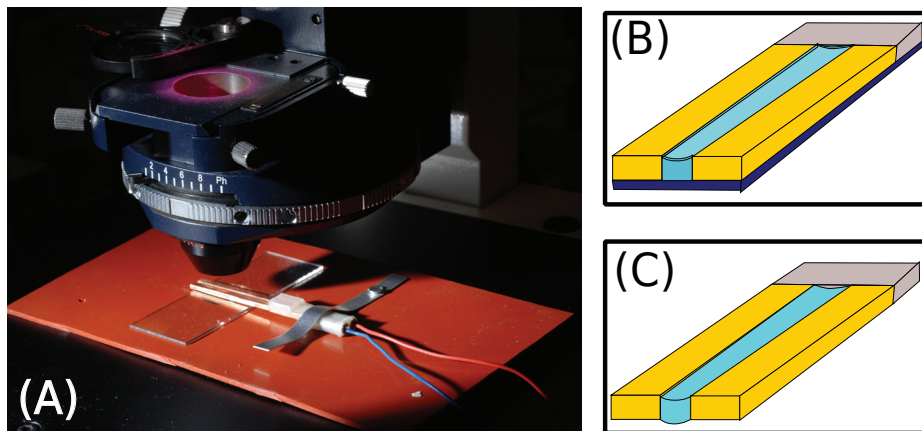
Figure 2.1: Experimental setup for initial measurements using powdered clay. In (A), the objective of the microscope, not visible in this photo, is below the copper electrode containing the sample and protected from oil by a microscope slide (not in contact with electrodes). The sample is illuminated from above and a high-speed camera is attached to the microscope to film the fast movements from below. Figures (B) and (C) show the sample holders used in these experiments, two copper electrodes are attached to a high voltage power supply. The silicone oil (light blue) is placed between the two electrodes. Initially a cover slide (dark blue) was glued to the electrode (B). This was removed in later experiments and the silicone oil was held in place by surface tension (C) and therefore the oil is only in contact with the electrodes.

Gravitational effects: There is a large difference in the density between the clay and the oils in which the experiments were performed ($1\,\mathrm{g\,cm^{-3}}$ vs $2.5\,\mathrm{g\,cm^{-3}}$). This was unavoidable and we were unable to density match the oil with the clay. For these initial studies the experiments were carried out without the bottom glass plate(Figure 2.1(B)), thus leaving the particles suspended in the oil. The particles were held in place by the oils' own surface tension and the plane of rotation is then perpendicular to the gravitational field.

Interaction between particles: There are many particles randomly distributed throughout the oil and between the electrodes. As they all interact with the electric field and rotate in the oil we observed some interaction between the particles through physical contact, hydrodynamic contact and interaction of the dipoles. Low concentrations of clay powder in the oil were used to mitigate this issue (see Figure 2.2). An example of the interaction between particles can be seen in Figure 2.3 between particles 1 and 4. The smaller of these particles does not fully align itself with the field as there is an interaction with the larger of the particles.

Repeatability: To avoid the interaction we are using very low concentrations, and this made it very hard to do repeated measurements on individual particles. Figure 2.2 shows a typical view through the microscope, where the copper electrodes are just outside the image on the left and right side. On application of the field the particles will rotate to align themselves and quickly start forming chains. In order to make a repeated measurement we would have to stir the suspension making it impossible to keep track of individual
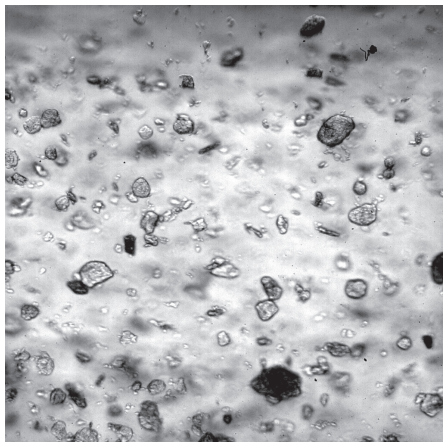
(a) Sample with high concentration of powdered clay. A large number of candidates suitable for tracking the rotation of the particle, but there were numerous interactions between particles.
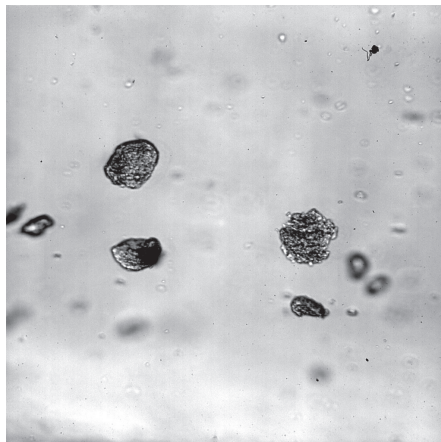
(b) Sample with low concentration of powdered clay. Interaction was less of an issue, but due to the low concentration there were very few candidates which were suitable for tracking the rotation of the particle. If the particles were not flat, i.e. their shortest axis was not vertical, the measurement would not be considered suitable.

Figure 2.2: Examples of powdered clay (NaFH) samples used in the initial experiments.

particles. We managed several repeated measurements by switching the field off almost immediately in order to avoid chain formation but this did not result in many usable particles per measurement.

Low yield: The particles are randomly orientated and at low concentrations. Here we define a plane spanned by the direction of the electric field and direction of the longest axis of the electrodes. This is the same plane that we are imaging. It is unlikely that we can find many particles with its two longest axis of the particle in this plane. Particles 1 and 2 in Figure 2.3 show two such particles rotating in the imaging plane. In Figure 2.3, particle 3 is rotating out of the imaging plane, and the particle will therefore have to rotate along all 3 dimensions. This increases the drag the particle experiences and makes it difficult to compare rotation times. A sample cell with multiple electrodes allowed us to pre align the particles in the plane such that the longest axis of the particles were close to ninety degrees to the primary electrodes, resulting in a full ninety degree rotation when the electrodes were switched. While the pre-alignment electric field is applied, the polarized oil will experience a net force counteracting some of the weight of the dispersion, thus climbing up the electrodes. Upon switching between electrodes there is initially a small fraction of time with no electric field present and therefore a relaxation of the oil. Thus the process of switching between the electrodes results in a randomization in the orientation of some of the clay particles. We might have been able to overcome these issues, but combined

with the non trivial field configuration due to the introduction of the additional electrodes, this encouraged us to try alternative methods (See section 2.2).
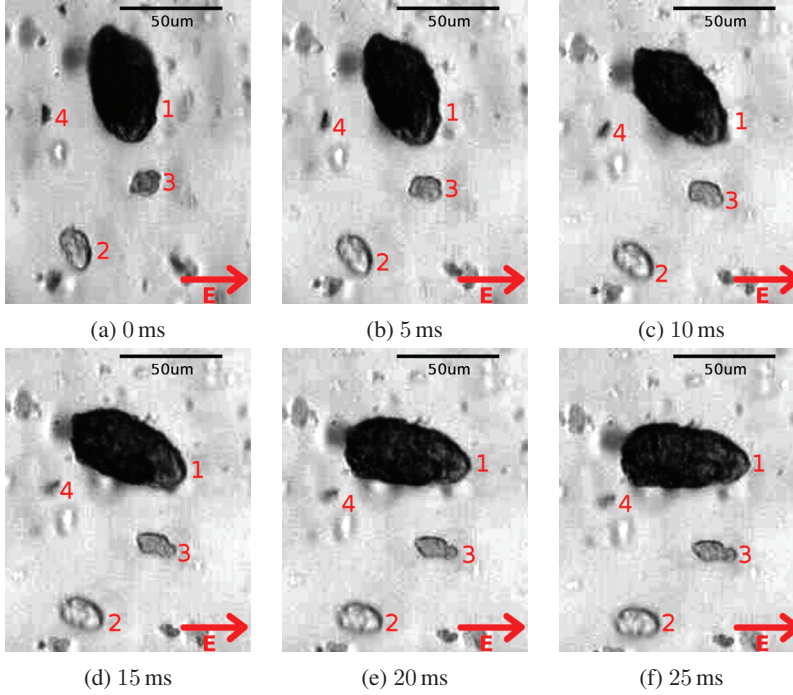
Figure 2.3: Particles rotating due to an electric field. Time shown under the image is the elapsed time in seconds from the time the field was applied. In the lower right corner the arrow shows the direction of the electric field (E). The direction of the gravitational field is in the image plane. This sample was measured at $1500\,\mathrm{V\,mm^{-1}}$ at $500\,\mathrm{Hz}$ AC in $100\,\mathrm{cSt}$ silicone oil. There are four particles of interest in this image. See main text for a longer discussion. Experiments carried out with Z. Rozynek.

2.1.3   Analysis

The results presented here were analysed using the same techniques as those shown in the analysis in chapter 2.3, where we fit the data by applying the theory described in Paper 5 using the equations:

$$\theta = \tan^{-1}(\tan\theta_0 e^{-(t-t_0)/\tau}) \tag{2.1}$$

$$\tau = \frac{\xi}{E^2 \Delta\alpha} \tag{2.2}$$

where θ is the angle of the particle with respect to the electric field $\mathbf{E}$, θ_0 is the initial angle the particle has at time t_0 (when the field is applied). τ is the characteristic rotation time for the particle, ξ is the rotational friction constant[39], which is proportional to the viscosity η, E is

the electric field strength, and $\Delta\alpha$ is the difference in polarizability of the particle in the parallel and perpendicular directions with regards to the electric field ($\Delta\alpha = \alpha_\parallel - \alpha_\perp$). Typical fits are shown in Figure 2.4.

Even though we had a number of issues with the setup we were still able to come with a number of conclusions with regard to the effect of the strength of the electric field and the viscosity of the system. The rotation angles versus time of two individual particles are shown in Figure 2.4.
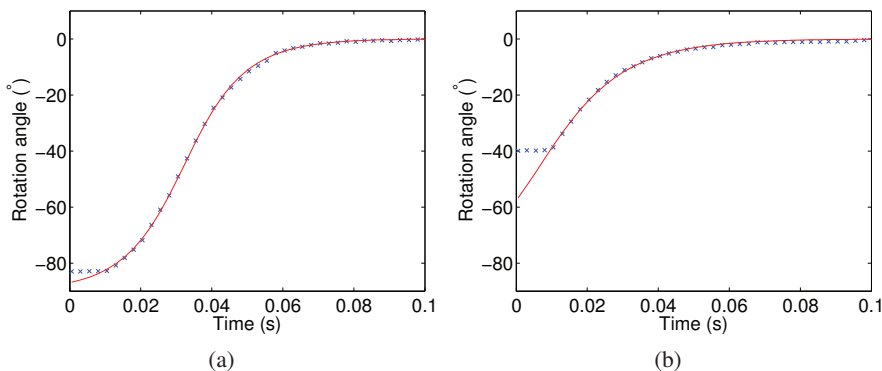

(a) (b)

Figure 2.4: Example of two particles rotating in the electric field. The particle in (a) is rotated just over $80°$ while the particle in (b) is seen to rotate around $40°$. In both plots the number of data points has been reduced by a factor of five for clarity. Both samples were measured at $500\,\mathrm{V\,mm^{-1}}$ at $500\,\mathrm{Hz}$ AC in $100\,\mathrm{cSt}$ silicone oil. The vertical offset, at t=0, between the data points and the fit are due to the initial orientation of the particle and the delay until the electric field is switched on. The red lines are a fit to the theory shown in Eq. (2.2).

2.1.4 Results

In Figure 2.5 we can see how a change in electric field strength changes the characteristic rotation time. We found in these initial studies that the rotation rate is inversely proportional to the square of the electric field strength.

Studying the rotation time at different viscosities showed that there was a clear linear relationship between the two. With five times greater viscosity the rotation time was 5 times longer (Figure 2.6). There is still a large spread in the data but we believe that this is related to the problems mentioned above, most notably the geometry and initial out of plane orientation of the particle.

We saw no effect on changing the AC frequency within the frequency range that was available to us ($0\,\mathrm{Hz}$ to $1800\,\mathrm{Hz}$ at $2\,\mathrm{kV}$). Figure 2.7 shows a plot of the data obtained from a change in frequency. There is little dependency on the frequency of the electric field oscillations.

2.1.5 Conclusions for powdered clay

These initial studies provided a lot of useful information and also gave us an indication on how to progress with further experiments. We required a way to make repeatable measurements
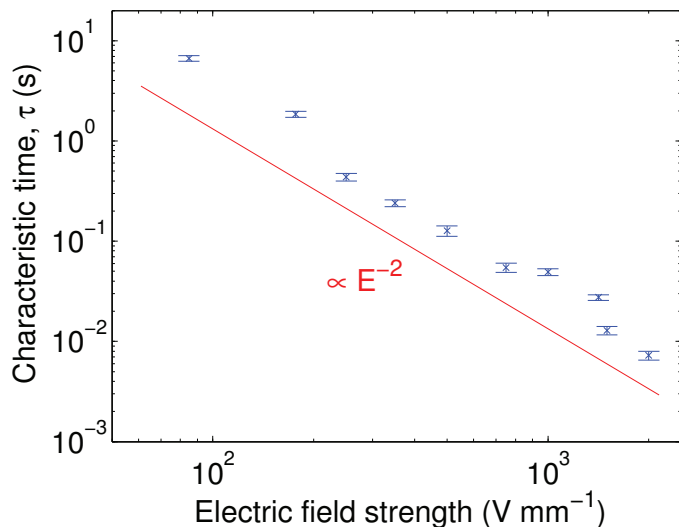
Figure 2.5: A plot showing the characteristic rotation time (τ) of the particles plotted against the field strength. The red line shows a slope of -2. Data is shown for a viscosity of 100 cSt and the error bars show the standard error.

preferably with a geometry that was simple. For these reasons we settled on the geometry which is described in chapter 1.2.2.

From the Figure 2.5 we can clearly see there is an E^2 dependency and this agrees with our theory (see Paper 5) that the characteristic rotation time is proportional to the electric field (E) and the dipole moment (p) which is again proportional to the field (E), thus an E^2 dependency. In Figure 2.6 we observed a linear dependency on the viscosity which is also expected as the rotational friction constant is proportional to the viscosity. The Frequency of the applied field (within the tested experimental range) seemed to have no clear effect on the characteristic rotation time.
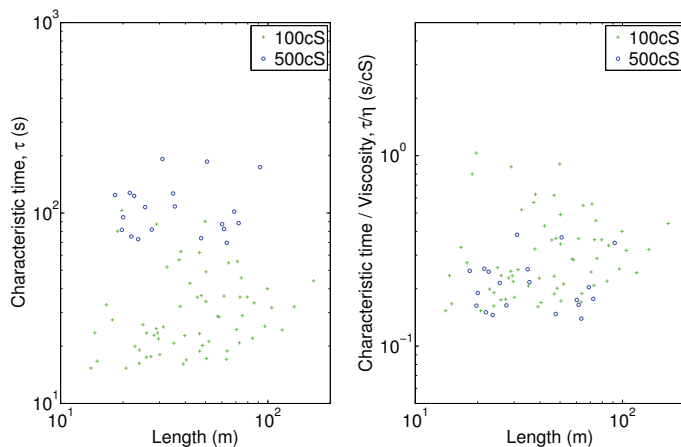
Figure 2.6: Left: The characteristic rotation time as a function of length for two different viscosities. Right: the same data, but scaled by the viscosity of the silicone oil. We expect an inverse relationship between the characteristic time, τ, and the viscosity as seen in Eq. (2.2). The large scatter in the data is mostly due to the large variation in size, shape and orientation of the particles.
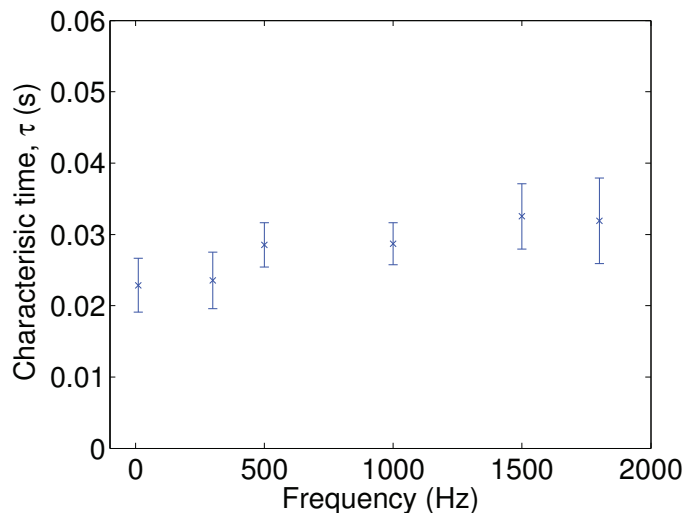
Figure 2.7: Characteristic rotation time (τ) as a function of the AC frequency of the field. Data is shown for a viscosity of $100\,\mathrm{cSt}$ and an electric field of $500\,\mathrm{V\,mm^{-1}}$, the error bars show the standard error. No significant scaling of the rotation time with frequency is observed

2.2   Experimental setup for large platelets

To overcome some of the issues encountered with the powdered clay we decided to produce large platelets by sedimentation of powdered clay as described in Paper 5 and chapter 1.2.2. This results in a particle we could repeatedly use and a well defined geometry. The experimental setup is quite similar to the powdered sample, just scaled up to accommodate larger particles. The setup is shown in Figure 2.8. Here platelet is placed in a PMMA cell which is connected to a high voltage amplifier. The sample cell is made from a standard $4.5\,cm^3$ (10 mm x 10 mm) PMMA cuvette with two thin $0.5\,mm$ copper plates that act as electrodes and are clipped onto the inside of the cell. This resulted in a separation between the electrodes of $9\,mm$. The high voltage signal is supplied by a HP 8116A function generator, and fed into the Trek 2200 power amplifier, capable of supplying just over $2\,kV$ AC at a maximum of $25\,mA$, and a maximum frequency of $7.5\,kHz$ at $2\,kV$ under no load. The high voltage source is attached to the sample cell by a pair of crocodile clips. A GW Instek GDS-1042 oscilloscope is used to monitor the signal (frequency, amplitude and shape) of the function generator and the low voltage "monitor output" of the power amplifier.

The particle is positioned and aligned in $1000\,cSt$ silicone oil using an electrically grounded needle. This ensures that if the particle at any point has become charged or if the probe comes in contact with live electrodes it would be discharged to the high voltage amplifier earth path. Whenever the particle was repositioned the needle would come into contact with the particle, thus discharging it to the high voltage amplifiers ground level. As in the case of the powdered clay, the density of the clay platelets are much greater than that of the surrounding oil, and the particles will settle. The time required to settle is linearly proportional to the viscosity of the oil. With the high viscosity used in these experiments the platelet made a full ninety degree rotation before getting to the bottom of the sample cell.
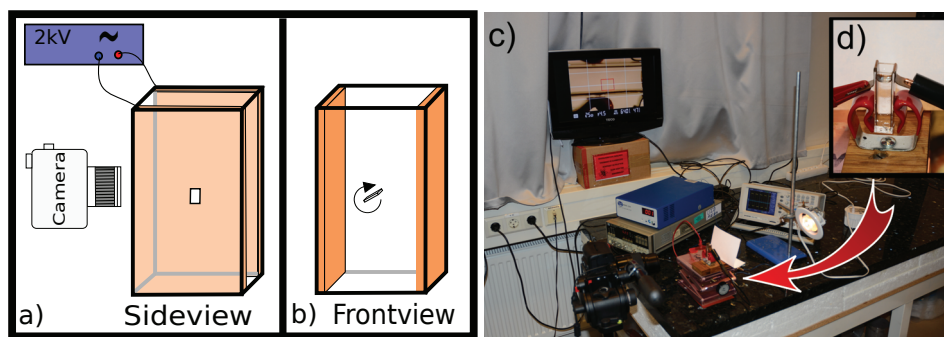
Figure 2.8: Experimental setup for the rotation experiments. (a) a side view, as viewed through the copper electrodes (coloured orange), (b) the view as seen from the camera. (c) the full experimental setup, with the sample cell (shown in insert (d) in same perspective as (b)) pointed to by the red arrow. See main text for a full description of the setup.

The rotation was filmed using a Nikon D7000 DSLR, either through a Nikon 105 mm micro lens or through a Zeiss microscope with 0.65-5x magnification. We found that the spatial resolution and the temporal resolution of the HD movie mode (1920x1080 pixels, 24 fps) of the camera was sufficient for these experiments.

The sample cell is lit from behind by a halogen light source, and is bright and diffuse enough (a piece of paper is used to diffuse the light) such that the platelet and sample cell are a silhouette with respect to the background lighting.

The voltage of the function generator is then adjusted to give the desired AC voltage, and the signal is switched on, reaching its peak voltage in less that $50\,\mu s$. The platelet will immediately start to align itself with the applied field and rotates such that it is perpendicular to the electrodes and parallel to the applied field.

Particle Orientation

It was observed to be quite important that the particles were orientated in the same direction for each measurement. The reason for this can be seen in Figure 2.9. This shows one of the most extreme cases of all the experiments that were made.
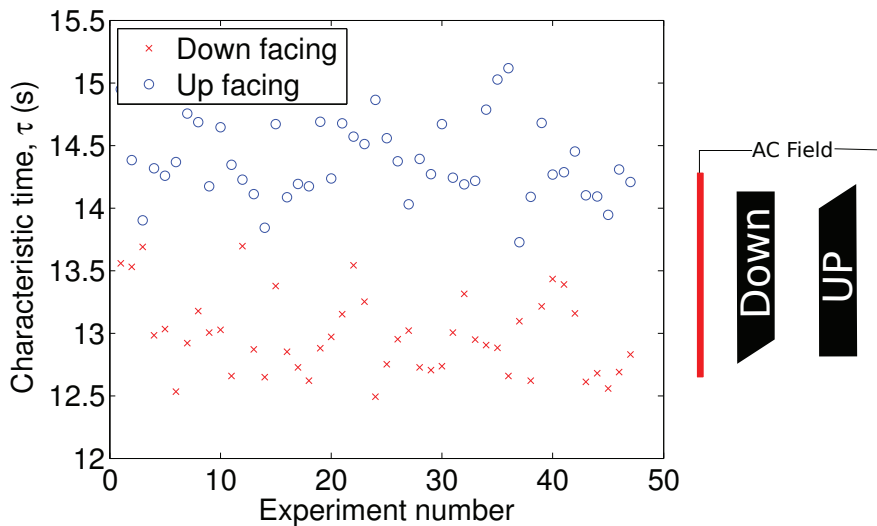
Figure 2.9: Effect of the orientation of the particle on the rotation time. The vermiculite particle was $2.7\,mm$ long, $0.3\,mm$ wide and $60\,\mu m$ thick.

We assume that this effect is due to a change in the hydrodynamic drag, and the size of the induced dipole due to any asymmetry in the particle shape. The sketch on the right shows an exaggerated example of the difference between the two orientations of the particle. The data is for a vermiculite particle, but a similar effect was noticed with fluorohectorite platelets.

For this reason measurements were sorted into two groups, depending on the orientation of the particle, resulting in a slight decrease in the standard error of the dataset.

2.3   Analysis

The videos made of the experiment were split into their respective frames using the program FFmpeg such that we had a large number of jpeg files. These are then imported into Matlab

and binarised such that the platelet is clearly differentiated from the bright background lighting. Using a MATLAB script we were able to identify the platelet and using the internal Matlab package region props package we could then obtain the angle of the platelet with respect to the direction of the electric field. Using the rotation angle we then used a least squares regression using the theory as described in Paper 5 and shown in Eq. (2.2), which provided us with the characteristic rotation time τ.

2.4   Frequency issues

Attempts were made to measure the frequency response of the platelet rotating in the field. At a field strength of $100\,\mathrm{V\,mm^{-1}}$, the frequency was increased from $7{\cdot}10^{-2}$ Hz all the way up to $7{\cdot}10^{3}$ Hz. These measurements were made for the vermiculite particle.
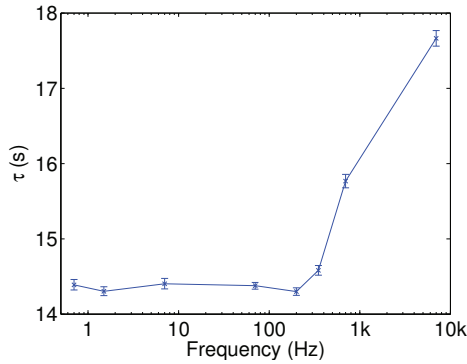
Figure 2.10: Frequency versus the characteristic time, τ, for the downward facing particle. There is a clear change in the system at around 700 Hz, which corresponds to the point at which a large increase in the current consumed in the system. Therefore, we think that this is an equipment issue.

In these experiments we were hoping to find any frequency dependencies in the rotation time. From [40] it is expected that at around $1000\,\mathrm{Hz}$ we should see a sharp drop in the permittivity of the material and hence the characteristic rotation time, as the interfacial contribution to the total permittivity falls away. We eventually had to conclude that there is not any clear dependency between the rotation time and frequency. This is more likely due to issues with the measurement as we were approaching the limitation of the amplifier. As we tried to increase the frequency in these measurements we saw a large increase in the current consumed, following a similar trend to that shown in Figure 2.10.

2.5 Effects of viscosity on rotation rate

For all viscosities measured, there is a clear linear dependency on the rotation time τ with the viscosity (Figure 2.11). From a theoretical basis, this is a reasonable observation as the dependency of τ on the viscosity is independent of size and the electric field as shown in Eq. (2.2). The tabulated properties of the oil are exactly the same and only differ in viscosity (and slightly in terms of density), but has the same dielectric and conductive properties as the less viscous oil (see Table 1.1).
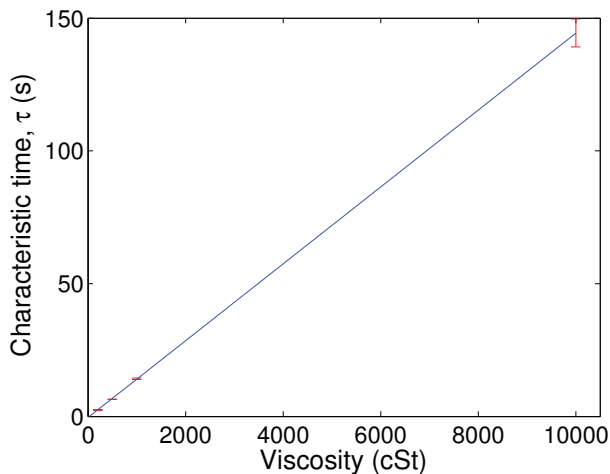

Figure 2.11: Effect of changing the viscosity on the characteristic rotation time, τ for a large platelet. The blue line shows a linear fit.

Chapter 3

Electric field alignment in an oligomeric matrix

Using WAXS we were able to make measurements of the anisotropy during melting and crystallisation and of the hydration process of LiFh clay dispersed in an oligomeric (a molecular complex consisting of a few monomer units) wax.

The oligomeric matrix in these experiments was a paraffin wax, (chemical formula C_nH_{2n+2}), where n was in the range of 15-40, giving rise to a melting point between $53\,°C$ to $80\,°C$. Our particular wax had a melting point of $65\,°C$ and n had a distribution of 20-40. In this experiment we used a powdered clay with similar properties to those mentioned in chapter 1.2.2.

One batch was prepared by randomly dispersing LiFh (5wt.%) in molten paraffin wax that was then allowed to solidify. This sample was slowly heated in the presence of an electric field. As the wax melts the LiFh will align with the field and eventually form column like structures. With the electric field applied and the heating removed, the paraffin is allowed to solidify, freezing the orientation of the particles and the column like structure. During the heating and cooling cycle we made WAXS measurements and could therefore monitor the degree of anisotropy due to the orientation of the particles and the chains.

On a second batch we made WAXS measurements at two points in time, six months apart. The WAXS measurements allowed us to measure the separation between the layers and analyse the intercalated water content in the clay. During the melting and dehydration process measurements were made at regular intervals these show that we require close to 10 hours transition from a pure 1 water layer state to an almost pure 0 water layer state. Six months later a new set of WAXS measurements were made on the samples and we could see that there was some hydration of clay going form a 0 water layer state to a 1 water layer state.

3.1 Experimental setup

Sample preparation was done at NTNU by Z. Rozynek prior to the trip to the ESRF facility. A first batch was prepared by heating the paraffin wax to $90\,°C$ and adding $7\,g$ of powdered Li-FH clay, the largest particles were allowed to settle out of the dispersion. The dispersion was then stirred for an hour at a temperature of $80\,°C$ to $90\,°C$. The dispersion was then allowed to cool, and cast into a solid piece. This was then cut into strips such that they fit into the

sample cell (Figure 3.1), about 1 mm thick and wide and high enough to cover the X-ray beam. Each strip of solid paraffin wax had randomly orientated clay particles embedded in it. The measurements for the electric field induced alignment were made using a special sample cell that would allow us to both heat the paraffin wax and to apply an electric field. The sample cell (shown in Figure 3.1) was used in conjunction with measurements done at the ESRF beamline. A strip of the randomly dispersed LiFh was placed in the cell and the electric field was applied while a heat source was powered and measurements were made.

A second batch of paraffin wax with LiFh clay made by heating the dispersion to 120 °C to 130 °C under constant stirring. Every hour a small sample was removed and cast into a solid strip, each $30 \times 6.5 \times 1.5$ mm^3, and immediately X-rayed. They were then left in lab conditions for 6 months and re-analysed.
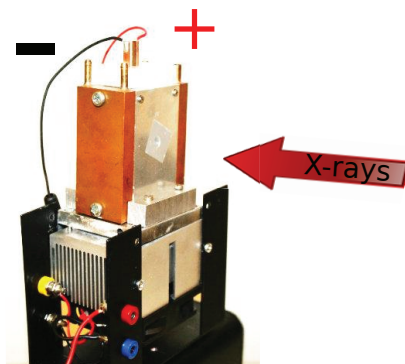

Figure 3.1: Sample cell used to heat the paraffin wax while applying an electric field. From Paper 1

3.2 Analysis

The measurements are made using a 2D detector, a MAR345 image plate at ESRF and a 2D gas detector at the lab in Trondheim. The 2D data obtained (example of this can be seen in Figure 1.5(B)) from these sensors are analysed using the FIT2D program, by integrating the first clay peak, corresponding to the 001 Bragg peak radially over a narrow q-range. The 1D data was then fitted using the Maier-Saupe function, which returns the S_2 order parameter, which ranges from $-\frac{1}{2} - 1$, where $-\frac{1}{2}$ is a perfect orientational order in the anti-nematic configuration, and 1 is a perfect orientational order in the nematic configuration, and finally 0 means that there is no orientational ordering of the system. Details of this fitting are given in chapter 1.2.4.

3.3 Results

There was a clear development of anisotropy of the clay particles (Figure 3.2a) in the oligomeric matrix during the melting and crystallisation of the paraffin wax. One of the interesting features was that order parameter S_2 reached its peak value of -0.36 (Figure 3.2b) just before the chain
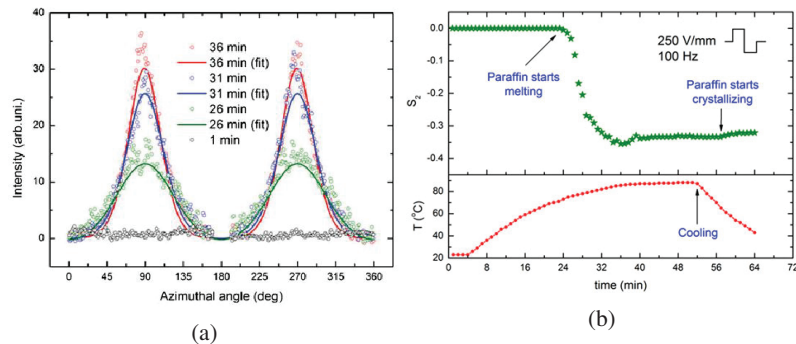
Figure 3.2: (a) Azimuthal plot of the first Bragg peak measured during melting of the paraffin wax. This clearly shows that there is in increase in the anisotropy of the sample as the experiment progresses. (b) Plot showing the order parameter S_2 and the temperature as a function over time. From Paper 1

formation, at which point the value decreases by 15%. This means that there was a slight loss of anisotropy as the chains form, the order parameter falls once more and this time we suspect this was related to the crystallisation of the paraffin wax.

These experiments also showed that the paraffin wax substantially changes the dehydration and hydration rates of the clay particles in the oligomeric matrix. It took a full 10 hours (Figure 3.3a) to remove the intercalated water and even after 6 months there was still a substantial population of clay particles with no or little intercalated water (Figure 3.3b). For the powdered clay sample the time taken to hydrate is typically on the order of a couple of hours[41], this is in sharp contrast to the time taken to hydrate a sample in paraffin wax.

(a)

(b)
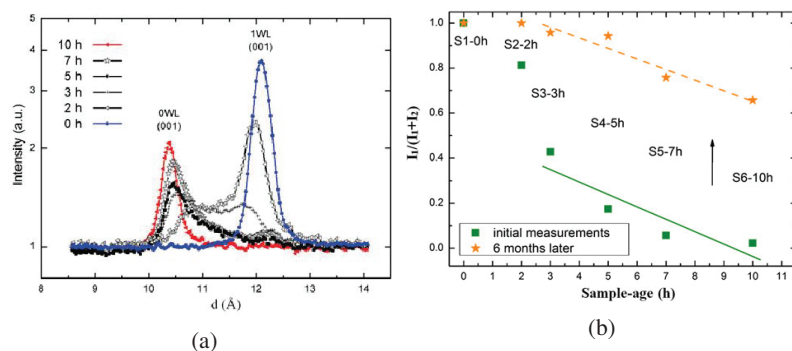
Figure 3.3: (a) Time evolution of the one to zero water layer (WL) transition. We can see a high intensity of the 1WL peak, as time progresses the peak almost vanishes and a new peak is formed at the 0WL position. (b) Plot showing ratio $I_1/(I_1 + I_2)$ of the 0 water layer and the 1 water layer peaks. Their value are in the range of 0-1, where 0 indicates a pure dehydrated state and 1 indicates a pure monohydrated state. A value of 0.5 indicates an equal hydration level. From Paper 1

Chapter 4

Armoured colloidal drops

4.1 Experimental development

As mentioned earlier, this work is a development of work done by a student at NTNU, Kjetil Hersvik[19], who did measurements on oil drops suspended in a different oil and the subsequent deformation of a silicone oil drop in castor oil on application of an electric field. The electro-hydrodynamic flow responsible for this behaviour can be explained by the Taylor-Melcher leaky dielectric model [42, 43, 44] (Figure 4.1).
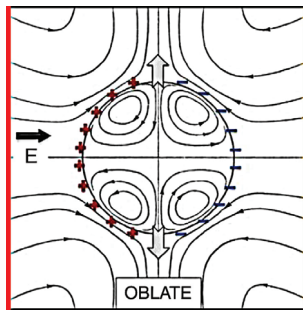

Figure 4.1: Hydrodynamic stream lines as seen in Taylor's hydrodynamic drop model. Image from Paper 4 and adapted from [42]. The + and - signs signify the surface charge of the drop.

A drop with no net charge is suspended in another fluid and exposed to an electric field. The fluids should have different physical properties. The drop will disturb the electric field, creating a discontinuity in the electric stress across the drop interface. For perfect dielectrics there are no free charges and the electric stress will only have a normal component. The drop will then adopt a prolate shape as the electric stress can then be balanced by the interfacial tension. There will be no hydrodynamic flow either inside or outside the drop. On the other hand if we have a leaky dielectric (slightly conductive dielectric), charges are brought to the interface by conduction, due to the interactions with the electric field this creates a tangential stress which sets the fluids in motion both inside and outside the drop. This hydrodynamic flow can then deform the drop in an oblate manner as in Figure 4.1. On application of an AC field the drop will not respond above a threshold frequency. This frequency is dependant on the physical properties of the fluids used and is 1Hz in the silicone drop in castor oil.

Any images presented in this section will have gravity pointed down, i.e. the drops fall from the top to the bottom of the page. Some of the first attempts at trying to map the flow inside and outside the drop were made using powdered clay as seen in Figure 4.2, or polyethylene particles, which can be seen in Figure 4.3. The traces for the clay particles gave a very good picture of what was happening, and for this reason we attempted to make a similar measurement with polyethylene beads that we could trace. Using a laser sheet, we attempted to light up a single plane of beads going through the centre of the drop. The result from this is shown in Figure 4.3. Due to the large number of particles outside the drop we suspected that there are more interaction than we would have preferred. For this reason we made measurements using a only a few tracer particles (as shown in Figure 4.5).
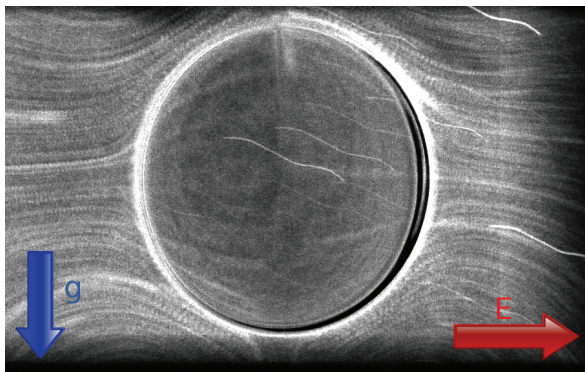

Figure 4.2: Tracing the hydrodynamic flow around a drop, traces made from particles of clay. This was made by stacking the images on top of each other and finally normalising the resulting image. The paths the clay particles have followed can be clearly seen around the drop. The electric field was applied horizontally and the drop fell from top to bottom in a gravitational field. Experiment performed at NTNU by K. Kjerstad[21].

4.2 Experimental setup

The armoured colloidal drop experiments were carried out using a similar setup of the rotation experiments. They either consisted of a $4.5\,\text{cm}^3$ PMMA cell, as in chapter 2.2, or a custom glass cell made of microscope slides and Indium Tin Oxide (ITO) coated glass (see Figure 4.4). The ITO coated glass was used so that we could have a transparent electrode and view the movement of the clay or beads during the experiment. The ITO glass was in contact with the oil. As our high voltage amplifier was incapable of supplying the voltages required for some of the stages of drop formation, we ended up using $3\,\text{mm}$ thick brass electrodes for some of the initial experiments. This reduced the spacing of the electrodes to $4\,\text{mm}$ thus increasing the field magnitude substantially. In contrast to the rotation experiments, for most of the drop experiments we needed to use the microscope in order to zoom in close enough to see the detailed movement of the drops and particles within. Here the sample cell was filled with castor oil and a drop was made using a micropippet. A small volume of silicone oil was dispensed into the castor oil and the micropippet was pulled away. Generally we aimed at getting a drop of around $1\,\text{mm}$
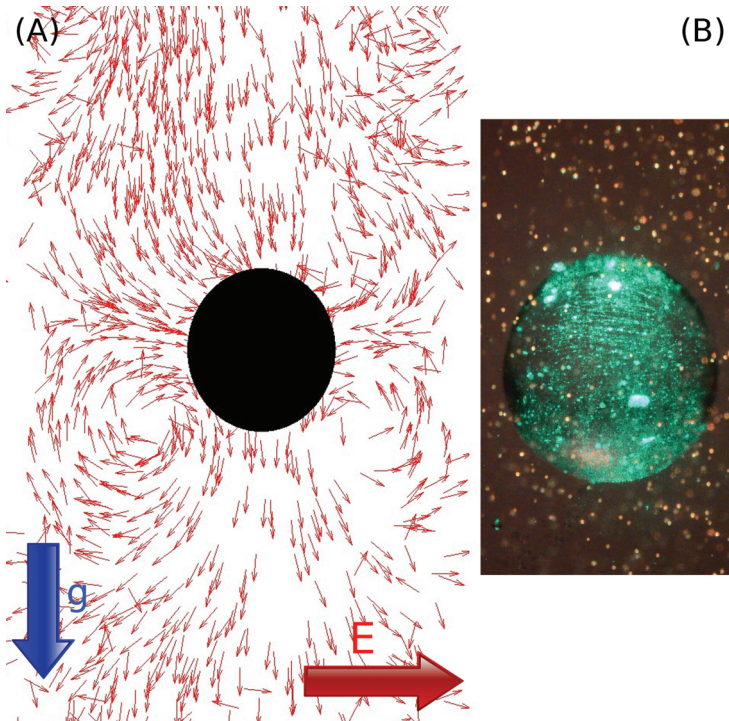
Figure 4.3: (A) A first attempt at visualising the electro-hydrodynamic flow aroudn a silicone oil drop suspended in castor oil. (B) A cropped and unprocessed image showing the droplet analysed in (A). Here we placed some polyethylene beads in the castor oil and applied an E-field indicated by the large red arrow(left to right). Using an image analysis script in Matlab we traced the beads' movement in the surrounding oil, resulting in flow vectors in red. The small flow vectors show the direction of hydrodynamic flow around the silicone drop. The downward pointed arrows at the top of the image clearly indicate the effects of gravity as the drops fall in the oil. The polyethylene beads were lit using a green laser sheet in order to light up a narrow imaging plane slightly wider than the diameter of the drop.
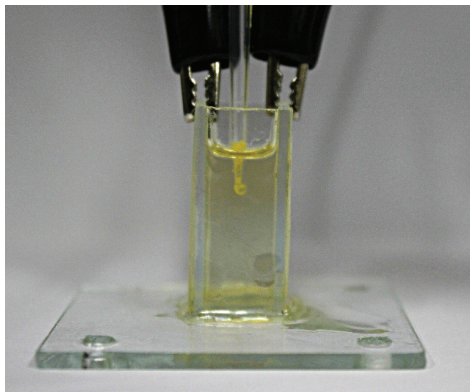
Figure 4.4: Example of a sample cell used for imaging drops parallel to the field. The ITO glass is parallel with the long edge of the microscope glass. The high voltage supply would be connected to the glass. Inside separation between the plates was $10\,\text{mm}$.

in diameter. As the silicone oil is slightly more dense than the castor oil ($964\,\text{kg}\,\text{m}^{-3}$ versus $961\,\text{kg}\,\text{m}^{-3}$) the oil drop would slowly settle in the sample cell. Similarly, the particles added, clay or polyethylene beads, have a higher density relative to the oil and these would eventually settle out. In both cases the high viscosity of the castor oil, and the relatively high viscosity of the silicone oil prevents this from happening too quickly and we were generally able to carry out the experiment before gravitational effects became a problem. In newer experiments we have density matched the two oils such that there is almost no sedimentation of the drop due to gravity[45].

The field was controlled by manually switching the amplifier on and off. As the response of the system took some time, this was sufficient to create the ribbon of particles and cover the drop.

4.3   Analysis

The image analysis done on these drops was mostly done manually, as the drops had a complex surface structure. The automatic image recognition software had problems identifying the full shape of the drop due to light and dark areas, the opening of the pupil, and position of the individual beads. This meant that in order to analyse these experiments, the video was split into its individual frames and by using an image analysis program called Fiji. Frames were analysed by drawing either an ellipse, square or a freehand shape around the area of interest and allowing the software to return the required geometric data. See Figure 4.5 for an example of the paths traced out.

During these initial experiments, it was noticed that if a clay was added to the drop it would form a "twister", as we initially called it, inside the drop. This was a V shaped aggregation of clay and turned out to be on the surface of the drop (similar to what is shown in Figure 4.6). This occurred when an applied electric field was within a certain magnitude range. After studying this effect, it was realised that this was actually a ribbon and the narrow section at the bottom

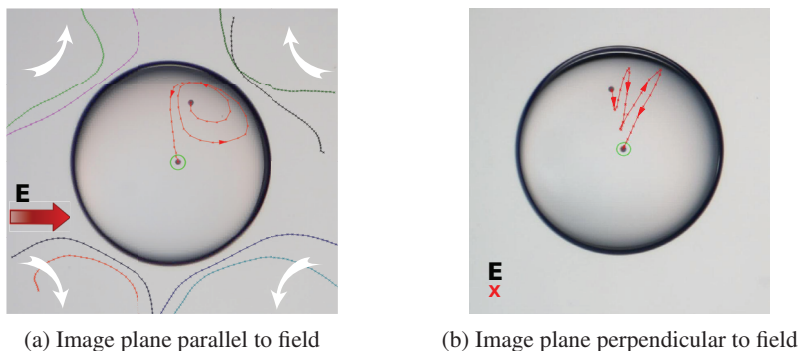(a) Image plane parallel to field   (b) Image plane perpendicular to field

Figure 4.5: Particle tracking inside and outside the drop, the particles position was tracked using Fiji, noting the position for each time step. The particles final position is marked by the green circle. Experiments performed at NTNU by A. Mikkelsen.

was due to the effect of gravity. As the drop falls the viscous drag of the surrounding oil will pull the particle towards the top of the drop. Depending on the rate at which it falls, the applied field, and how long it had been falling, the effect could become more or less pronounced.
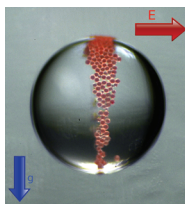

Figure 4.6: Drop with ribbon of polyethylene particles falling in a gravitational field. Note the width of the ribbon at the top and bottom of the drop. A similar effect is observed with powdered clay. Experiment performed together with P. Dommersnes.

The fact that there was a ribbon formation at the surface led to another question, and that was how the particles had migrated to the surface. Immediately after application of a field we could observe movement of any particles added to the drop. The particles would then migrate to the drop surface over time, even though the Taylor-Melcher stream lines never got the particles close enough to the surface to adsorb onto it. We propose that the migration to the surface happens primarily through short range dipole interaction between particles already at the surface and those in the bulk. The particles at the surface are adsorbed strongly to the surface, due to capillary binding, and they are then able to pull the particles in the bulk to the surface. In addition we also expect that there is an uptake of charge on the clay particles, which combined with the applied field will drive them to the surface. The electro-hydrodynamic flow is an important contributing factor to the migration to the surface as we do not see the particle migrating to the surface in an AC field. But what we do notice is that in a DC field, sedimentation of the particles within the drop seem to significantly increase the rate of adsorption to the surface as the particles get closer to the droplet interface and can bet adsorbed more easily.
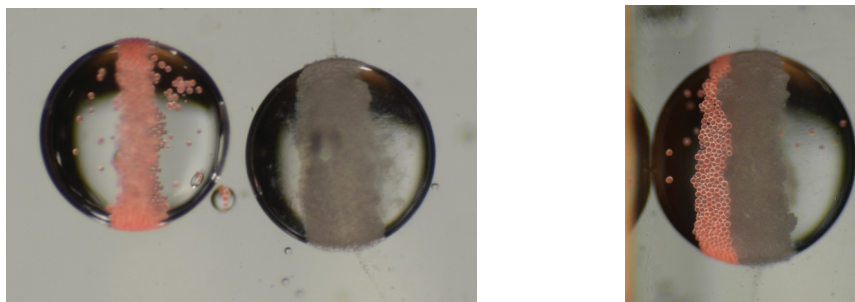
(a) Two drops, the left with red polyethylene beads the right with semitransparent silica beads. At this stage the tightly packed ribbon has been formed due to the applied electric field.

(b) Due to electrostatic and electro-hydrodynamic forces the two drops approach each other and eventually electro-coalesce. The coalesced drop with densely packed ribbon is shown above.

Figure 4.7: Merging of two drops with ribbons made of polyethylene and silica. Experiment carried out together with P. Dommersnes.

4.4   Results

While trying to map the movement of particles inside a drop, we found an interesting technique of merging two drops and as a result creating stripes of two different types of particles. Once the droplet had formed a tightly packed ribbon the two drops are attracted to each other due to the electrostatic and electro-hydrodynamic forces[45]. Once the particles are close enough they will eventually merge forming a larger drop. In Figure 4.7 we can see the result of merging two drops containing red polyethylene particles ($45\,\mu$m to $53\,\mu$m) and transparent glass beads ($1\,\mu$m). This process can be repeated many times to create a striped drop or, alternatively, only once with a larger number of particles in each drop to create a "Janus shell". This is a drop with two hemispheres of different types of particle.

Viewing the drop through the electrodes allowed us to see how the ribbon formed and as a consequence we were also able to observe the "pupil effect". At low fields we actively encouraged the ribbon formation, while at high fields the ribbon got stretched and would fully cover the drop. When seen from the right angle it looks like the pupil contracts and expands as the field strength is varied. At low fields the Taylor-Melchner flow induces the formation of the ribbon. Whereas at higher fields the conductivity of the clay is higher than that of the oil and as a result there will be free charge build up on the edge of the ribbon, which can then induce electro-stretching of the ribbon. As the ribbon is stretched by the field it also diminishes the charge build-up (shown in Figure 4.1) and suppresses the electro-hydrodynamic flow. This allows the clay to form a film and cover the surface, essentially creating a Faraday cage thus preventing further flow. Lowering the field again will allow the Taylor-Melchner flow to induce the ribbon formation. See figure Figure 4.8 for an example.

The suppression of the electro-hydrodynamic flow can be seen more clearly by use of conductive beads Figure 4.9. If a sufficient number of beads are added, such that they cover the entire drop surface, the conductivity of the drop is significantly increased, shorting out the build up of charge on the surface, and there will no longer be a Taylor-Melchner flow. The drop is now more conductive than the oil it is suspended in and the drop will stretch in a prolate manner.
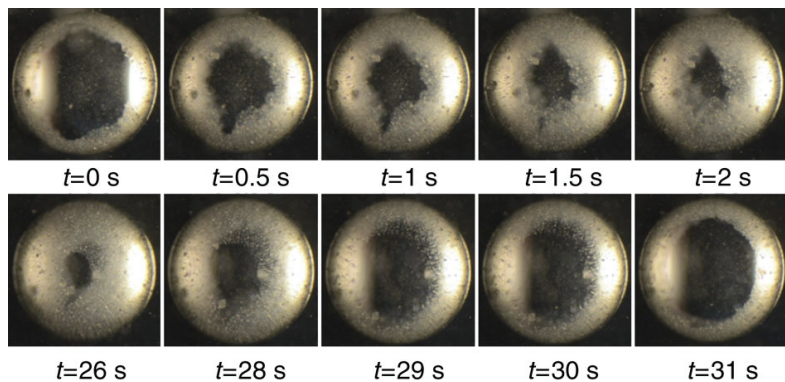
(a)
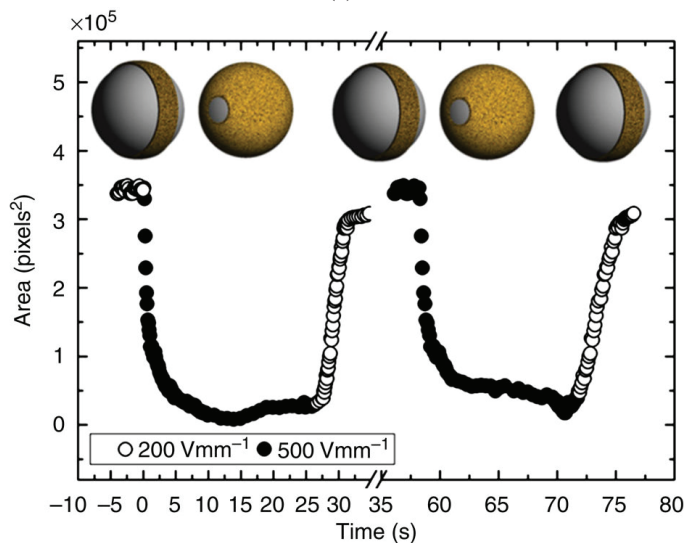
(b)

Figure 4.8: The images in (a) and the plot (b) shows how we could dynamically control the size of the clay "pupil" on a 1 mm drop, by only using a DC electric field. At low fields ($200 \, \text{V} \, \text{mm}^{-1}$) the clay will form a ribbon around the drop, whilst at high fields ($500 \, \text{V} \, \text{mm}^{-1}$) the clay "armour" will be stretched such that the "pupil" contracts. Experiment performed together with P. Dommersnes.
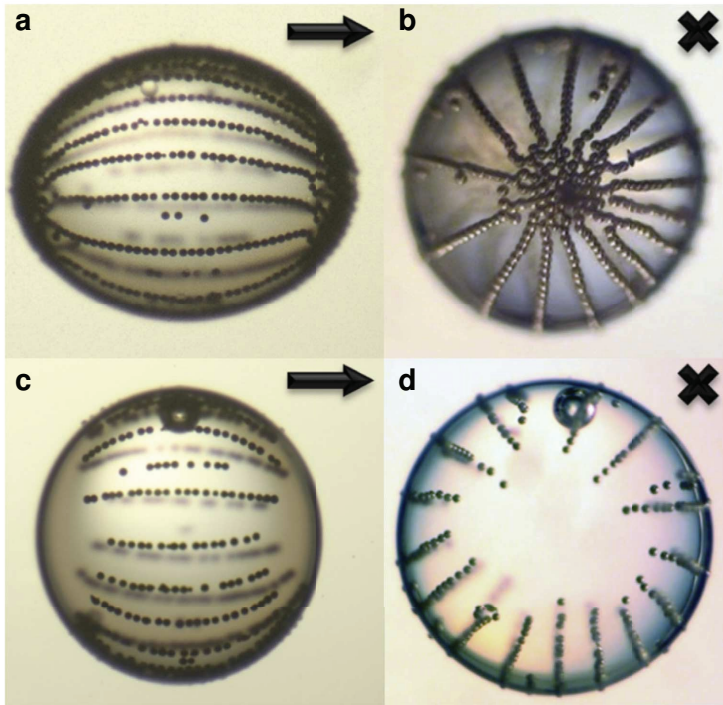
Figure 4.9: A 1 mm silicone oil droplet with conducting silica beads. (a,b) The beads attract, forming chains on the surface of the droplet, short circuiting the drop and deforming the droplet in a prolate fashion. (c,d) have a lower concentration of beads and they are unable to stretch across the full drop surface and therefore an oblate deformation is observed, this indicates the presence of a Taylor-Melchner flow. The Arrows and crosses indicate the direction of the electric field. Experiments done by Z. Rozynek at NTNU.

If there are too few beads to cover the entire length of the drop there will be some build up of charge and the drop will deform in an oblate manner indicating the presence of Taylor-Melchner flow.

Chapter 5

Conclusions and future prospects

We found some clear field and viscosity dependencies on the rotation rate for a particle rotating in an electric field, There was also an increase in the rotation rate as a particles' hydration level was increased. We have seen that the change in polarizability of a clay particle increases and peaks at width/length ratio of 0.24. There still are many unanswered questions and a lot we would like to do. We would like to be able to answer which molecules or cations are contributing the most to the size of the dipole, and by how much. We would also like to be able to measure the frequency response over a larger frequency range, say from $1\,\mathrm{Hz}$ to $10{,}000\,\mathrm{Hz}$. We had hoped to be able to see if there was a sharp drop at around $1000\,\mathrm{Hz}$ due to a drop in the permittivity as the interfacial contributions are no longer able to respond quickly enough. Making a more complete viscosity measurement with a couple of data points at intermediate viscosities would be nice to take any doubt away from the measurements.

We saw that we were able to keep the anisotropic ordering of clay particles in a paraffin matrix even when it had completely solidified with only a small loss in order when the paraffin wax solidified. The paraffin wax also seemed to delay the clay from absorbing water and changing the hydration state. Even after six months there still was a large population of clay without any intercalated water. In future investigations we plan on studying the water diffusion through the paraffin matrices with aligned clay particles.

The colloidal armoured drop experiments showed some very interesting ways of organising particles within a drop. The particles would self organise to form a ribbon around the drop, due to hydrodynamic flow induced inside and outside the drop. We were also able to dynamically change the flow and therefore able to break up the ribbon and reform it. One of the most interesting properties of the drop was the "pupil" that we were able to dynamically open and close depending on the size of the applied electric field. Having better control of the pupil would be an area of research that would be interesting to take further, possibly even being able to speed up the process. Work has been started on merging one or more drops to produce a larger drop that had either alternating bands or two different hemispheres ("Janus shell") of different materials. Finally it would be interesting to create a solid surface structure by connecting the beads either by sintering or chemically bonding them together. If you were then able to remove the oil you would be left with a hollow shell of the drop.

Chapter 6

Summary of Papers

Paper 1: Electric field nematic alignment of fluorohectorite clay particles in oligomeric matrices.
This paper shows how synthetic fluorohectorite dispersed in paraffin wax behaves when it is aligned using an electric field. Clay particles are dispersed in liquid paraffin wax and aligned in an electric field, a process that is slower than in silicone oil due to the increased viscosity. Initially a sample without any preferential orientation is exposed to an electric field. As it was heated the order parameter decreases to -0.36 and only increases slightly on crystallisation.

As the samples are held in the melted clay for extended periods of time the number of water layers intercalated between the clay layers is decreased, requiring almost 10 hours to reach the zero water layer state.

In addition the rehydration of the clay particles is studied by monitoring the dehydrated particles after being stored at room temperature for 6 months in humidity ranges of 20–30% relative humidity. From this part of the study it can be seen that the particles will rehydrate at a much slower rate than those not stored in the polymer matrix.

Paper 2: Clay alignment in electric fields. Aggregates of NaFh are made by sedimentation of powdered clay, and allowing the water to evaporate. This produces layered clay samples with their stacking direction parallel to the sedimentation direction. A single particle was suspended in silicone oil so that we could investigate the alignment properties of the clay particle. We found that we could get a data collapse of the alignment angle of the particle versus time, if we divided time with the square of the electrical field.

Paper 3: Dipolar ordering of clay particles in various carrier fluids. This article is mostly a summary article discussing the work carried out in our collaborative group. A study of the effect of shearing a dispersion of 5wt% NaFh powder is performed and the viscosity is measured in terms of the shear velocity and the field strength, which is varied between $350\,\text{V}\,\text{mm}^{-1}$ and $1000\,\text{V}\,\text{mm}^{-1}$. As the field is increased the viscosity is also increased, similarly if the shear velocity is decreased the viscosity also increases.

LiFh powder was dispersed in paraffin wax at $90\,°\text{C}$ and allowed to cool in an electric field of $500\,\text{V}\,\text{mm}^{-1}$, WAXS studies of the sample showed that there was no preferential ordering in the polar angle.

CTAB-FH was added to a styrene monomer and in the presence of an electric field of $830\,\text{V}\,\text{mm}^{-1}$ allowed to polymerize for 7 days. Using X-ray scattering it was shown

that there is a pronounced peak in d_{001} which is due to the clay particles aligning with the stacking direction perpendicular to the electric field. This sample, as in the previous sample, shows no preferential alignment when viewed along the chains.

Finally laponite is suspended in air and aligned with an AC electric field of $500\,\mathrm{V\,mm^{-1}}$. When the field is applied most of the aggregates are aligned and form chains over the electrodes. At higher concentrations not all the particles will align but this is due to packing, preventing the particles from orientating themselves.

Paper 4: Active structuring of colloidal armour on liquid drops. In this paper we look at the process of creating a colloidal armour on the surface of the liquid drops. We show how we can dynamically control the properties of the colloidal armour by adjusting the electric field that the drop is exposed to.

The drops were created by placing a silicone oil drop inside a bath of castor oil. The silicone oil contains either powdered clay, polyethylene particles or coated silica beads.

On application of an electric field the particles in the silicone oil will migrate to the surface of the drop either creating a ribbon, or if the concentration is high enough it will coat the whole surface, which could lead to jamming.

By adjusting the electric field we were able to adjust the convection within the colloidal drop, changing the shape of the drop, creating rotating domains within the ribbon, opening and closing a pupil of uncovered surface. We also studied the flow of the fluid inside the drop using tracer particles and managed to confirm a flow as expected by Taylor's models.

Paper 5: Insight into the alignment of clay platelets in silicone oil. Using large platelets made by sedimentation of powdered sodium fluorohectorite clay dispersed in water, the platelets were dried and measurements were performed to investigate the time required to align the platelets suspended in silicone oil to an electric field.

By varying the magnitude of the electric field, the dimensions of the platelet and the number of water layers we have attempted to determine some of the properties of the clay platelets.

We have shown a theoretical model of the platelet aligning itself in the electric field, and have used this to estimate the polarizability of the platelet using the experimental data. From this we are able to show that there is a peak in the polarizability at a width/length ratio of approximately 0.25.

From the experimental data we can conclude that the alignment time had a E^2 dependency on the magnitude of the electric field, such that doubling the field we saw a rotation rate that was 4 times as fast. When a dehydrated platelet was placed in the silicone oil we saw that there was a significant decrease (corresponding to 10%) in the rotational time and have concluded that this was due to the hydration of the platelet. In addition to the rotational alignment experiments, we found the fricational drag constant for the hydrodynamic drag on plate by measuring the torque experienced when a plate is rotated in a bath of a high viscosity fluid. From this data we were able to extrapolate the effect of the dimensions of the clay platelet on the viscous drag that it experiences.

Chapter 7

Bibliography

[1] Flavio Romano and Francesco Sciortino. "Colloidal self-assembly: Patchy from the bottom up." In: *Nat Materials* 10 (3 Mar. 2011), pp. 171–173.

[2] M. Okamoto et al. "Biaxial flow-induced alignment of silicate layers in polypropylene/clay nanocomposite foam." In: *Nano letters* 1.9 (2001), pp. 503–505.

[3] X. He et al. "Morphology and melt rheology of nylon 11/clay nanocomposites." In: *Journal of applied polymer science* 102.1 (2006), pp. 542–549.

[4] H. Hemmen et al. "The Isotropic- Nematic Interface in Suspensions of Na- Fluorohectorite Synthetic Clay." In: *Langmuir* 25.21 (2009), pp. 12507–12515.

[5] E. N. De Azevedo et al. "Anisotropic water diffusion in nematic self-assemblies of clay nanoplatelets suspended in water." In: *Langmuir* 23.9 (2007), pp. 5100–5105.

[6] http://delphi.com. *Audi R8 Features Delphi's Revolutionary MagneRide Semi-Active Suspension.* Mar. 2006. URL: `http://delphi.com/news/pressReleases/pressReleases_2006/pr_2006_11_30_001/`.

[7] Nicholas K Petek et al. "Demonstration of an automotive semi-active suspension using electrorheological fluid." In: *SAE PUBLICATION SP 1074. NEW DEVELOPMENTS IN VEHICLE DYNAMICS, SIMULATION, AND SUSPENSION SYSTEMS (SAE TECHNICAL PAPER 950586)* (1995).

[8] T. Halsey and J. Martin. In: *Scientific American* 42 (Oct. 1993).

[9] Sharon C. Glotzer and Michael J. Solomon. "Anisotropy of building blocks and their assembly into complex structures." In: *Nat Mater* 6 (7 Aug. 2007), pp. 557–562.

[10] Shan Jiang et al. "Janus particle synthesis and assembly." In: *Advanced materials* 22.10 (2010), pp. 1060–1071.

[11] Tony JunáHuang et al. "Microfluidic synthesis of multifunctional Janus particles for biomedical applications." In: *Lab on a Chip* 12.12 (2012), pp. 2097–2102.

[12] Rodney T Chen et al. "Fabrication of asymmetric Janus particles via plasma polymerization." In: *Chem. Commun.* 46.28 (2010), pp. 5121–5123.

[13] F. Gao. "Clay/polymer composites: the story." In: *Materials Today* 7.11 (2004), pp. 50 –55.

[14] D. Ratna et al. "Poly(ethylene oxide)/clay nanocomposite: Thermomechanical properties and morphology." In: *Polymer* 47.11 (2006). Special issue in honour of James McGrath, pp. 4068 –4074.

[15] G. Choudalakis and A. D. Gotsis. "Permeability of polymer/clay nanocomposites: A review." In: *European Polymer Journal* 45.4 (2009), pp. 967 –984.

[16] K. Yano et al. "Synthesis and properties of polyimide-clay hybrid." In: *Journal of Polymer Science Part A: Polymer Chemistry* 31.10 (1993), pp. 2493–2498.

[17] H. Althues, J. Henle, and S. Kaskel. "Functional inorganic nanofillers for transparent polymers." In: *Chem. Soc. Rev.* 36 (9 2007), pp. 1454–1465.

[18] Z. Rozynek et al. "Electric field induced structuring in clay-oil suspensions: new insights from WAXS, SEM, leak current, dielectric permittivity, and rheometry." In: *J. Phys.: Condens. Mat.* 22 (2008), p. 324104.

[19] K. Hersvik. "Oil-oil droplet deformation under DC electric field as a method to investigate clay electrorheology." MA thesis. NTNU Trondheim, 2010.

[20] A. Mikkelsen. "Experimental studies of flow- and electric properties of oil droplets including suspended clay particles." MA thesis. NTNU Trondheim, June 2012.

[21] K. B. Kjerstad. "Clay-oil droplet suspensions in electric field." MA thesis. NTNU Trondheim, May 2012.

[22] H Block and J P Kelly. "Electro-rheology." In: *Journal of Physics D: Applied Physics* 21.12 (1988), p. 1661.

[23] Z. Rozynek. "Experimental Studies of Self-organization from Electrically Polarized Clay particles." PhD thesis. Norwegian University of Science and Technology, 2011.

[24] F. Bergaya, B. K. G. Theng, and G. Lagaly. *Handbook of Clay Science*. Developments in Clay Science. Elsevier Science, 2006. ISBN: 9780080441832.

[25] Jon Otto Fossum. "Physical phenomena in clays." In: *Physica A: Statistical Mechanics and its Applications* 270.1-2 (1999), pp. 270 –277.

[26] J. T. Kloprogge, S. Komarneni, and J. E. Amonette. "Synthesis of smectite clay minerals: a critical review." In: *Clays and Clay Minerals* 47.5 (1999), pp. 529–554.

[27] H. Hemmen et al. "X-ray studies of interlayer water absorption and mesoporous water transport in a weakly hydrated clay." In: *Phys. Rev. E* 82 (2010), p. 036315.

[28] G. J. da Silva et al. "Synchrotron x-ray scattering studies of water intercalation in a layered synthetic silicate." In: *Phys. Rev. E* 66 (1 July 2002), p. 011303.

[29] R. P. Tenório et al. "Intercalated Water in Synthetic Fluorhectorite Clay." In: *Langmuir* 26.12 (2010), pp. 9703–9709.

[30] H. Hemmen et al. "Erratum: X-ray studies of interlayer water absorption and mesoporous water transport in a weakly hydrated clay." In: *Phys. Rev. E* 83 (2011), p. 0019901.

[31] P. D. Kaviratna, T. J. Pinnavaia, and P. A. Schroeder. "Dielectric properties of smectite clays." In: *J. Phys. Chem. Solids* 57 (1996), pp. 1897–1906.

[32] W. Zhu et al. "Supramolecular ionic strength-modulating microstructures and properties of nacre-like biomimetic nanocomposites containing high loading clay." In: *RSC Advances* 2.15 (2012), p. 6295.

[33] BYK-Gardner GmbH. *Technical Information B-RI 21, Laponite, Performance Additives*. Jan. 2014. URL: http://www.byk.com/fileadmin/byk/additives/product_groups/rheology/former_rockwood_additives/technical_brochures/BYK_B-RI21_LAPONITE_EN.pdf.

[34] B. Wang et al. "Electrorheological properties of organically modified nanolayered laponite: influence of intercalation, adsorption and wettability." In: *J. Mater. Chem.* 19 (13 2009), pp. 1816–1828.

[35] A. Cadene et al. "Study of individual Na-montmorillonite particles size, morphology, and apparent charge." In: *Journal of Colloid and Interface Science* 285.2 (2005), pp. 719 –730.

[36] A. Khaldoun et al. "Quick Clay and Landslides of Clayey Soils." In: *Phys. Rev. Lett.* 103 (18 Oct. 2009), p. 188301.

[37] Y. Méheust, K. D. Knudsen, and J. O. Fossum. "Inferring orientation distributions in anisotropic powders of nano-layered crystallites from a single two-dimensional WAXS image." In: *Journal of applied crystallography* 39.5 (2006), pp. 661–670.

[38] P. G. de Gennes. *The physics of liquid crystals*. International series of monographs on physics. Clarendon Press, 1974. ISBN: 9780198512851.

[39] M. Doi and S.F. Edwards. *The Theory of Polymer Dynamics*. Oxford science publications. Oxford University Press, 1994.

[40] M. M. Schwartz. *Encyclopedia of smart materials*. Encyclopedia of Smart Materials v. 2. J. Wiley, 2002. ISBN: 9780471177807.

[41] E. DIMASI, J.O. FOSSUM, and G.J. DASILVA. "SYNCHROTRON X-RAY STUDY OF HYDRATION DYNAMICS IN THE SYNTHETIC SWELLING CLAY NA-FLUOROHECTORITE." In: July 2001.

[42] G. Taylor. "Studies in Electrohydrodynamics. I. The Circulation Produced in a Drop by Electrical Field." In: *Proceedings of the Royal Society of London. Series A. Mathematical and Physical Sciences* 291.1425 (1966), pp. 159–166.

[43] D. A. Saville. "ELECTROHYDRODYNAMICS:The Taylor-Melcher Leaky Dielectric Model." In: *Annual Review of Fluid Mechanics* 29.1 (1997), pp. 27–64.

[44] Paul F. Salipante and Petia M. Vlahovska. "Electrohydrodynamics of drops in strong uniform dc electric fields." In: *Physics of Fluids (1994-present)* 22.11 (2010),

[45] Z. Rozynek et al. "Electroformation of Janus and Patchy capsules." Submitted to Nat. Comm. (Under revision, March 2014). 2014.

8 List of Figures

Chapter 9

Papers

Electric field nematic alignment of fluorohectorite clay particles in oligomeric matrices

Zbigniew Rozynek[a)]
Department of Physics, NTNU, 7491 Trondheim, Norway

René C. Castberg
Physics Department, University of Oslo, 0316, Oslo, Norway

Alexander Mikkelsen
Department of Physics, NTNU, 7491 Trondheim, Norway

Jon Otto Fossum[b)]
*Department of Physics, NTNU, 7491 Trondheim, Norway; and The Centre for Advanced Study (CAS),
Norwegian Academy of Science and Letters, 0272, Oslo, Norway*

We study the behavior of fluorohectorite synthetic clay particles dispersed in paraffin wax. We report wide-angle x-ray scattering related to electric-field-induced alignment of the embedded clay particles. The development of anisotropic arrangement of the particles is measured during melting and crystallization of the composites. The degree of anisotropy is quantified by fitting azimuthal changes of the clay diffraction peak intensity to the Maier-Saupe function. This parametric function is then used to extract both the full width at half maximum (FWHM) and the amplitude of the anisotropic scattering and eventually to estimate a nematic order parameter for this system. Finally, the time evolution of the one-to-zero and zero-to-one water layer transition in paraffin embedded fluorohectorite clay galleries is presented, and we demonstrate that such particles can be used as "meso-detectors" for monitoring the local water content in bulk carrier matrices, such as paraffin wax.

I. INTRODUCTION

Clay particles have the ability to change and improve many physical properties, e.g., mechanical strength, thermal stability, conductivity, etc. of the medium in which they are suspended.[1–3] Some of these properties can be anisotropically enhanced if the particles are orientationally aligned in the host medium. Such a particle organization can be utilized as a molecular barrier, i.e., the permeability of gas molecules in polymer–clay composites are significantly reduced in the direction normal to clay platelet surfaces, whereas no change is expected for molecules propagating along the oriented clay surfaces. Yano et al.[4] report that only a 2 wt% addition of montmorillonite clay particles into polyimide may lower the gas permeability down to a value less than half of the pure polyimide gas permeability. Alignment of clay particles can be induced by planar shearing,[5] extrusion,[6] gravity,[7] and magnetic[8] or electric field.[9]

An electric field is often used to produce anisotropic structures to obtain desirable physical properties.

When polarizable particles are exposed to an electric field of either alternating current or direct current, dipoles will be induced and result in a rotational force on the particles in accordance with the Clausius–Mossotti relation.[10] The particle alignment can be monitored by means of x-ray or neutron diffraction,[11,12] and the degree of anisotropy can be quantified and expressed in terms of an order parameter S_2 (Refs. 7,13) (for details see Sec. III. A).

In previous studies by our group, the average orientational clay distribution was measured in a silicone oil system.[9,11] In the present study, the clay particles are instead dispersed in melted paraffin wax. There are some important differences between this system and the silicone oil system: the paraffin wax viscosity is significantly higher since the paraffin molecules are longer than the oil molecules, thus clay alignment is achieved at higher temperatures, i.e., between 65 and 100 °C, and is slower than for the silicone oil case. Therefore, in the present case of paraffin wax, we are able to monitor the increase of orientational order dynamically.

We are here also concerned with studying the amount of water that is intercalated inside clay galleries. It is well known that the swelling/shrinking of layered clay particles consists of changes in the basal spacing (*d*-spacing), and these changes can be monitored by means of x-ray diffraction. The amount of intercalated water is a function of

CAMBRIDGE JOURNALS J. Mater. Res., Vol. 28, No. 10, May 28, 2013 © Materials Research Society 2013 1349

http://journals.cambridge.org   Downloaded: 23 Oct 2013   IP address: 193.157.251.107

temperature and relative humidity (RH) of the clay surroundings. Hemmen et al.[14,15] showed that by measuring the basal spacing d, it is possible to (i) estimate a local humidity surrounding the clay particles, and thus (ii) monitor quasi-one-dimensional diffusion of water through the bulk sample, and finally (iii) extract profiles of RH along the sample. Here, we investigate the time-dependent changes in the intercalated water content of clays in both the melted state and the crystallized paraffin. This is the initial step for further measurements of anisotropic water diffusion through paraffin matrices with aligned clay particles.

The layout of this article is as follows: first, the sample preparation and the experimental procedures are explained in Sec. II. Wide-angle x-ray scattering results are presented in Sec. III, including alignment of clay particles in electric field and the development of the system anisotropy during melting and crystallization (Sec. III. A), time-dependent one-to-zero water layer transition (Sec. III. B), and finally, zero-to-one water layer transition (Sec. III. C). Conclusions and suggestions for further work are presented in Sec. IV.

II. SAMPLE DESCRIPTION, PREPARATION, AND EXPERIMENTAL PROCEDURES

A. Li-Fh clay particles

In this work, we have studied the synthetic clay fluorohectorite. There are several reasons for this choice. First, fluorohectorite is a 2:1 type clay with a crystallographic structure similar to that of some natural clay minerals such as montmorillonite.[16] Second, our group has studied fluorohectorite as a model system for clays[17–19] for many years and this system is thus understood and characterized in great detail.

Lithium fluorohectorite (Li-Fh) was purchased from Corning Inc., New York, in the form of a white powder. Li-Fh is a synthetic 2:1 smectite clay having the nominal chemical formula $Li^+_{1.2}[Mg_{4.8}Li_{1.2}Si_8O_{20}F_4]^{-1.2}$ per unit cell, where Li^+ is an interlayer exchangeable cation. Li-Fh has a surface charge of 1.2 e^-/unit cell and is a polydisperse clay with platelet diameters ranging from a few 100 nm up to a few µm.[18] A "single" particle consists of about 80–100 platelets (crystalline sheets)[14,15] that stack on top of one another. Since the thickness of such a stack is approximately 0.1 µm, the resulting particle has a diameter-to-height ratio on average close to 20:1. However, the single particles tend to agglomerate when dispersed into a nonpolar medium (oils, polymeric matrices, etc.) unless chemically modified.[20] Both the shape and the size of aggregated structures may vary, and in general, they depend on the clay type and sample preparation.[21–23] The Li-Fh clay mineral swells when it absorbs water. The swelling of layered 2:1 smectite clay particles is caused by a change in the basal spacing between crystalline sheets (d-spacing).[24]

B. Paraffin wax

Paraffin wax normally refers to a mixture of n-alkanes (chemical formula C_nH_{2n+2}) with n ranging between 20 and 40 determining the characteristic length of the molecules and also the melting temperature of the paraffin matrix. The material used for the present composite preparation was purchased from Sigma-Aldrich (ASTM D 127, batch: MKBC6750, Sigma-Aldrich Norway AS, Oslo, Norway). This particular type of paraffin wax has its melting point around 65 °C and was chosen due to the following reasons: (i) the x-ray peak positions related to the characteristic molecule dimensions should not overlap with clay reflections related to the interlamellar distance, (ii) optimal melting and crystallization temperatures providing both the ease of composite preparation and appropriate stiffness of the composite when in a solid form at room temperature, and (iii) the relatively nonpolar and nonconductive materials that can be used as an electrorheological carrier fluid for clay particles when in the melted state.

The characterization of the pure paraffin wax by means of x-ray scattering and rheometry is presented in the supporting materials (see Figs. S1 and S2).

C. Preparation of paraffin–clay composites

The first sample batch was prepared to monitor the dynamic alignment of clay particles during the composite melting and crystallization inside a custom-made heating cell. The sample batch was made as follows: 1.4 g of Li-Fh clay powder was slowly added into 7 g of premelted (90 °C) paraffin wax. After 10 min of stirring, the solution was left to rest for 3 min to allow the biggest clay particles to sediment. The top part (80% of the solution), consisting of the smallest clay particles, was then poured into a 10 mL glass phial (Procedure 1).

The solution was then kept at a temperature between 80 °C and 90 °C and stirred for 1 h to disperse clay particles within the paraffin. Finally, the solution was cooled down, and the solid cast was cut into small pieces that could fit inside the sample holder of the heating cell (see Fig. S3 in supporting material).

The second sample batch was prepared for in situ monitoring of the water content in clays embedded in paraffin matrix. In the first step, the composites were made following the Procedure 1 and then the solution was stabilized at a temperature around 120–130 °C under stirring. The temperature was higher for this batch compared with the first sample batch since we wish to monitor the time-dependent dehydration in clays, i.e., the one-to-zero water transition. Every hour, around 0.5 mL of solution was taken out to make a solid cast and x-rayed immediately after each composite had solidified. The same samples (stored in a solid form at room temperature and RH between 20% and 30%) were reexamined by x-ray scattering 6 months later to monitor changes in the water content.

1350 CAMBRIDGE JOURNALS   J. Mater. Res., Vol. 28, No. 10, May 28, 2013

http://journals.cambridge.org   Downloaded: 23 Oct 2013   IP address: 193.157.251.107

The dimensions of composites are $30 \times 6.5 \times 1.5$ mm^3. An example of a solid cast is shown in supporting Fig. S4. In all samples, the clay concentration was estimated to be around 5% by weight.

D. Wide-angle x-ray scattering experimental procedures

Investigations of the dynamic alignment of clay particles (Sample Batch 1) were performed at the European Synchrotron Radiation Facility (ESRF) in Grenoble, France. An x-ray beam with a wave length of 0.9 Å and a beam size of 0.3×0.3 mm^2 at the sample was used. The beamline BM01A is equipped with a two-dimensional (2D) MAR345 image plate detector with a diameter of 345 mm. The available scattering q-range is 0.03–1.6 Å^{-1}, where the scattering vector $q = 4\pi\sin(\theta/2)/\lambda$, given by the wave length λ of the incident beam and the scattering angle θ. The custom-made sample cell (Fig. S3) enabled precise control of heating and cooling in temperature range between 20 °C and 100 °C.

The second sample batch was investigated at our home laboratory (NTNU, Trondheim, Norway) using NanoSTAR from Bruker AXS setup in a wide-angle x-ray scattering (WAXS) mode. The instrument is equipped with a Cu K$_\alpha$ Xenocs microsource emitting x-rays at a wave length of 1.5418 Å and a 2D gas detector. The beam size at the sample is about 0.4 mm in diameter and the available scattering q-range for the setup is 0.08–1 Å^{-1}. The sample-to-detector distance was calibrated using a silver behenate standard.

III. RESULTS

A. Electric-field-induced alignment of clay particles

Figure 1 shows two examples of the 2D WAXS patterns from paraffin–clay composites without (left) and with (right) an applied external electric field. The outermost ring originates from the Bragg 001 reflection that corre-

sponds to the distance between clay's crystalline layers. It becomes anisotropic in the presence of an electric field due to clay particle alignment.

To quantify the degree of anisotropy of the system, i.e., how well the clay platelets align with respect to the electric field direction, one needs to integrate the 2D WAXS patterns (corresponding to the width of the 001 clay peak) radially over a narrow q-range and fit the obtained azimuthal plot to a parametric function. The Maier-Saupe function is commonly used for characterizing the orientational order in the field of liquid crystals.[25,26] It has previously been utilized for nematic-like dispersions of clay mineral particles,[27,28] and it has also been used successfully for characterizing electro-rheological alignment of clay particles.[9,11,13,23] Use of the Maier-Saupe function in the present case thus gives a direct comparison between the present system and the related previous work in this field. In short, the fitting parameter is a measure of the peak full width at half maximum, i.e., a smaller value equals a higher degree of anisotropy and can be expressed as the nematic order parameter S_2. The values of this parameter ranges from $-1/2$ to 1, where 1 indicates perfectly oriented platelet particles in the nematic configuration, 0 states no orientational order, and $-1/2$ indicates perfectly oriented platelets in the so-called antinematic configuration.[11,13,29]

We are expecting the clay particles to align in the antinematic fashion when an external electric field is applied. The validity of such an assumption is tested here by investigation of the clay particle alignment as a function of the rotation angle, i.e., the rotation axis is in the direction parallel to electric field lines. Ninety 2D WAXS images of the solidified sample were captured at different rotation angles with the rotation axis parallel to the electric field direction. Remark: we lack data points at angles 63° and 64°. The nematic order parameters were calculated for each sample position. The results are presented in Fig. 2, where S_2 values are plotted against the rotation angle. For measurements performed at rotational angles between 36° and 44°, the nematic order parameter displays a rather systematic deviation from the average observed S_2 values. Since the sample was cubic shaped, it is possible that the effective sample thickness in the x-ray beam direction is significantly larger at these rotational angles, thus contributing to more multiple scattering. For the measurements performed at other rotation angles, the S_2 values do not change considerably, indicating that there is no preferential orientation along the rotation angle, as represented by the arrowed disc being part of the plane normal to the electric field direction (see Fig. 2 inset). Thus, we can assume that the antinematic configuration applies for the clay particles in the present case.

To examine whether the alignment of clay particles may be disrupted during paraffin crystallization, the nano-particles' dispersion state was monitored during heating and

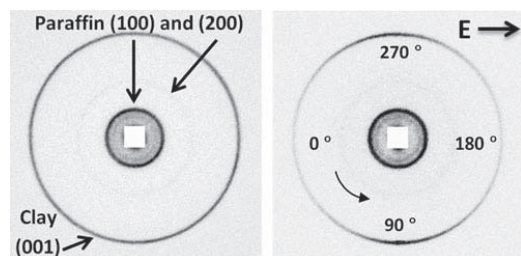FIG. 1. 2D WAXS patterns from paraffin–clay composites without (left) and with (right) an applied external electric field of 250 V/mm. The outermost ring from clay becomes anisotropic indicating that clay particles are aligned with their stacking direction perpendicular to the electric field lines.

CAMBRIDGE JOURNALS
http://journals.cambridge.org

J. Mater. Res., Vol. 28, No. 10, May 28, 2013

1351

FIG. 2. The nematic order parameter calculated for different rotation angles. The average S_2 value is indicated as a dashed line. The inset shows a sketch of the clay alignment in a so-called antinematic configuration (see text for details).

FIG. 3. Azimuthal plots of the first Bragg peak amplitude (001) measured at different times during the paraffin melting.

FIG. 4. Development of the anisotropy in the system expressed by changes in the nematic order parameter S_2.

cooling using the custom-made sample cell. X-ray diffractograms were first collected for samples at room temperature with no preferential orientation. Electric field (250 V/mm, 100 Hz, square wave) was applied from the beginning of the measurements, and it did not affect the samples while in solid form. Figure 3 shows 1D azimuthal plots (only 4 out of 64 measurements are shown for sake of clarity), where the 001 Bragg peak amplitudes (clay stacking) increase when paraffin melts and clay particles start aligning.

The scattered points are the experimental data, whereas the lines are the Maier-Saupe fits. The results of fitting are presented in Fig. 4. The nematic order parameter $S_2 = 0$ was ascribed by default for data points measured from 0 to 23 min since it was impossible to converge the 1D azimuthal plots with the fitting curve (as the black open circles in Fig. 3). The red curve shows the temperature measured 2 mm away from the sample.

The degree of anisotropy in the system increases when the paraffin starts melting and S_2 reaches a maximum value -0.36 at $t = 36$ min. Interestingly, as time passes, the anisotropy starts decreasing slightly and the value of S_2 changes by $\sim$15%, and it thus seems like a better particle alignment is achieved before individual particles start forming column-like structures. After 54 min, the sample was cooled down. It took around 5 min for paraffin to start crystallizing. A small drop in S_2 was observed during that time. This might be caused by the paraffin crystallization. The final measured nematic order parameter value (last minutes − solid sample) is −0.32. More measurements are needed to be more conclusive on these points.

Compared with particle alignment in clay/silicone oil-suspension (at room temperature) studied by our group previously, the characteristic rotation time τ_R (alignment of clay particles along the electric field lines) is longer in the present case since the paraffin wax is significantly more viscous than the silicone oil used in the previous work.[11] Recently, this rotation time has been shown to be proportional to E^2 and inversely proportional to the viscosity of the carrier fluid.[30] As reported in,[30] when particle is immersed in castor oil with the viscosity of $\sim$1 Pa s and exposed to $E = 250$ V/mm, it takes typically few seconds for a Fh clay aggregate (size: $\sim$1 $\times$ 0.1 $\times$ 0.05 mm) to rotate around 90° and align with its major axis along the electric field lines. Figure S1 shows that the viscosity of paraffin wax is significantly higher than that of the castor oil used in,[30] thus the rotation time is expected to be in range of minutes (before paraffin reaches T above 70 °C).
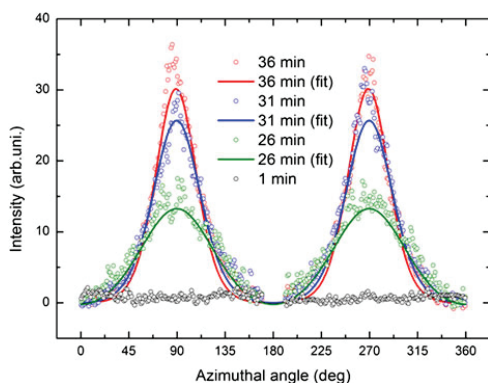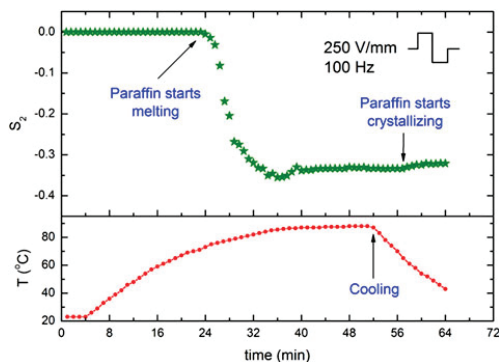
B. One-to-zero water layer transition

Water can intercalate in between each fluorohectorite platelet in the stack, causing the clay particle stack to swell. For Li-Fh, the intercalation process, which is temperature

1352   CAMBRIDGE JOURNALS   J. Mater. Res., Vol. 28, No. 10, May 28, 2013

http://journals.cambridge.org   Downloaded: 23 Oct 2013   IP address: 193.157.251.107

and RH dependent, yields four stable hydration states.[31,32] The structures, referred to as having 0, 1, 1.5, or 2 intercalated water layers, respectively, are quite well ordered along the stacking direction. The unit cell along the stacking direction is given by the distance between the stacked platelets, and the d-spacing in this direction is close to 10, 12, 13.5, and 1.5 Å for the case of 0 water layer (WL), 1 WL, 1.5 WL, and 2 WL, respectively.

The samples from the second batch were measured to investigate the time-dependent changes in the water content intercalated between the clay's crystalline sheets. The recorded x-ray data allow monitoring of the evolution of one-to-zero and zero-to-one WL transitions.

Figure 5 shows azimuthally integrated 2D WAXS patterns from six samples prepared at different times, namely for 0, 2, 3, 5, 7, and 10 h of stirring at elevated temperature around 120–130 °C. Initially, the clay particles (kept at room temperature and ambient humidity, in a form of powder) were in the pure 1 WL hydration state (first measurement − blue dotted curve). The corresponding 001 Bragg peak is located at 12.1 Å. After 2 h, the 1 WL peak intensity decreased and a new, broad and not yet distinct peak appeared at the q-value corresponding to the 0 WL hydration state. Both peaks are shifted from their initial ($d_{100}^{1WL} = 12.1$ Å) and final ($d_{100}^{0WL} = 10.3$ Å) positions toward lower and higher values ($d_{100}^{1WL} = 11.9$ Å and $d_{100}^{0WL} = 10.7$ Å), respectively. The intensity of the peak related to the 0 WL state increases with time and becomes sharper. After 5 h, the population of clay particles in the scattering volume contains a significantly higher proportion of 0 WL over 1 WL spacing. The clay particles need almost 10 h to reach the nearly pure 0 WL hydration final state (red curve with triangles). A minor population of clay particles possessing the intercalated water is still present but is hardly detectable by our instrument.

The interlayer hydration states occurring in smectite clays are pure water layer states [i.e., 0 WL, 1 WL, (1.5 WL), and 2 WL], and in addition Hendricks–Teller mixed hydration states occur as reported by Michels et al.[33] Recently, Hemmen et al.[14,15] thoroughly mapped systematic changes in the d-spacing values within the pure WL states as a function of RH and investigated the 1-to-2 WL transition. In the present case, the 1-to-0 WL transition was monitored. The maximum values of the smooth changes in the d-spacing, with respect to both the initial and the final states (1 WL → 0 WL), are in the order of approximately 0.3 Å for deviation from 1 WL and 0.5 Å for deviation from 0 WL. These values are similar to those that reported by Hemmen et al.[14,15]

C. Zero-to-one water layer transition

The samples described in Sec. III. B (dehydrated to a different extend) were stored at room temperature and RH between 20% and 30% for 6 months and then x-rayed to monitor the water contents.

The time 2:1 smectite clays require to hydrate depends on RH and temperature together with the size and charge of the exchangeable cation in the interlayer space. For powdered samples, the time evolution magnitude is in the order of hours.[34–37] However, the time needed for the entire clay population (inside the paraffin wax) to reach the 1 WL state is considerably longer. The effective RH around embedded clay particles is low since the water penetration through the oligomer matrix is restrained.

Figure 6 shows $I_1/(I_1 + I_2)$ magnitude ratios for 0 WL and 1 WL peak intensities for six samples from the second sample batch. The ratio values are in the range of 0–1, where 0 indicates a pure dehydrated state, 0.5 is obtained when the number of clay particles in the two states is equal, and 1 depicts the pure monohydrated state. Green squared data points were acquired from measuring samples right

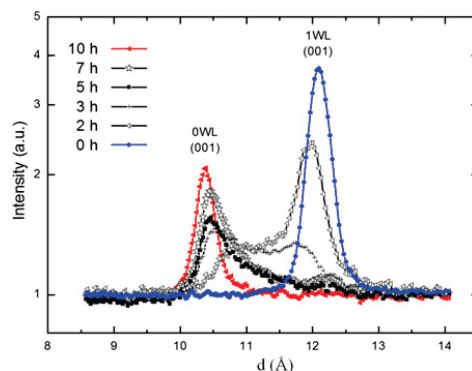FIG. 5. Time evolution of the one-to-zero WL transition (Sample Batch 2).
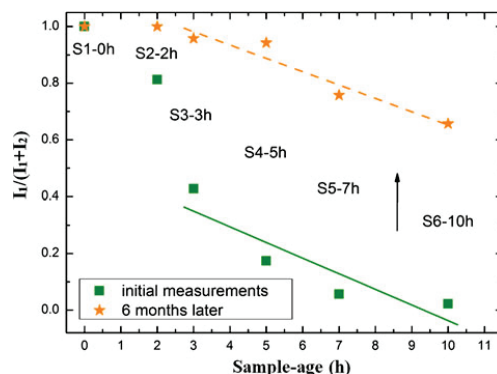

FIG. 6. The ratios $I_1/(I_1 + I_2)$ between magnitudes of 0 WL and 1 WL peak intensities for six samples (Sample Batch 2). Their values are in the range of 0–1, where 0 indicates the pure dehydrated state, 0.5 is obtained when the number of clay particles in the two states are equal, and 1 depicts the pure monohydrated state.

after their preparation (as shown also in Fig. 5). Orange star data points were obtained from the same samples, measured 6 months later. For all samples (S1–0 h omitted in this discussion), water molecules intercalate into the clay galleries. However, the complete recovery from a partially dehydrated state (0 WL) to a monohydrated state (1 WL) was only accomplished by the sample labeled S2–2 h. By comparing the intensity ratio values, it can be concluded that the remaining four samples absorbed comparable amounts of water. The two lines in Fig. 6 were obtained by fitting the data points to a linear function $I_1/(I_1 + I_2) = a + bx$. The calculated values of the slope b were very similar for the two sets, i.e., -0.05 ± 0.02 and -0.06 ± 0.02 for the (dashed) orange and (solid) green curves, respectively.

IV. CONCLUSIONS

We have investigated the electric field-induced alignment of fluorohectorite clay particles in oligomeric matrices, and the development of the system anisotropy was observed during paraffin melting and crystallization. Interestingly, it was found that on average, the clay particles loose some of their orientational order to accommodate chain formation.

The dehydration of clay particles as a function of time was also investigated, and our observations show that it takes almost 10 h for the clay particles in the melted wax to reach the pure 0 WL hydration final state. However, the zero-to-one WL transition for clay particles being embedded in crystallized paraffin is very slow. This is due to a very low water penetration through the oligomer matrix. Even after 6 months with air exposure, the sample still contains a population of clay particles possessing no or very little intercalated water. This suggests that such embedded clay particles can be used as "meso-detectors" for monitoring the local water content in such bulk carrier matrices. We plan future work in this direction including investigations of possibly anisotropic water diffusion through paraffin matrices with aligned clay particles.

REFERENCES

1. H.J. Walls, M.W. Riley, R.R. Singhal, R.J. Spontak, P.S. Fedkiw, and S.A. Khan: Nanocomposite electrolytes with fumed silica and hectorite clay networks: Passive versus active fillers. *Adv. Funct. Mater.* **13**, 710–717 (2003).
2. S.H. Kim, J. Eun-Ju, Y. Jung, M. Han, and S.J. Park: Ionic conductivity of polymeric nanocomposite electrolytes based on poly(ethylene oxide) and organo-clay materials. *Colloids. Surf., A* **313**, 216–219 (2008).
3. D. Ratna, S. Divekar, A.B. Samui, B.C. Chakraborty, and A.K. Banthia: Poly(ethylene oxide)/clay nanocomposite: Thermomechanical properties and morphology. *Polymer* **47**, 4068–4074 (2006).
4. K. Yano, A. Usuki, A. Okada, T. Kurauchi, and O. Kamigaito: Synthesis and properties of polyimide-clay hybrid. *J. Polym. Sci., Part A: Polym. Chem.* **31**, 2493–2498 (1993).
5. M. Okamoto, P.H. Nam, P. Maiti, T. Kotaka, T. Nakayama, M. Takada, M. Ohshima, A. Usuki, N. Hasegawa, and H. Okamoto: Biaxial flow-induced alignment of silicate layers in polypropylene/clay nanocomposite foam. *Nano Lett.* **1**, 503–505 (2011).
6. X. He, J. Yang, L. Zhu, B. Wang, G. Sun, P. Lv, I.Y. Phang, and T. Liu: Morphology and melt rheology of nylon 11/clay nanocomposites. *Appl. Polym. Sci.* **102**, 542–549 (2006).
7. H. Hemmen, N.I. Ringdal, E.N. De Azevedo, M. Engelsberg, E.L. Hansen, Y. Méheust, J.O. Fossum, and K.D. Knudsen: The isotropic-nematic interface in suspensions of Na-fluorohectorite synthetic clay. *Langmuir* **25**, 12507–12515 (2009).
8. E.N. De Azevedo, M. Engelsberg, J.O. Fossum, and R.E. de Souza: Anisotropic water diffusion in nematic self-assemblies of clay nanoplatelets suspended in water. *Langmuir* **23**, 5100–5105 (2007).
9. J.O. Fossum, Y. Méheust, K.P.S. Parmar, K.D. Knudsen, K.J. Måløy, and D.M. Fonseca: Intercalation-enhanced electric polarization and chain formation of nano-layered particles. *Europhys. Lett.* **74**, 438–444 (2006).
10. Y.P. Huang, M.J. Lee, M.K. Yang, and C.W. Chen: Montmorillonite particle alignment and crystallization and ion-conducting behavior of montmorillonite/poly(ethylene oxide) nanocomposites. *Appl. Clay Sci.* **49**, 163–169 (2010).
11. Z. Rozynek, K.D. Knudsen, J.O. Fossum, Y. Méheust, B. Wang, and M. Zhou: Electric field induced structuring in clay–oil suspensions: New insights from WAXS, SEM, leak current, dielectric permittivity, and rheometry. *J. Phys. Condens. Matter* **22**, 324104 (2010).
12. K.D. Knudsen, J.O. Fossum, G. Helgesen, and M.W. Haakestad: Small-angle neutron scattering from a nano-layered synthetic silicate. *Physica B* **352**, 247–258 (2004).
13. Y. Méheust, K.D. Knudsen, and J.O. Fossum: Inferring orientation distributions in anisotropic powders of nano-layered crystallites from a single two-dimensional WAXS image. *J. Appl. Cryst.* **39**, 661–670 (2006).
14. H. Hemmen, L.R. Alme, J.O. Fossum, and Y. Méheust: X-ray studies of interlayer water absorption and mesoporous water transport in a weakly hydrated clay. *Phys. Rev. E* **82**, 036315 (2010).
15. H. Hemmen, L.R. Alme, J.O. Fossum, and Y. Méheust: Erratum: X-ray studies of interlayer water absorption and mesoporous water transport in a weakly hydrated clay. *Phys. Rev. E* **83**, 019901 (2011).
16. P.D. Kaviratna, T.J. Pinnavaia, and P.A. Schroeder: Dielectric properties of smectite clays. *J. Phys. Chem. Solids* **57**, 1897–1906 (1996).
17. J.O. Fossum: Physical phenomena in clays. *Physica A* **270**, 270–277 (1999).
18. J.O. Fossum: Flow of clays. *Eur. Phys. J. Spec. Top.* **204**, 41–56 (2012).

1354   CAMBRIDGE JOURNALS   J. Mater. Res., Vol. 28, No. 10, May 28, 2013

http://journals.cambridge.org   Downloaded: 23 Oct 2013   IP address: 193.157.251.107

19. E.L. Hansen, H. Hemmen, D.M. Fonseca, C. Coutant, K.D. Knudsen, T.S. Plivelic, D. Bonn, and J.O. Fossum: Swelling transition of a clay induced by heating. *Sci. Rep.* **2**, 618 (2012).

20. B. Wang, M. Zhou, Z. Rozynek, and J.O. Fossum: Electrorheological properties of organically modified nanolayered laponite: Influence of intercalation, adsorption and wettability. *J. Mater. Chem.* **19**, 1816–1828 (2009).

21. Z. Rozynek, T. Zacher, M. Janek, M. Čaplovičová, and J.O. Fossum: Electric-field-induced structuring and rheological properties of kaolinite and halloysite clays. *Appl. Clay Sci.* **77-78**, 1–9 (2013).

22. Z. Rozynek, B. Wang, J.O. Fossum, and K.D. Knudsen: Dipolar structuring of organically modified fluorohectorite clay particles. *Eur. Phys. J. E* **35**, 9 (2012).

23. Z. Rozynek, H. Mauroy, R.C. Castberg, K.D. Knudsen, and J.O. Fossum: Dipolar ordering of clay particles in various carrier fluids. *Rev. Cub. Fis.* **29**, 1E37–41 (2012).

24. G.J. Silva, J.O. Fossum, E. DiMasi, K.J. Måløy, and S.B. Lutnæs: Synchrotron x-ray scattering studies of water intercalation in a layered synthetic silicate. *Phys. Rev. E* **66**, 011303 (2002).

25. P.G. De Gennes: *The Physics of Liquid Crystals* (Clarendon Press, Oxford, 1979).

26. W. Maier and A. Saupe: Eine einfache molekulare theorie des nematischen kristallinflussigen zustandes. *Z. Naturforsch. A* **13**, 564 (1958).

27. B.J. Lemaire, P. Panine, J.C.P. Gabriel, and P. Davidson: The measurement by SAXS of the nematic order parameter of laponite gels. *Europhys. Lett.* **59**, 55–61 (2002).

28. I. Bihannic, C. Baravian, J.F.L. Duval, E. Paineau, F. Meneau, P. Levitz, J.P. de Silva, P. Davidson, and L.J. Michot: Orientational order of colloidal disk-shaped particles under shear-flow conditions: Rheological-small-angle x-ray scattering study. *J. Phys. Chem. B* **114**, 16347–16355 (2010).

29. I. Dozov, E. Paineau, P. Davidson, K. Antonova, C. Baravian, I. Bihannic, and L.J. Michot: Electric-field-induced perfect anti-nematic order in isotropic aqueous suspensions of a natural Beidellite clay. *J. Phys. Chem. B* **115**, 7751–7765 (2011).

30. R.C. Castberg, Z. Rozynek, J.O. Fossum, K.J. Måløy, P. Dommersnes, and E.G. Flekkøy: Clay alignment in electric fields. *Rev. Cub. Fis.* **29**, 1E17–19 (2012).

31. R.P. Tenorio, M. Engelsberg, J.O. Fossum, and G.J. da Silva: Intercalated water in synthetic fluorhectorite clay. *Langmuir* **26**, 9703–9709 (2010).

32. T.J. Tambach, P.G. Bolhuis, E.J.M. Hensen, and B. Smith: Hysteresis in clay swelling induced by hydrogen bonding: Accurate prediction of swelling states. *Langmuir* **22**, 1223–1234 (2006).

33. L.E. Michels, H. Hemmen, R. Droppa Junior, G. Grassi, G.J. Silva, and J.O. Fossum: Synchrotron x-ray scattering studies of Li-fluorohectorite synthetic clay: Random intercalation states. In *Proceedings of 2nd International Workshop on Complex Physical Phenomena in Materials*, J.O. Fossum and G.L. Vasconcelos, eds. complexphysics.org, 2012; p. 31–34.

34. E. DiMasi, J.O. Fossum, and G.J. da Silva: Synchrotron x-ray study of hydration dynamics in the synthetic swelling clay Na-fluorohectorite. In *Proceedings of the 12th International Clay Conference, Argentina*, E. Dominguez, G.R. Mas and F. Cravero, eds. Elsevier Science BV: Amsterdam, Netherlands, 2003.

35. N. Wada, D.R. Hines, and S.P. Ahrenkiel: X-ray diffraction studies of hydration transitions in Na vermiculite. *Phys. Rev. B* **41**, 12895–12901 (1990).

36. R.W. Mooney, A.G. Keenan, and L.A. Wood: Adsorption of water vapor by montmorillonite. Effect of exchangeable ions and lattice swelling as measured by x-ray diffraction. *J. Am. Chem. Soc.* **74**, 1371–1374 (1952).

37. G. Løvoll, B. Sandnes, Y. Méheust, K.J. Måløy, J.O. Fossum, G.J. da Silva, M.S.P. Mundim, R. Droppa, Jr., and D.M. Fonseca: Dynamics of water intercalation fronts in a nano-layered synthetic silicate: A synchrotron x-ray scattering study. *Physica B* **370**, 90–98 (2005).

38. G. Strobl: *The Physics of Polymers*, 2nd ed. (Springer, New York, NY, 1997), pp. 143–144.

39. E. Sirota, H. King, D. Singer, and H. Shao: Rotator phases of the normal alkanes: An x-ray scattering study. *J. Chem. Phys.* **98**, 5809–5824 (1993).

40. G. Ungar: Structure of rotator phases in n-alkanes. *J. Phys. Chem.* **87**, 689–695 (1983).

41. M.J. Nowak and S.J. Severtson: Dynamic mechanical spectroscopy of plastic crystalline states in n-alkane systems. *J. Mater. Sci.* **36**, 4159–4166 (2001).

42. A.E. Smith: The crystal structure of the normal paraffin hydrocarbons. *J. Chem. Phys.* **21**, 2229–2231 (1953).

Supplementary Material

Supplementary materials can be viewed in this issue of the *Journal of Materials Research* by visiting http://journals.cambridge.org/jmr.

CAMBRIDGE JOURNALS

http://journals.cambridge.org

J. Mater. Res., Vol. 28, No. 10, May 28, 2013

Downloaded: 23 Oct 2013

IP address: 193.157.251.107

1355

Supporting materials
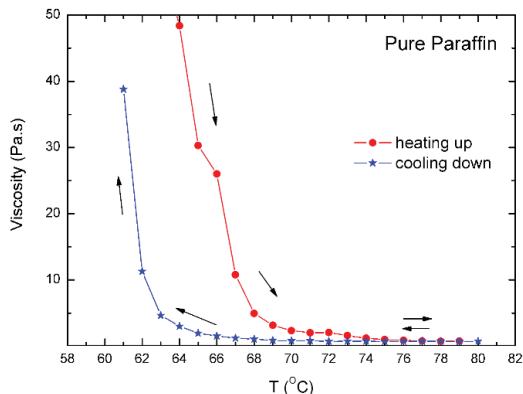
Figure S1. Rheological data showing both the melting and the crystallization transition temperatures for pure paraffin wax used in the present studies, see text.

Prior to the composite preparation, the melting point of the pure paraffin-wax was measured by employing the Physica MCR 300 Rotational Rheometer equipped with a coaxial cylindrical cell C27/ERD. The crystalline melting temperature appeared around 65 ºC, as shown in Fig. S1. The temperature range where crystallization occurs, and consequently, also the range of melting during the subsequent heating, are broad. The observed hysteresis width is additionally broadened by the fast heating rate of 1 ºC/min.

Complementary information about pure paraffin is provided by wide angle X-ray diffraction measurements, where diffractograms were collected for the sample during the solid-to-liquid transition. In the solid form, the paraffin-wax has a crystal structure that is composed of stacked layers of disentangled molecules, each layer being assembled of chain molecules with identical helical conformations **[38]**. However, when heated up, they take on coiled conformations just like polymers and the regular structure is lost. Figure S2 shows the X-ray diffractograms of pure paraffin-wax during heating from 25 to 85 °C. Each X-ray diffractogram has been captured with an exposure time of 1 min, and during that time the sample temperature changes as indicated in the legend. The characteristic peaks attributed to the lengths of the oligomer molecules start shifting and decreasing at a temperature range between 60 and 75 °C. They vanish completely for higher temperatures, indicating a loss of crystallinity. For more details about paraffin-waxes, their different structural phases, solid-liquid phase transitions, positional and orientational order, viscoelastic behaviour, etc., the reader is referred to the literature **[39-42]**.
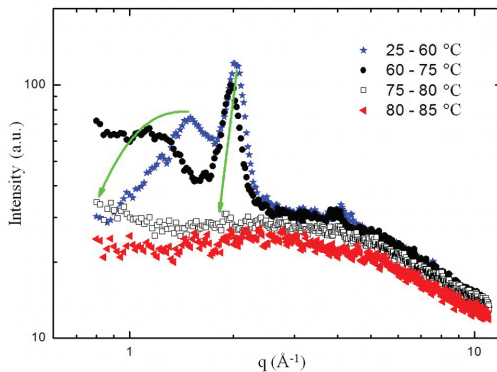
Figure S2. X-ray diffractograms of pure paraffin-wax during heating from 25 to 85 °C. The characteristic peaks attributed to the lengths of the oligomer molecules start shifting and decreasing at temperature range between 60 and 75 °C. They vanish completely for higher temperatures, indicating a loss of crystallinity.
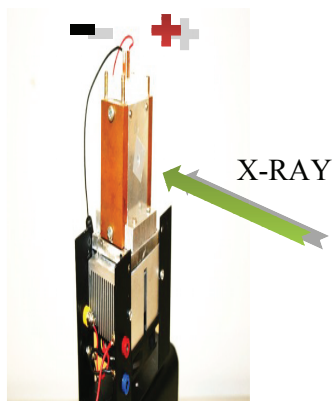
Figure S3. Experimental setup for studying dynamic alignment of clay particles during melting and crystallization of clay/paraffin-wax composites.
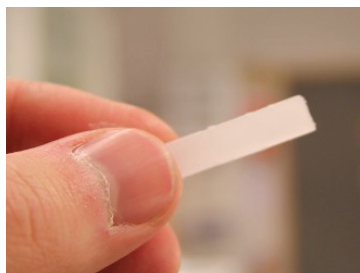
Figure S4. Paraffin/clay composite with a 30 x 6.5 x 1.5 mm³ dimension.

CLAY ALIGNMENT IN ELECTRIC FIELDS

ALINEACIÓN DE ARCILLAS EN CAMPOS ELÉCTRICOS

R. C. Castberg[a †], Z. Rozynek[b], J. O. Fossum[b,d ‡], K. J. Måløy[a,d *], P. Dommersnes[c,d] and E. G. Flekkøy[a,d]

a) Department of Physics, University of Oslo, P.O. Box 1048, NO-0316, Oslo, Norway,
rene@castberg.org[†], k.j.maloy@fys.uio.no[*]
b) Department of Physics, NTNU, Høgskoleringen 5, NO-7491, Trondheim, jon.fossum@ntnu.no[‡]
c) Matieres et Systemes Complexes, Universite Paris 7, 75253, Paris, France
d) Centre for Advanced Study at the Norwegian Academy of Science and Letters, Drammensveien 78, NO-0271 Oslo, Norway
†, ‡, * corresponding authors

The response of rotational alignment of lithium fluorohectorite (Li-Fh) to an external electric field has been studied by employing image analysis. Large aggregates consisting of many single clay particles were prepared using a sedimentation technique in order to control both their shapes and sizes. Such aggregates have a layered structure which was confirmed by wide-angle X-ray scattering (WAXS) studies. Measuring the electric-field-induced alignment of these particles we obtained a data collapse by plotting $\ln(\theta)$ versus t/E^2, where θ is the rotational angle, t is time and E is the electric field strength.

Se estudia la respuesta de la alineación rotacional de la fluorohectorita de litio (Li-Fh) debido a un campo eléctrico externo mediante análisis de imágenes. Se prepararon grandes agregados consistentes en muchas partículas individuales de arcilla usando una técnica de sedimentación, con el objetivo de controlar tanto sus formas como sus tamaños. Tales agregados poseen una estructura a capas, lo que fue confirmado por dispersión de rayos X de ángulo ancho (WAXS). Midiendo el alineamiento inducido por campo eléctrico de las partículas, obtuvimos un colapso de los datos en un gráfico $\ln(\theta)$ vs. t/E^2 donde θ es el ángulo de rotación, t es el tiempo, y E es la intensidad del campo eléctrico.

INTRODUCTION

On application of an external electric field, clay particles suspended in non-polar and non-conductive carrier fluids (such as silicone oil) will rotate and align themselves [1] such that their stacking direction is normal to the electric field direction. Once these particles have aligned themselves, they will eventually start forming chain-like structures [2, 3, 4]. In order to understand the processes behind chain formation, we have to understand how the individual particles initially orient themselves with the field. From preliminary observations, we find that for small particles this process takes a couple of *ms*, for this reason we prepared larger particles which were easier to manipulate. In this work optical measurements were made of the particles aligning themselves in the electric field and we show that there is a E^2 dependency on the rotation rate.

SAMPLE PREPARATION

Lithium fluorohectorite (Li-Fh) was purchased from Corning Inc., New York in the form of a white powder. Li-Fh is a synthetic 2:1 smectite clay having the nominal chemical formula $Li^+_{1.2}[[Mg_{4.8}Li_{1.2}]Si_8O_{20}F_4]^{1.2-}$ per unit cell, where Li is an interlayer exchangeable cation (not to confuse with Li in the crystaline sheet); for more details on structure see reference [5]. Li-Fh has a surface charge of 1.2 e-/unit cell and is a polydisperse clay with platelet diameters ranging from a few hundred *nm* up to several μm [6]. In order to have a better control on the particle shape

and size (parameters that may influence the rotation time when particles are subjected to *E*-fields), it was decided to prepare the samples as follows. The Li-Fh powder was mixed with deionized water and stirred for 12 *h* at RT. Next, the solution was transferred to a flat Petri dish and then left for 3 days at RT for water evaporation. During that time the individual clay particles sediment, and generally lie flat on the bottom of the dish and consequently stack on one another as sketched in Figure 2 (a). In order to obtain different particle thicknesses' four different clay concentrations were used, namely 0.5, 1, 2 and 4 *wt.*%. In this proceeding we will present data from the 2 *wt.*%. Once the samples have dried, they were carefully cut into small pieces with desired lengths and widths (see Figure 1).
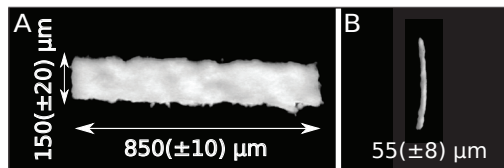

Figure 1: Optical microscopy images of the sample showing length of around 0.85 *mm* (A) and thickness of around 55 μm (B).

SAMPLE CHARACTERISATION

The sample shown in Figure 1, with thickness of around

55 μm, was measured at our home laboratory (NTNU, Norway) using a NanoSTAR X-ray instrument from Bruker AXS, setup in a wide-angle X-ray scattering (WAXS) configuration during the present experiments. This instrument is equipped with a CuKα micro-source emitting X-rays at wavelength of 1.5418 $\mathring{A}$; and a 2-D detector that collects Bragg diffraction rings. The equipment enabled the investigation of both the orientational distribution of the clay platelet stacks and the characteristic interlamellar distance for monitoring the intercalated water content. The X-ray beam is directed such that it is normal to the sedimentation direction, as shown in Figure 2 (a), i.e. the thickness of the particle. The beam has a diameter of about 0.4 mm and the available scattering q-range for the setup used here was: 0.08 - 1 $\mathring{A}^{-1}$.
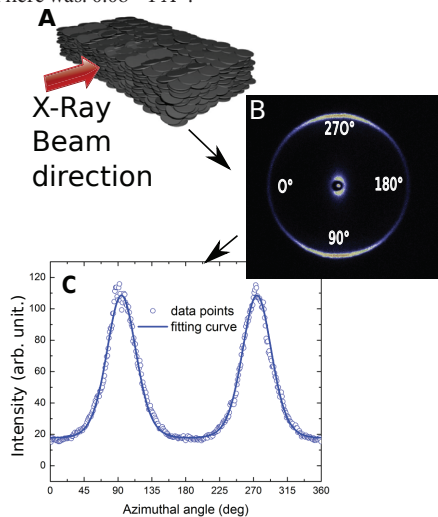
Figure 2: (A) Clay platelets forming an aggregate, (B) resulting in an asymmetry in the WAXS data. (C) The azimuthal plot is made by radial integration of the 2-D WAXS pattern. The parametric fit (solid line) is used to calculated the nematic order parameter (here S_2 = -0.34 ± 0.02).

An example of the two-dimensional WAXS pattern is shown in Figure 2 (b). The 001 Bragg ring that originates from the clay interlamellar distance (between clay crystalline sheets) is anisotropic indicating that the clay particles have a preferential orientation. Since the scattering intensity peaks at 90º and 270º and the direction of the X-ray beam is horizontal, one can conclude that the clay particles are oriented with their stacking direction normal to the X-ray beam, as sketched in Figure 2 (a). When the 2-D WAXS pattern is integrated along the radial direction with a narrow q-range (2θ-angle) around the Bragg ring, one can obtain a 1-D azimuthal plot, as presented in Figure 2(c). This can be fitted to a parametric function (such as Maier-Saupe, see [7, 8]) in order to calculate the nematic order parameter (S_2), which is a qualitative measure of the clay particles' orientation distribution. In this case, the S_2 was found to be -0.34 ± 0.02 (remark: S_2 = 0 and S_2 = -0.5 indicate no preferential orientation and perfect alignment, respectively).

EXPERIMENTAL SET-UP AND ANALYSIS

The experimental set-up is sketched in Figure 3. Castor oil was used as a hosting liquid to fill the cell. The castor oil has a high viscosity (~ 1000 cSt), ensuring that the particles rotate slowly enough to obtain accurate data. The particle is placed in the centre of the cell such that it is completely surrounded by the castor oil. Initially the particle (prepared as described in the sample preparation section) is aligned with the major axis normal to the electric field, and the narrowest side aligned parallel to the electric field. When the field is then applied the particle starts to rotate such that the major axis is eventually aligned parallel to the field. Each measurement is filmed at 30 fps and then the recording is processed using MATLAB by tracking the particle from frame to frame (using the regionprops function). Its angle is calculated by fitting an ellipse to the particle and measuring the angle of the major axis. For each of the measured field strengths the same particle was used, ensuring that the experiments were as similar as possible.
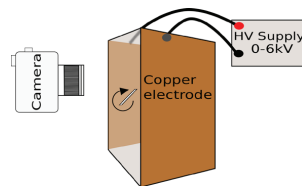
Figure 3: Experimental setup: A video camera is used to film the rotating particle in a glass cell. The two copper electrodes are connected to a high voltage supply capable of supplying up to 5 kV DC. Resulting in an electric field of up to 500 V/mm.

RESULTS AND DISCUSSION

The results for tracking the same particle at different field strengths can be seen in Figure 4. In this plot we see the angle of the particle plotted against the time. It can be clearly seen that the rotation time for the lowest fields (100 V/mm) are considerably longer than for the highest fields (500 V/mm).
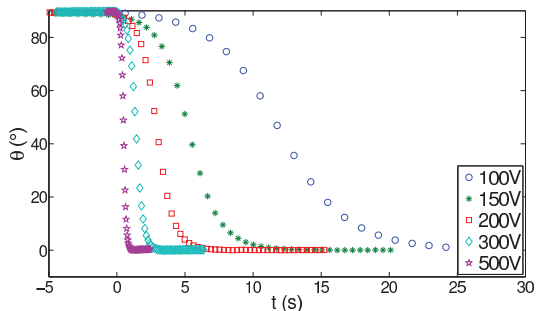
Figure 4: Angle of rotation for a single particle at different electric field strengths. Particle size: $0.85 \times 0.15 \times 0.055$ mm

This is expected as there is an equilibrium between the torque (T) applied from the electric field and the drag of the oil. The torque due to drag in the rotational plane can be written as[9]:

$$T_d = -\zeta_{rot}\dot{\theta},\tag{1}$$

where ζ_{rot} is the specific rotational drag coefficient in the plane the particle rotates.

The torque due to the electric field is [10,11]

$$\vec{T}_E = (\bar{\chi}\vec{E})\times\vec{E},\tag{2}$$

which can then be written as

$$T_E = \chi_0 E^2 \sin(\theta)\cos(\theta),\tag{3}$$

where χ_0 is the effective polarizability involving geometric factors. As the data is for the same particle, i.e. the shape and structure are the same, χ_0 is considered a constant.
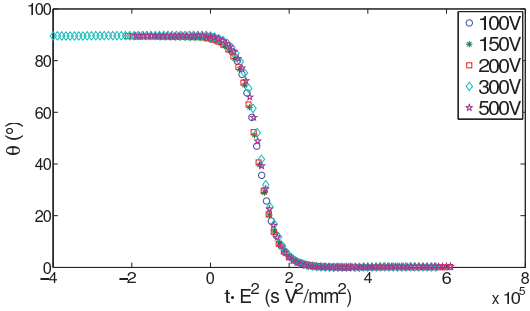
Figure 5: Data collapse of Figure 4, θ plotted against time multiplied by E^2 for different field strengths. Particle size: $0.85 \times 0.15 \times 0.055$ mm

We are operating in the low Reynolds number regime ($Re < 0.01$), and can ignore any inertial effects, hence the electric torque balances the hydrodynamic torque giving

$$\dot{\theta} = -\frac{\chi_0 E^2}{2\zeta_{rot}}\sin(2\theta) = -\frac{1}{2\tau}\sin(2\theta)\tag{4}$$

and thus we obtain

$$\tau \propto \frac{1}{E^2}\tag{5}$$

This is confirmed by way of a data collapse by plotting θ against $t \cdot E^2$, where t is the time and E is the field strength. This can be seen in Figure 5. We should note that we have not treated the anisotropic effects of the dipole that would be encountered as the cylinder rotates. For a more detailed study the reader is referred to Doi and Edwards [9] Solving equation Eq. (4) results in

$$\ln\left(\frac{\tan(\theta)}{\tan(\theta_0)}\right) = -\frac{t - t_0}{\tau},\tag{6}$$

where t_0 is the time the field is applied, and the corresponding angle $\theta_0 = \theta(t_0)$. We can observe this in Figure 6 where we plot $\ln(\tan(\theta))$ against $t \cdot E^2$ and can see an exponential cut-off, with a slope of -3.4×10^{-5}.

CONCLUSION

From the data we can clearly see that θ scales with time as E^2 as the electric field strength is changed. In future work we wish to determine the effect of the particle geometry, and how multiple water layers affect the rotation time, as in these experiments we only had 1 water layer, and whether the intercalated cations contribute to the dipole moment.
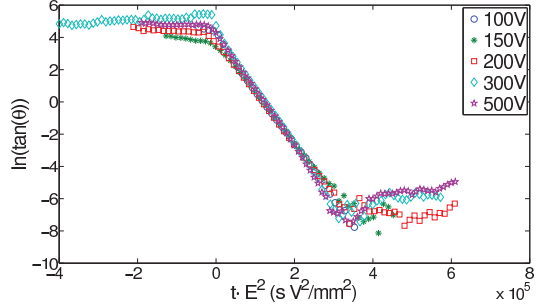
Figure 6: Data collapse of Figure 4, $\ln(\tan(\theta))$ plotted against time multiplied by E^2 for different field strengths. Particle size: $0.85 \times 0.15 \times 0.055$ mm

[1] J. O. Fossum, Y. Méheust, K. P. S. Parmar, K. D. Knudsen, K. J. Måløy and D. M. Fonseca, Europhys. Lett. **74**, 438 (2006).

[2] B. Wang, M. Zhou, Z. Rozynek and J. O. Fossum, J. Mater. Chem. **19**, 1816 (2009).

[3] Z. Rozynek, K. D. Knudsen, J. O. Fossum, Y. Méheust, B. Wang and M. Zhou, J. Phys: Condens. Mat. **22**, 324104 (2008).

[4] Z. Rozynek, H. Mauroy, R. C. Castberg, K. D. Knudsen and J. O. Fossum, Rev. Cub. Fis. **29**, 1E37 (2012).

[5] H. Hemmen, L. R. Alme, J. O. Fossum and Y. Méheust, Phys. Rev. E **82**, 036315 (2010).

[6] P. D. Kaviratna, T. J. Pinnavaia and P. A. Schroeder, J. Phys. Chem. Solids **57**, 1897 (1996).

[7] Y. Méheust, K. D. Knudsen and J. O. Fossum, J. Appl. Cryst. **39**, 661 (2006).

[8] Z. Rozynek, B. Wang, J. O. Fossum and K. D. Knudsen, Eur. Phys. J. E. **35**, 9 (2012).

[9] M. Doi and S. Edwards, *The Theory of Polymer Dynamics*, (Oxford University Press, USA, 1986).

[10] P. Zijlstra, M. van Stee, N. Verhart, Z. Gu and M. Orrit, Phys. Chem. **14**, 4584 (2012).

[11] H-Y Hsu, N. Sharma, R. S. Ruoff and N. A. Patankar, Nanotechnology **16**, 312 (2005).

DIPOLAR ORDERING OF CLAY PARTICLES IN VARIOUS CARRIER FLUIDS

ORDENAMIENTO DIPOLAR DE PARTÍCULAS DE ARCILLA EN DIVERSOS FLUIDOS

Z. Rozynek[a †], H. Mauroy[b], R. C. Castberg[c], K. D. Knudsen[b] and J. O. Fossum[a,d ‡]

a) Department of Physics, NTNU, Høgskoleringen 5, NO-7491 Trondheim, Norway, rozynek@ntnu.no[†], jon.fossum@ntnu.no[‡]
b) Physics Department, IFE, NO-2027 Kjeller, Norway
c) Department of Physics, University of Oslo, P.O.Box 1048, NO-0316 Oslo, Norway
d) Centre for Advanced Study at the Norwegian Academy of Science and Letters, Drammensveien 78, NO-0271 Oslo, Norway
†, ‡ corresponding authors

We investigate here examples of complexity in composite materials. The objective of the paper is to show that clay particles can be aligned in different hosting media, such as: silicone oil, paraffin-wax, polystyrene and ambient air. The use of an electric field is an easily controllable, non-intrusive manner of inducing such an alignment. Depending on the medium used, a large span in time constants for the orientation and reorganization has been observed. Furthermore, the reorientation may be frozen into the material, thus permanently changing its properties.

Se investigan ejemplos de complejidad en materiales compuestos. El objetivo de este artículo es demostrar que se pueden alinear partículas de arcilla en diferentes medios como aceite de silicona, parafina-cera, poliestireno, y aire. El uso de un campo eléctrico resulta una vía fácilmente controlable y no-intrusiva de inducir el alineamiento. Se observa un amplio rango de constantes de tiempo para la orientación y la reorganización en dependencia del medio utilizado. Aún más, la reorientación puede congelarse en el material, de tal suerte que sus propiedades cambian permanentemente.

PACS: Granular materials rheology, 83.80.Fg; pattern formation in granular systems, 45.70.Qj; rocks magnetic and electrical properties, 91.25.F-; colloids, 82.70.Dd

INTRODUCTION

Application of an external electric field to a suspension of dielectric clay particles induces polarization of the particles. They will consequently re-orient and aggregate, and this results in the formation of a columnar structure parallel to the electric field direction. The clay particles polarize along their silica sheets, i.e. their stacking direction will be normal to the direction of polarization [1]. The mechanism of the polarization in clays is still under discussion, although one hypothesis is that the intercalated ions and water molecules, which are movable, could play a central role in particle electrical polarization. The resulting induced dipole is attached structurally to the clay particle, and this causes clay particles to reorient and interact, as suggested in [1]. However, recent measurements performed by us indicate that the contribution from the outer surface charges may be dominant, and the particle alignment is then determined by its shape, i.e. so that the longest axis of a single clay particle (or aggregate of particles) will be parallel to the direction of E-field lines [2].

The clay polarization is a rapid process ($< \mu s$) that is followed by a particle re-orientation with a rotation time proportional to the carrier fluid viscosity and inversely proportional to: firstly the difference in the dielectric constants between particle and medium; and secondly the electric field squared (see also [3]). The time scale for particle rotation is in the range of 10^{-3} to 10^1 s, for E-field between 50 and 2000 V/mm and viscosity of carrier fluid such as silicone oil between 100 and 500 $mPa \cdot s$ [2]. If the particle concentration is high enough, and a minimum critical E-field is applied, chain formation occurs via a particle dipole-dipole interaction [4].

The phenomena described above may be utilized in many different ways and just a few examples are: (i) Electro-rheological fluids (clay particles in silicone oil) in which the so-called liquid-to-solid reversible transition occurs via the application of an external E-field. Such a transition is manifested by changes of ER properties, namely: viscosity, yield stress, storage and loss moduli, etc. [5, 6, 7]. Some examples of application of ER fluids are: fast acting hydraulic valves or clutches [8]. (ii) Nanocomposites (clay particles in polymers), since the aspect ratio of the clay platelets and the interfacial contact area between the clay and matrix are high, the incorporation of small amounts of such inorganic filler into a polymer medium can significantly improve the properties of the resulting polymer/clay nanocomposites. Such nanocomposites can attain a high degree of stiffness and strength [9]. Furthermore, the presence of the dispersed phase results in additional properties, such as flame retardancy or enhanced barrier properties (e.g. gas permeability), when compared to either component [10, 11]. In many situations it is not only the *presence* of the well-dispersed filler but also its *orientational* ordering that may improve certain physical and

chemical properties. The electric-field-induced alignment of clay particles can thus be used to obtain and control a range of the desired material properties.

The above examples have clearly an application-oriented character. However, the focus of our studies is on better understanding of basic physics of such complex systems. Apart from already mentioned hosting media, we also here report for the first time structuring from clays in atmospheric air. The common denominator, for all studied systems, is the clay particle alignment in the presence of an *E*-field.

SAMPLES

Two types of clay particles, namely laponite (Lp) and fluorohectorite (Fh) are used in the present investigations. The synthetic Lp clay was purchased from Laponite Inc. and the synthetic Fh clay was purchased from Corning Inc. They both belong to the smectite family of clay minerals. Smectites are 2:1 phyllosilicates that possess a net negative charge on the surface of each crystalline layer. Counter ions are located between these lamellar sheets to balance for that charge. Exchangeable cations such as Na^+, Li^+, Ca^{2+}, Mg^{2+}, Cu^{2+} or Fe^{2+} are common. The chemical formulas are: $Na^+_{0.7}[(Mg_{5.5}Li_{0.3})Si_8O_{20}(OH)_4]^{0.7-}$ for Lp clay and $Na^+_{1.2}[(Mg_{4.8}Li_{1.2})F_4Si_8O_{20}]^{1.2-}$ for Fh clay, respectively. They are silicates where a fraction of Mg^{2+} ions is substituted by Li^+ in trioctahedral sites resulting in a negative structural charge [12]. Fluorohectorite has been reported from X-ray data to retain a stacked structure of lamellar particles composed of between 20 and 100 unit layers when dispersed in water, whereas laponite is known to exfoliate into single unit layers in aqueous suspensions [13]. The individual Lp clay particle resembles a disc of average diameter around 30 *nm*, whereas the size of Fh clay can be as large as several *μm*.
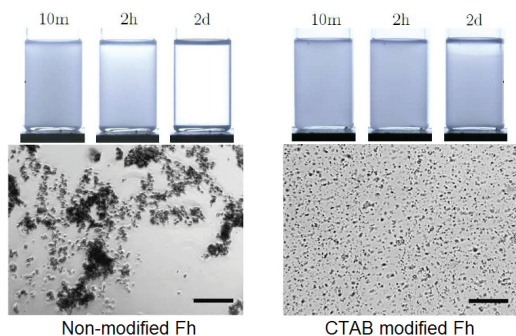
Figure 1: Microscope images of non-modified Fh (left) and organically modified CTAB-Fh (right) clay particles suspended in silicone oil. The length of the bar corresponds to 200 *μm*. The pictures of the glass vials with samples (top) illustrate the sedimentation dynamics. Adopted from [16].

Clays, in their natural forms, are hydrophilic, or depending on the context they may be referred to as organophobic. When suspended in a non-polar medium, such as silicone oil or polymeric matrix, they tend to form large agglomerates and

consequently sediment (see Figure 1). Addition of surfactants is commonly used to prevent particle agglomeration, which then slows down particle sedimentation, or if the particles are small enough (i.e. magnetic particles in ferrofluids), ensures that they are held in suspension by Brownian motions [14]. Another reason for modifying clays is the ease of uniform dispersion in an apolar polymer matrix. To promote compatibility between the inorganic filler and apolar polymers, it is necessary to chemically modify the inorganic clays by intercalation of organophilic cations, which expand the interlamellar space of the clay, decreasing the interaction among the silicate sheets, and facilitating the diffusion and accommodation of polymeric chains [15].
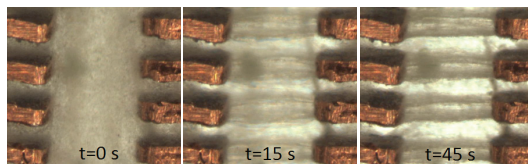
Figure 2: Optical microscopy images of clay/oil suspension without *E*-field applied (left) and a field of 1000 *V/mm* (middle and right).

RESULTS

Clays in silicone oil. The preparation of the ER fluid was undertaken by the following procedure. Na-Fh clay powder was crushed with a pestle and mortar, weighed and placed in an oven for 12 *h* at 110 *ºC*. The silicone oil was heated at the same conditions. Subsequently, the clay powder and silicone oil were mixed in glass tubes and sealed. The solutions were then vigorously hand-shaken for 2 *min* and placed in an ultrasonic bath for 1 *h*. Before each measurement the samples were hand-shaken again. The clay concentration was approximately 5 *wt*.%.

Firstly, optical observations were conducted. For that purpose the ER fluid was placed between two electrodes with pre-defined shapes as shown in Figure 2. The gap between the electrodes is roughly 1 *mm* and the electric field is applied horizontally.
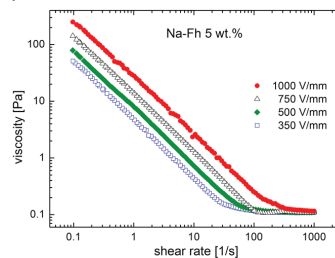
Figure 3: Flow curves for 5 *wt*.% clay particles suspended in silicone oil. Different electric field strengths are used, influencing the shear viscosity.

When no *E*-field is applied, the Fh particles are randomly dispersed into the silicone oil, as shown in Figure 2 (left). Microscopy images of the sample under a DC electric field of 1000 *V/mm* taken at different times, 15 *s* and 45 *s* are shown

1E38

in Figure 2 (middle and right). The formation of column-like structures aligning parallel to the field is clearly observed. Several thin chains are formed first, and these subsequently attract each other resulting in the creation of thicker columns. After a certain time (here several minutes) no major changes in the system are noticeable.
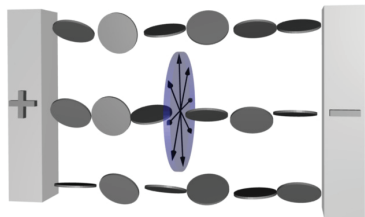
Figure 4: The sketch of the clay alignment in so-called anti-nematic configuration (see text for details).

Imagine now shearing the ER fluid perpendicular to the *E*-field direction. If the *E*-field is not present, the shear viscosity of such a sample (silicone oil and only 5 *wt*.% of clay) is close that of pure silicone oil. However, once the electric field is applied, so that the particles are oriented against the flow, the shear viscosity of a fluid containing clay particles is expected to increase. As the curves in Figure 3 show, this is also what is seen experimentally.

Clays in paraffin-wax. The particular type of paraffin-wax used here has its melting point around 65 °C and was chosen for two major reasons: (i) optimal melting and crystallization temperatures, providing both easy composite preparation and appropriate stiffness of the composite when in solid form at room temperature; (ii) a relatively non-polar and non-conductive material that can be used as an electrorheological carrier fluid when in the melted state. Fluorohectorite particles (~5 *wt*.%) were dispersed in the melted paraffin and then poured into a custom-made mould with two electrodes. The electric field strength of 500 *V/mm* was applied and kept for a few minutes until the paraffin crystallized and cooled down to room temperature. The solid composite was then investigated using wide-angle X-ray scattering.
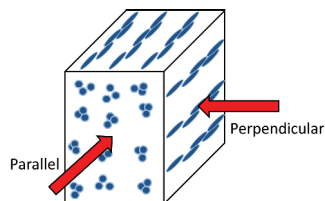
Figure 5: Simple sketch of what the X-ray beam probes in the sample.

When a 2-D X-ray pattern (like those shown in Figure 6) is integrated along the radial direction with a narrow *q*-range (2θ-angle) around the Bragg ring, one obtains a 1-D azimuthal plot which is then fitted using a parametric function. The fitting allows extracting parameters that are further used to calculate the nematic order parameter (S_2) (for details see [17]). This parameter ranges from -1/2 to 1, where 1 indicates perfectly

oriented particles in the nematic configuration, 0 means no orientational order, and finally -1/2 indicates perfectly oriented particles in the anti-nematic configuration [6, 17, 18]. It is expected that the clay particles align in the anti-nematic geometry and the validity of such assumption is tested below.

Several 2-D X-ray images were taken from the same sample at different polar angles, with the rotation axis parallel to the reference direction, which is here the direction of the *E*-field. The nematic order parameter was calculated for four sample positions and the results are presented in Table 1.

Table 1. Nematic order parameter as a function of the polar angle, with the rotation axis parallel to the direction of *E*-field lines.					
Sample rotation	0	30	60	90	Avg
Order parameter	-0.37 ±0.01	-0.35 ±0.01	-0.37 ±0.02	-0.36 ±0.01	-0.36 ±0.01

We observe that the nematic order parameters do not differ significantly from each other indicating that there is no preferential orientation along the polar angle. The arrowed disc shown in Figure 4 represents the plane perpendicular to the *E*-field direction, and that is in fact the average particle stacking direction. The black arrows indicate that clay normals are oriented without any preferred polar direction.
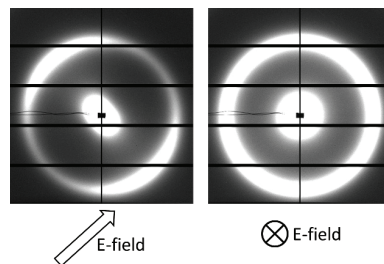
Figure 6: SAXS-patterns from PS/CTAB-Fh with permanently aligned clay chains. Remark: the sample is tilted 45 degrees in the *x-y* plane.

Clays in polystyrene. When aligning clay particles in liquid media the alignment may be lost after a while when the electric field is turned off. An approach to freeze the chain structure was tested by solidifying the matrix while the electric field was applied. The matrix, styrene monomer, polymerizes to give solid polystyrene polymer (PS). A 1 *wt*.% sample of organically modified CTAB-Fh (see [16] for details) was dispersed in styrene monomer and a small quantity of a radical initiator, benzoyl peroxide, was added. The clay/monomer suspension was filled in square shaped glass capillaries, which were sealed with a flame torch. The capillaries were then immersed in an 80 °C silicone oil bath, and placed between two plate electrodes. The electric field over the electrodes was set to 830 *V/mm*, and the samples were left to polymerize for 7 days. The resulting PS-clay composites were investigated with small angle X-ray scattering (SAXS) at the Dubble beam line at ESRF in Grenoble, France. The samples were probed with the X-ray beam perpendicular and parallel to the direction of clay chains

1E39

(see Figure 5). The main ring comes from the characteristic spacing between clay crystalline sheets, and $d_{001} \sim 4$ *nm*. A pronounced anisotropy of the d_{001} peak is seen in Figure 6 (left) due to clay alignment, i.e. on average, particles orient with their stacking direction perpendicular to the *E*-field lines. When probed along the chains the pattern looks isotropic, as shown in Figure 6 (right), since there is no preferential orientation of clay particles along the polar angle (see also [18, 19]).
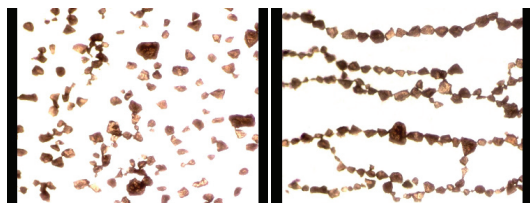
Figure 7: Laponite particle aggregates between two electrodes without *E*-field applied (left) and with an AC *E*-field of 500 V/*mm* (right). The images have been edited to enhance the contrast.

Clays in air. As the final example, we show laponite clay alignment in atmospheric air. Laponite clay powder stored in our laboratory at ~23 ºC and RH in range between 10 and 30 % was used. Such particles normally form aggregates and their sizes can span a few orders of magnitudes reaching a few *mm*. In the present work the size of the aggregates were between 10 and 100 *µm*. Figure 7 shows clay particle aggregates between two electrodes with no *E*-field applied (left) and with an AC *E*-field of 500 V/*mm* (right). The electrodes were kept horizontally and images were taken from above. Clay particles lied on a thin glass substrate, and when the electric field was applied the set-up was gently tapped, lowering the friction as the particles were momentarily suspended in air.

As can be seen, most of the clay particle aggregates align with their longest axis along the *E*-field direction. However, there are several particles disobeying that rule, and these making bridges between individual chains allowing for charge transport. It is possible that the dominant part of the clay polarization occurs only on the clay aggregate surface, not the bulk, i.e. in the clay galleries. However, it is difficult (if not impossible) to draw a firm conclusion on this point, since we deal here with large aggregates. Therefore our future work will be focused on reducing the complexity of the system by working with *single* clay particles, such as vermiculite.
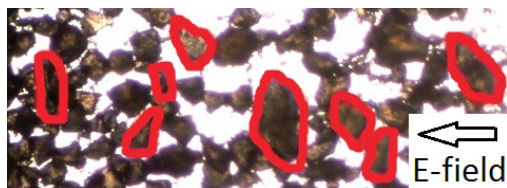
Figure 8: High concentration of laponite particle aggregates between two electrodes with an AC *E*-field of 500 V/*mm* applied. Several particle aggregates (red-color-marked) were not able to re-orient fully with their longest axis along the *E*-field lines due to jamming. This will effectively lower the value of the nematic order parameter.

In Figure 8 we also present structuring from particles in air, but this time the clay concentration is significantly higher. A possible jamming transition may occur where many particles have very little freedom to re-orient (see red-coloured particles). This is an ongoing study and more results are expected in the near future.

CONCLUSION

We have provided examples of recent results from our work on manipulation and orientation of asymmetric particles in external fields. Clay particles are ideal for this purpose due to their inherent large anisotropy and correspondingly high degree of polarizability. When placed in an apolar medium and subjected to an electric field, the particles will orient and organize within a time frame that depends principally on factors such as *E*-field strength and viscosity of the surrounding medium. We have shown how these effects may be induced in various media, with a large span in viscosity, from silicone oil, via polymer matrices to solidified wax, and even air. The clay particles may form chains that span the entire sample volume, thus changing the macroscopic properties of the material. Most notably, there will generally be a large change in the overall rheological behavior, and materials of this kind are therefore highly interesting for applications where the mechanical and structural properties should be manipulated via an electric field.

[1] J. O. Fossum, Y. Méheust, K. P. S. Parmar, K. D. Knudsen, K. J. Måløy and D. M. Fonseca, Europhys. Lett. **74**, 438 (2006).
[2] R. C. Castberg, Z. Rozynek, J. O. Fossum, K. J. Måløy and P. Dommersnes, work in progress
[3] R. C. Castberg, Z. Rozynek, J. O. Fossum, K. J. Måløy, P. Dommersnes and E. G. Flekkøy, Rev. Cub. Fis. **29**, 1E17 (2012).
[4] J. D. Jackson, *Classical Electrodynamics*, (Wiley 143, 1962).
[5] B. Wang, M. Zhou, Z. Rozynek and J. O. Fossum, J. Mater. Chem. **19**, 1816 (2009).
[6] Z. Rozynek, K. D. Knudsen, J. O. Fossum, Y. Méheust and B. Wang, J. Phys: Condens. Matter. **22**, 324104 (2010).
[7] Y. Méheust, K. Parmar, B. Schjelderupsen and J. O. Fossum, J. Rheol. **55**, 809 (2011).
[8] J. Madeja, Z. Kesy and A. Kesy, Smart Mater Struct. **20**, 105005 (2011).
[9] A. Esteves, A. Timmons and T. Trindade, Quim. Nova **27**, 798 (2004).
[10] S. S. Ray and M. Okamoto, Prog. Polym. Sci. **28**, 1539

(2003).

[11] S. Letaief and C. Detellier, J. Mater Chem. **17**, 1476 (2007).

[12] P. D. Kaviratna, T. J. Pinnavaia and P. Schroeder, J. Phys. Chem. Solids **57**, 1897 (1996).

[13] E. DiMasi, J. O. Fossum, T. Gog and C. Venkataraman, Phys. Rev. E **64**, 061704 (2001).

[14] Z. Rozynek, A. Jozefczak, K. D. Knudsen, A. Skumiel, T. Hornowski, J. O. Fossum, M. Timko, P. Kopecansky and M. Koneracka, Eur. Phys. J. E **34**, 28 (2011).

[15] K. S. Santos, S. A. Liberman, M. A. S. Oviedo and R. S.

Mauler, J. Polym. Sci. B: Polym. Phys. **46**, 2519 (2008).

[16] Z. Rozynek, B. X. Wang, J. O. Fossum and K. D. Knudsen, Eur. Phys. J. E **35**, 9 (2012).

[17] Y. Méheust, K. D. Knudsen and J. O. Fossum, J. Appl. Cryst. **39**, 661 (2006).

[18] I. Dozov, E. Paineau, P. Davidson, K. Antonova, C. Baravian, I. Bihannic and L. J. Michot, J. Phys. Chem. B **115**, 7751 (2011).

[19] Z. Rozynek, R. C. Castberg, A. Mikkelsen and J. O. Fossum, work in progress.

ARTICLE

Active structuring of colloidal armour on liquid drops

Paul Dommersnes[1,2,3,4,*], Zbigniew Rozynek[1,*], Alexander Mikkelsen[1], Rene Castberg[2], Knut Kjerstad[1], Kjetil Hersvik[1] & Jon Otto Fossum[1,4,*]

Adsorption and assembly of colloidal particles at the surface of liquid droplets are at the base of particle-stabilized emulsions and templating. Here we report that electrohydrodynamic and electro-rheological effects in leaky-dielectric liquid drops can be used to structure and dynamically control colloidal particle assemblies at drop surfaces, including electric-field-assisted convective assembly of jammed colloidal 'ribbons', electro-rheological colloidal chains confined to a two-dimensional surface and spinning colloidal domains on that surface. In addition, we demonstrate the size control of 'pupil'-like openings in colloidal shells. We anticipate that electric field manipulation of colloids in leaky dielectrics can lead to new routes of colloidosome assembly and design for 'smart armoured' droplets.

---

[1] Department of Physics, Norwegian University of Science and Technology, Hoegskoleringen 5, N-7491 Trondheim, Norway. [2] Department of Physics, University of Oslo, PO Box 1048, Blindern, N-0316 Oslo, Norway. [3] Laboratoire Matière et Systèmes Complexes, Université Paris 7 Diderot, 10, rue Alice Domon et Léonie Duquet, F-75205 Paris, France. [4] Centre for Advanced Study, Norwegian Academy of Science and Letters, Drammensvegen 78, N-0271 Oslo, Norway. * These authors contributed equally to this work. Correspondence and requests for materials should be addressed to J.O.F. (email: jon.fossum@ntnu.no).

Colloidal particles can bind strongly to fluid interfaces and assemble into thin layers. Monodisperse colloidal beads can form two-dimensional (2D) ordered colloidal crystal monolayers[1–3], and poly-disperse and anisotropic particles form amorphous shells[4–6]. This effect is currently much studied in relation to particle-stabilized 'Pickering' emulsions[7–9] where particle coatings on droplets effectively prevent droplet coalescence and produce very stable surfactant-free emulsions. Emulsions are ideal templates for producing particles and capsules[10]. Solid colloidal capsules, colloidosomes, can be produced by fusing or linking colloidal particles at the surface of Pickering emulsions droplets[11].

Particle-stabilized emulsions and their use as templates for making colloidal structures have a vast range of applications, notably in food processing[12], biomedicine[13,14] and petroleum industry[15]. It is increasingly realized that the colloidal-coated particles can have a role that goes beyond mere encapsulation: colloidal particle surface properties and volume can respond to temperature and solvent changes, colloidal particles can also be manipulated by external fields and act as catalyst to chemical reactions. This opens up for new possibilities for the use and control of emulsions and colloidal capsules: controlled release, with possible applications to drug delivery, has been achieved from pH-responsive colloidal capsules[16], and pH-responsive particles have been shown to act as reversible on/off emulsifiers for Pickering emulsions[17]. Emulsions stabilized by paramagnetic colloidal beads have been shown to undergo controlled phase separation in response to magnetic fields[18]. Solid particles can also stabilize water–oil emulsions and simultaneously catalyse biomass refining reactions at the liquid interfaces[19].

Droplet-based templating[10] include, for example, production of colloidosome capsules[11] or new porous structures[20]. Controlled production of anisotropic colloidosomes, either in shape or surface material composition, will likely have an important role in the development of colloidosome materials technology. Non-spherical droplets have been produced from double-emulsion templates or by 'arrested' droplet coalescence[21,22], and Janus colloidal shells, composed of two different colloidal hemispheres, can be produced by targeted delivery of colloidal particles in a microfluidics setup[23].

Although electric fields are commonly used for emulsion breaking, there appears to be few studies of Pickering droplets subjected to electric fields. It has been shown that particles adsorbed on droplets can be manipulated by AC electric fields by dielectrophoresis (DEP) effects[24–26], and electric fields can also be used to remove particles from droplet surfaces due to droplet breakup and tip streaming[27].

Here, we wish to bring to attention the possibilities offered by electric fields for assembly and manipulation of colloidal armour on liquid droplets. We demonstrate a new route of colloidal surface self-assembly in a simple setup including electrohydrodynamic (EHD) circulation flows in leaky-dielectric drops. Oil-in-oil emulsion droplets in electric fields have been extensively studied, and constitute a classic example of electric field-induced hydrodynamic flow, as described by the Taylor–Melcher leaky-dielectrics model[28,29]. Here, we show that colloidal particles are carried by EHD convective flow, concentrating the particles in a dense packed colloidal ribbon on the drop surface. This is reminiscent of the 'coffee-ring' effect, which is owing to colloidal particles carried by capillary convective flow in an evaporating droplet[30]. In addition, we show that colloidal ribbons, once assembled, can be dynamically modulated by tuning the electric field strength, provided the colloidal particles are polarizable and can form dipolar chain structures on the drop surface. To our knowledge, this is the first realization of a Winslow electro-rheological type system[31,32] confined to a 2D surface.

Results

Colloidal clay ribbons. A millimeter-sized clay-silicone (1 wt% clay) drop is immersed in castor oil, see Fig. 1. The clay is dispersed throughout the drop. The top row of images is taken

| a | b | c | d |
| No E-field $t=0$ min | 150 Vmm⁻¹ $t=1$ min | 150 Vmm⁻¹ $t=2$ min | 150 Vmm⁻¹ $t=4$ min |
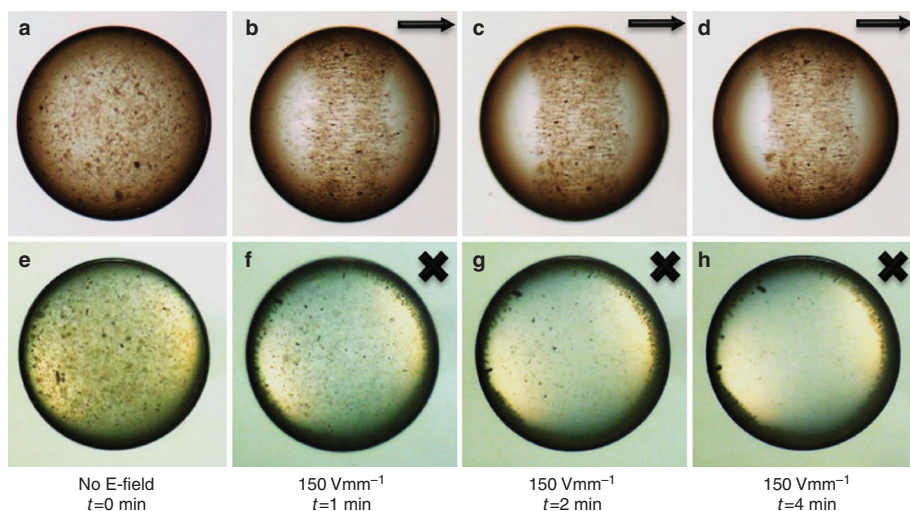
Figure 1 | Assembly of colloidal clay surface ribbon. A silicone oil drop of radius 0.7 mm with Fh clay particles initially dispersed throughout the drop. The drop is immersed in castor oil. The arrows and crosses indicate the direction of the E-field. The four upper panels (**a–d**) are viewed perpendicular to the E-field direction, while the four lower panels (**e–h**) are viewed along the E-field direction. (**a,e**) Show the situation before the electric field is turned on, and (**b–d**) and (**f–h**) after a DC electric field is applied. Hydrodynamic circulation flows are observed in the drop, and in a few minutes clay particles are concentrated in a ribbon-shaped film on the drop surface.

perpendicular to the applied electric field, whereas the bottom row is in the direction of the field (as seen through transparent electrodes). A DC electric field of strength 150 Vmm^{-1} is applied across the cell. Circulation flows can be seen inside the drop immediately after application of the electric field. A ribbon-shaped film builds up at the drop surface in less than a minute, and in about 4 min the drop becomes transparent in the direction of the field, indicating that clay particles have migrated to the surface ribbon. After the initial assembly dynamics, a steady state exists with a stable ribbon. The film is disordered, containing small aggregates of clay particles. The boundary of the ribbon is sharp, suggesting that the clay particles are closely packed or cohesive. Once adsorbed, the clay particles seem to be bound irreversibly to the interface: turning off the electric field only results in slow disruption of the ribbon, but the clay particles still remain on the surface of the drop. At slightly higher field strengths, the steady-state ribbon clearly contains dipolar electro-rheological chain structures, see Fig. 2.

The formation of the ribbon must involve two processes: (1) transport of clay particles from the drop bulk to the drop interface and (2) assembly of the ribbon film on the drop interface. It is well documented that colloidal particles adhere strongly to oil–water interfaces. For example, clay particles are known to absorb strongly at oil/water interfaces and produce stable emulsions[9]. This is generally attributed to capillary binding: a particle at the interface is trapped in a capillary barrier with a substantial energy cost of moving to either side of the liquid interface[7]. The typical surface tension between water and many oils is $\gamma_{o-w} \approx 30 - 40$ mNm^{-1}, and the resulting binding energy of micron-sized particles at oil–water interfaces is very high compared with thermal energies,[7] $\Delta E \sim 10^3 k_B T$. The surface tension between castor oil and silicone oil is[33] $\gamma_{o-o} \approx 4.5$ mNm^{-1}, an order of magnitude lower than oil–water tension, but the capillary binding energy is still likely to be very high compared with thermal energies, explaining the strong affinity of clay to the castor/silicone oil interface.

The width of the ribbon depends on the initial clay concentration in the drop: for an electric field of 200 Vmm^{-1} and clay concentration 1.5 wt% the ribbon almost covers the drop, while for 0.5 wt% the ribbon is narrow (see the Supporting Information). Assuming that the majority of clay particles have migrated into the ribbon, we may estimate the average thickness of the clay ribbon: The density ratio of clay and oil is $\sim$1.5–2, and 1.5 wt% is equivalent to $\sim$1% by volume of clay. In the case where the clay completely covers the drop surface, the thickness of the film is $d = cr/3$, where c is the initial volume percentage of clay inside the drop and r the drop radius. For a mm-sized drop with 1.5 wt%, this would give a shell thickness of $d \sim 3 \mu$m, which
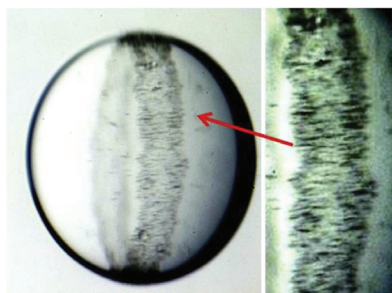
is in the same size range as the fluorohectorite (Fh) clay particles used here, suggesting that the film is composed of just a few layers of clay particles.

The timescale for a clay particle of size $b \sim \mu$m to diffuse 1 mm in 100 cSt silicone oil is roughly $t \sim 10^3$ days, and therefore hydrodynamic flow, sedimentation or electric forces are required to transport clay particles to the drop surface at the timescales reported above.

In an emulsion formed by two leaky-dielectric liquids, such as two oils, free charge accumulation can result in a Maxwell electric stress that sets up liquid circulation flows inside and outside the drops[28,29]. When the drop is less conducting than the surrounding liquid (such as silicone drop in castor oil), the circulation flow is directed towards the drop equator, as shown in Fig. 3a. We have observed the flow, both outside and inside the drop. Tracing paths were made by following one polyethylene (PE) particle inside and a few beads outside the drop, see Fig. 3b. If the drop is more conductive than the surrounding liquid, then the flow is reversed, and also significantly weaker. For a silicone drop in castor oil, the Taylor model[28] predicts that the induced velocity at the surface is $v_\theta \sim \frac{r\varepsilon\varepsilon_0 E^2}{\eta} \frac{\tilde{\varepsilon}}{\varepsilon}$ and directed to the drop equator (see Methods). The timescale to convect a particle towards the equator is $\sim \frac{r}{v_\theta}$, which in a field of 150 Vmm^{-1} gives a timescale of $t \sim 7$ s (see Methods). This shows that Taylor flow is sufficiently strong to induce the ribbon formation during the measured timescale. The process is likely slowed down by the presence of clay particles, as they modify both the electric field around the drop and the EHD flow. The increased conductivity of the drop owing the clay film will reduce the free charge buildup and therefore also reduce the induced hydrodynamic flow.

It has previously been observed that large colloidal particles adsorbed at droplet interfaces can migrate to the 'equator' or the 'poles' of the droplet when subject to an AC field[24,26] owing to DEP of particles on the droplet surface: polarizable colloidal particles are subject to forces in non-uniform fields at the droplet surface, the force being proportional to the gradient of the square of the field strength. This effect should also contribute in our case, as clay is polarizable, and should therefore be attracted towards stronger electric fields at the droplet equator. We have previously shown that suspended clay particles are significantly more conductive than oil[34], and therefore can be considered as conductors when subject to a DC field. The force on a spherical
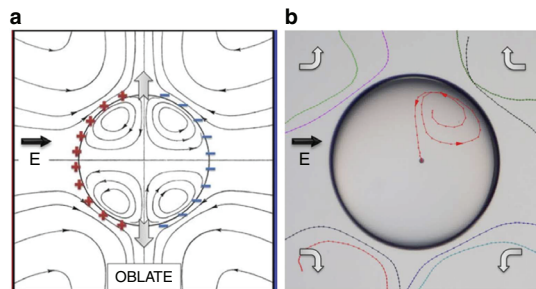
Figure 3 | Hydrodynamic streamlines in Taylors electrohydrodynamic drop model. The model is valid for a silicone drop in castor oil (**a**). Adopted from ref. 28. This flow, both outside and inside the drop, is observed experimentally (**b**). Tracing paths are made by following PE beads outside and one particle inside a drop of radius about 1mm. Arrows indicate the direction of the flow. The E-field direction is horizontal in the plane of the panels, as indicated by the arrow. For the side view of the internal particle trace (in the direction of the electric field), see Supplementary Fig. S1.

Figure 2 | Perspective view displaying the surface clay ribbon film on a drop. Drop radius is 1mm. 2D dipolar chain formation of clay particles can be seen in the ribbon. Electric field strength is 200 Vmm^{-1}.

particle of radius b in an inhomogeneous DC electric field is $F_{DEP} = 2\pi\varepsilon\varepsilon_0 b^3 \frac{\sigma_p - \sigma_m}{\sigma_p + 2\sigma_m} \nabla E^2$, where $\varepsilon\varepsilon_0$ is the dielectric constant of the fluid medium, σ_p and σ_m are the conductivities of the colloidal particle and the fluid medium, respectively[35]. This expression for F_{DEP} is valid provided that the size of the polarized particle is small compared with the length scale of the non-uniformity of the electric field. This is justified in the present case because the inhomogeneity of the electric field is given by the drop size, which is of the order of 1 mm, and the size of the clay colloidal particle is in the range of 1–10 μm. As in the present case $\sigma_p \gg \sigma_m$ and $\nabla E^2 \sim \frac{E^2}{r}$, then $F_{DEP} \sim \varepsilon\varepsilon_0 b^3 E \frac{E}{r}$. Balancing the hydrodynamic drag $\sim \eta b$ and the dielectrophoretic force thus gives a dielectrophoretic velocity of the order $v_{DEP} \sim \frac{F_{DEP}}{\eta b}$. The ratio of the EHD and dielectrophoretic velocities is $\frac{v_{DEP}}{v_0} \sim \frac{\varepsilon}{\bar{\varepsilon}} \frac{b^2}{r^2} \ll 1$, meaning that dielectrophoretic effects are not significant here. This we have verified experimentally by using non-polarizable particles, for which we observed ribbon formation on similar timescales as for clay, see Supplementary Fig. S1.

The Maxwell–Wagner charge relaxation time for the silicone in castor oil system is $\tau_{MW} \approx 1$ s. Taylor EHD flow will therefore be suppressed at AC frequencies much larger than 1 Hz (ref. 29). This is consistent with our observation that for clay–oil drops in AC fields, we only obtain ribbon formation at very low frequencies (0.1 Hz), and the ring gradually becomes wider as the frequency is increased.

Although EHD flow accounts for the stability of the ribbon once formed, it does not directly explain the migration of clay to the interface. It is not evident that the flow can direct particles from the bulk to the surface, as the flow component normal to the surface vanishes. Thus, particles carried by Taylor–Melcher circulation streamlines will approach the drop surface, but they eventually turn before adsorbing. In (refs 23,36) it was observed that efficient colloidal assembly on droplets by hydrodynamic flow requires finite Reynolds number flow, that is, inertial effects. As clay forms dipolar chains on the drop surface, see Fig. 2, there must be significant electric field-induced short-range dipole interactions between the particles, suggesting that clay near the drop surface could simply be attracted to the clay that is already trapped. Another contributing mechanism could be charge uptake on clay particles, which could drive them in the electric field to directly hit the surface and adsorb. For drops only subjected to high-frequency AC field, we do not observe migration of clay particles towards the drop surface, the particles rather appear to form chains inside the drop. In this case, the dipole interactions alone are not sufficient to direct clay to the surface, suggesting that DC-induced EHD convection and clay particle dipole interactions work together to enhance the rate of clay adsorption to the drop interface.

The clay film can be considered as a 2D electro-rheological fluid with dipolar chain formation, see Fig. 2. The tangential component of electric surface field in particle-free oil drops is $E_t = 3\sigma/(\bar{\sigma} + 2\sigma)E \sin(\theta)$. The conductivity of castor oil is much higher than silicone oil, hence the field at the equator ($\theta = \frac{\pi}{2}$) is $E_t \approx \frac{3}{2}E$. In 3D bulk suspension, we have previously observed clay chain formation above $E \sim 350$ Vmm^{-1} (refs 32,34); if we assume similar dynamics in 2D, one expect to see chain formation at droplet surface for applied field of roughly $E \sim 230$ Vmm^{-1}, in fair agreement with the observations.

At field strengths below 250 Vmm^{-1}, we observe axisymmetric clay ribbon formation, either thin or thick ribbons, depending on the initial clay concentration. However, at increased field strengths the drop response depends on clay concentration.

At lower clay concentration (0.5 wt%), increasing the field strength induces an instability of the ribbon, it breaks up into several counter-rotating colloidal assemblies (shown in Fig. 4 and
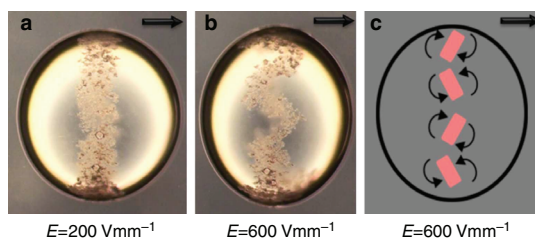

Figure 4 | Breakup of clay ribbon into rotating domains. Clay concentration is 0.5 wt%. The ribbon is stable at field strength of 200 Vmm^{-1} (**a**). At 600 Vmm^{-1} (**b**), the ribbon breaks up into several domains with continuous rotation (vortices) as illustrated in the cartoon (**c**). The drop remains oblate even at high fields, similar to a pure silicone drop in castor oil that experience EHD flow deformation (see also Supplementary Movie 1). The drop radius is about 1 mm. The E-field direction is horizontal in the plane of the panels, as indicated by the arrows.

Supplementary Movie 1). Particles that are less conducting than their surrounding liquid can spin in DC electric fields, known as Quincke rotation[37]. In the present case, clay is more conducting than the surrounding liquid, and we therefore exclude Quincke rotation as the mechanism here. However, our observations are in line with previous work showing that conducting particles in bulk can assemble and form counter-rotating vortices[38].

At higher clay concentrations, the ribbon width increases when the electric field is increased, as shown in Fig. 5. This is opposite to what can be expected within the Taylor–Melcher model for a particle-free pure oil drop where the EHD flow increases with field strength, which should result in increased compression of the ring and not stretching. We have previously observed that Fh chain formation in silicone oil gives non-ohmic response and strongly enhanced conductivity[34], and in the present case, this should diminish the charge buildup on the drop, and thereby suppress the EHD flow. A similar effect is seen in the drop deformation: At high fields and high clay concentrations, the drop deformation can change from oblate to prolate as shown in Fig. 5, indicating that the EHD Taylor flow is suppressed or reversed[28].

Clay pupil. The above observations suggest that such colloidal films can be actively controlled by electric fields. As a simple illustration of this, we have performed experiments in which we switch between two different field strengths, one that induces a narrow ribbon formation, and a higher field that actively stretches the ribbon and covers the drop, see Fig. 6. Seen through the electrodes, this has the appearance of an expanding and contracting 'pupil'. The fact that the film rapidly covers the surface at higher field strength cannot be attributed to clay wetting dynamics at the interface (Marangoni), as turning the field off does not lead to rapid coating. There must therefore be an electrically induced force that actively stretches the film armour. The clay itself will modify the electric field, as clay is more conductive than both oils. Thus, there will be free charge accumulation at the edge of the ribbon, and the electric field acting on these charges could induce electro-stretching of the film. A drop fully covered with dense colloidal armour of conducting colloidal particles can be considered as a Faraday cage screening the internal electric field[23], and hence removing the necessary conditions for Taylor–Melcher flow.

A complete understanding should take into account the electrohydrodynamic response of the combined colloidal clay–
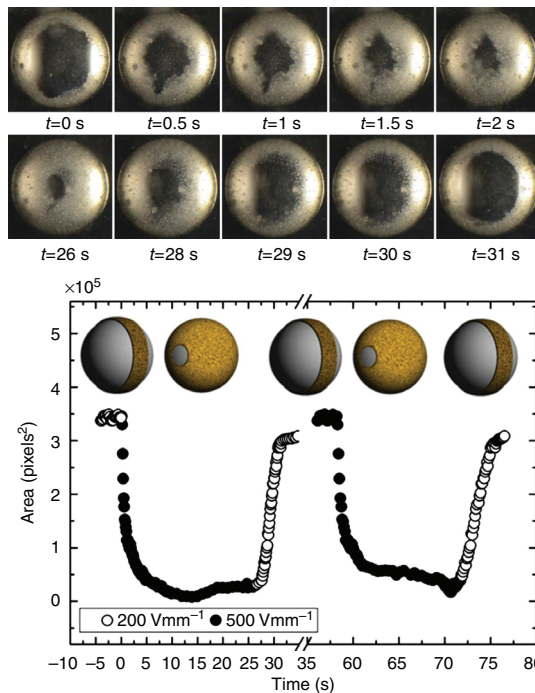
ARTICLE
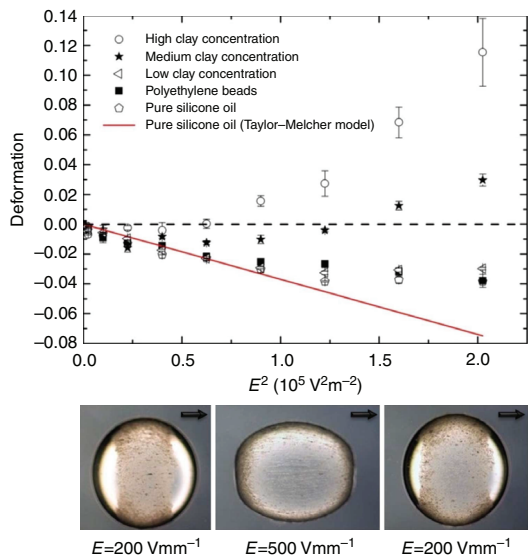
Figure 5 | Drop deformation as a function of the square of the electric field strength. Pure silicone drops are oblate (drop deformation $D < 0$) and the measurements for weak deformations ($-0.04 < D < 0$) quite accurately follow the prediction of Taylor–Melcher perturbation theory. Drops with low clay concentration almost follow the same curve as drops without clay. However, with higher clay concentrations the behaviour is qualitatively different: at low field strengths the drop is oblate, but as the field strength increases the drop deformation reverses from oblate to prolate ($D > 0$). This behaviour coincides with the nonlinear electric response of clay particles, at high field strengths clay form increasingly longer conductive dipolar chains that effectively can short-circuit the silicone drop. The three images at the bottom show how a drop with clay concentration in the medium to high regime (that is, 1–1.5 wt%) deforms reversibly as the electric field strength is increased and decreased. The drop radius is about 1 mm. The E-field direction is horizontal in the plane of the panels, as indicated by the arrows.

Figure 6 | Actively contracting and expanding pupil armour. This is shown in the series of ten images on the top. The drop is viewed along the E-field direction, as indicated by the crosses. At 200 Vmm^{-1}, the drop (of a radius about 1 mm) is partially covered by a clay ribbon, and at 500 Vmm^{-1} the drop is nearly fully covered. The timescale of switching is seconds (see also Supplementary Movie 3). This is a reversible process as displayed in the bottom panel, where we plot the area of the pupil opening versus time (following changes of the electric field strength). The cartoons in the inset display a perspective view of the process.

oil systems, including the non-ohmic conductivity of the clay film. For example, for pure particle-free drops the type of axisymmetric deformation is not field dependent, and is either always prolate or oblate depending on the relative dielectric constant and conductivity of the two liquids[29]. A pure silicone oil drop in castor oil is oblate; however, with clay particles present, we observe that the drops can switch to prolate deformation as the field strength is increased, as illustrated in Fig. 5. This is consistent with the clay film having a non-ohmic response. In pure drops, it is the Maxwell–Wagner times that decide whether a drop is oblate or prolate, whereas with clay the charge accumulation is dependent on field strength, making it possible to switch from oblate to prolate as the conductivity increases.

For higher clay concentrations (above about 2 wt%), the drop surface seems to be covered by a clay armour, and asymmetric drop stretching occurs. We observe breakup at field strength of 400 Vmm^{-1} and above, in contrast to pure silicone oil drops that are only weakly deformed at such field strengths.

To investigate the robustness of the clay pupil effect, we performed equivalent experiments on several different types of clay (Supplementary Table S1). It was found that four clay samples exhibited the pupil effect. The presence of pupil effect correlates with high clay conductivity, supporting the hypothesis

that the pupil closing is related to conductive dipolar clay chains short-circuiting the drop.

Insulating colloidal beads. Clay particles are more conductive than silicone oil. We therefore also investigated electrically insulating beads, with dielectric constant similar to that of silicone oil, and thus practically unpolarizable in the present experiments (for example, polystyrene or PE). Therefore, there should be no noticeable dipole interactions between the insulating beads in our case, and also the conductivity of the drop should not be enhanced. Nevertheless, we observe insulating colloidal ribbon formation, on a similar timescale as for clay particles (Supplementary Fig. S2). However, in most of the experiments with insulating beads, many beads continue to move around inside the drop, and only after applying the DC field for significantly longer times all the beads will go to the surface. This supports the idea that electric forces or sedimentation aid the clay particle to absorb on the drop interface, as discussed above. As for the clay particles, at higher fields we observe breakup of the colloidal ribbon into several small rotating domains (Supplementary Fig. S3 and Supplementary Movie 2), similar to the dynamics observed in clay ribbons at lower concentration, see Fig. 4. Both for the polystyrene and PE beads, we observe that the domain rotation frequency at 300 Vmm^{-1} is of order of

magnitude 0.1 Hz and increases with electric field with a rate of $\sim 4 \times 10^{-4}\,mmV^{-1}s^{-1}$ (within the range of 275–375 Vmm^{-1}). In the range 200–270 Vmm^{-1} there is ribbon deformation and the domains are not clearly defined. At even lower fields, that is, below 200 Vmm^{-1}, the ribbon is static. The rotation frequency does not appear to follow the E^2 behaviour of the Taylor–Melcher model, suggesting that this may be a different kind of flow instability. With insulating particles, we always observe oblate drop deformation, suggesting that it is the conductive properties of clay that induces prolate deformations.

We have also performed additional experiments with 20 × smaller polystyrene beads and we observed that the time it takes for beads to adsorb onto the drop surface is noticeably longer than for larger beads. We attribute this to the role of sedimentation in aiding the Taylor–Melchor flow in the process of bringing particles onto drop surfaces.

Conducting colloidal beads. To emulate the conductive properties of clay on drop surfaces, we also performed experiments with conductive silver-coated beads inside silicone drops immersed in castor oil. The beads are rapidly transported to the drop surface where they form chains; see Fig. 7, similar to the clay particle case shown in Supplementary Fig. S4. We also observe a very similar transition from oblate to prolate deformation. With sufficient number of beads to form long chains spanning the drop, the drop takes a prolate deformation, see Fig. 7a. This indicates that the increased conductivity suppress Taylor–Melcher flow associated with oblate deformation. With fewer beads, the drop is oblate, see Fig. 7b.

We have also investigated the role of the sedimentation in the process of bringing colloidal particles to the drop surface by conducting experiments with heavy silver-coated glass particles

and we see that the sedimentation is significantly faster than that of lighter polymer beads investigated above. It can be seen that even in the case that almost all conductive particles sediment to the bottom of the drop, they self-organize themselves into chain structures spanning the entire drop surface, as shown in Supplementary Movie 4.

Discussion

We have shown that electric fields can induce structural assembly of colloidal armour on oil drops, including 'equatorial' ribbons and 'longitudinal' dipolar chains. Electrohydrodynamic circulation flows inside the drop and dipole interaction between particles can account for the observations. The armour width can be actively controlled by the strength of the electric field and we have shown that this effect is intimately linked to the magnitude of polarizability contrast between particles and the drop oil and colloidal particle conductivity (Supplementary Table S1). Thus in the present experiments, the 'pupil effect' can only be observed with the clay particles, as our insulating beads only form equatorial ribbons, and metallic-coated particles only form chain-like structures. This is illustrated in Fig. 8, where we observe a drop covered simultaneously with insulating beads and metallic-coated glass beads. It would be interesting to extend this study to mixtures of different particles, which could lead to more advanced electrically controlled self-assembled surface structures. Solidification of these structures can be induced by UV light or heating to produce anisotropic functional colloidosomes[11]. The method we have demonstrated here is easily transportable to microfluidic devices that include use of electric fields[39]. Soft matter is characterized by being easily deformable by external fields or forces. The observed electro-stretching of the clay armour on drops is an example of 2D soft matter. To our knowledge, this is the first realization of a Winslow electro-rheological type system[31,32] confined to a 2D surface. In 3D space, it is well established that electro-rheological chains often attract and form large bundles[40]. In our case, we did not observe bundling on drop surfaces, rather the chains repel each other, and are regularly spaced in a stable configuration.

It should be possible to design other 'soft capsules' that respond to external fields. We believe that the results presented here can lead to new methods for assembly of colloidal particles on drops leading to advanced emulsion and template-based design. It is possible to mass produce various colloidal shells (ribbons, pupils, and so on) and this is shown in Supplementary Fig. S5, where ribbons of Fh clay particles are viewed at an angle $\sim 60°$ with
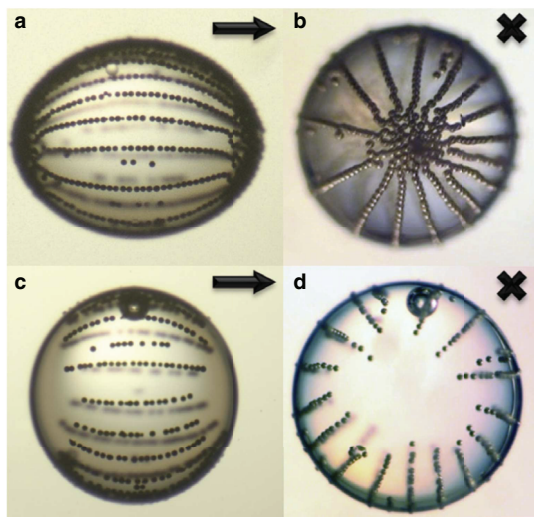
Figure 7 | Drop behind bars. (**a,b**) Conducting beads on the surface of a silicone drop with a radius of about 1 mm embedded in castor oil: the beads attract and form chains, resulting in a colloidal bar armour. The drop now has a prolate shape, owing to the increase in electric conductive from the chains, which short-circuit the drop and supress the free surface charges inducing the Taylor–Melcher EHD flow. (**c,d**) At lower bead concentration, the chains do not span the entire drop, and the drop is oblate, indicating presence of Taylor–Melcher EHD flow. The arrows and crosses indicate the direction of the E-field.
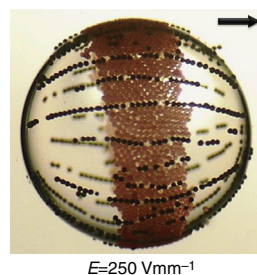
$E = 250$ Vmm^{-1}

Figure 8 | Silicone oil drop covered simultaneously with PE beads and metallic-coated glass beads. The applied electric field strength is 250 Vmm^{-1}. The E-field direction is horizontal in the plane of the panels, as indicated by the arrow. The PE beads only form equatorial ribbons, and the metallic-coated particles only form chain-like structures. The dynamic 'pupil effect' observed for clay particles (see Fig. 6) cannot be realized for any of these cases in the present experiments. The drop radius is about 1 mm.

respect to the direction of electric field (a); whereas the opening and closing of pupils for multiple droplets are shown in (b) and (c), respectively. At very high droplet numbers, the mass production is hampered by droplet coalescence.

Methods

Sample cell. The experiments are performed in a square glass cuvette ($10 \times 10 \times 30 \, mm^3$), in which two sides are made of transparent ITO (indium tin oxide) electrodes, allowing observation of drops both parallel and perpendicular to the applied electric field. In all images, the direction of gravity is downward.

Oils. The cell is filled with castor oil (Sigma-Aldrich 83912, specific density of $0.961 \, gcm^{-3}$ at 25 °C, electric conductivity 45 pSm^{-1}, relative permittivity 4.7 and viscosity 1000 cSt). Silicone drops (Down Corning 200/100 cSt, Prod 630074A, specific density of $0.97 \, gcm^{-3}$, electric conductivity ~3–5 pSm^{-1}, relative permittivity 2.1) containing colloidal particles are put into the castor oil using a pipette.

Clay minerals. Fh (fluorohectorite with different exchangeable cations, that is, Na, Li, Fe and Cu in the present case) and Laponite are synthetic 2:1 clay minerals. The Fh clay minerals used here comes from the same batch of materials as reported by characterized by Hansen et al.[41] and references therein. Na-MMT (sodium-montmorillonite) and Vermiculite are commercially available natural 2:1 clay minerals. Kaolinite and Halloysite are commercially available natural 1:1 clay minerals. Quick clay is a mixture of geologically available natural clays.

Other colloidal particles. Silicone drops with colloidal beads are also studied: Fluorescent PE beads (UVPMS- BY2 45–53 µm) and conductive silver-coated glass beads (SLGMS- AG 45–53 µm) were purchased from Cospheric LLC; polystyrene beads (Dynoseeds CS40 and CS2) of diameter 40 and 2 µm were purchased from Microbeads.

Preparation of colloidal dispersions. Silicone oil and clay powders are measured by weight and stirred together followed by ultrasonic bath to avoid aggregation of clay particles.

Timescale for colloidal ribbon formation. The characteristic timescale for the EHD surface convection of particls can be estimated from the Taylor–Melcher model: the surrounding liquid (castor oil) has electric conductivity σ, dielectric constant ε and viscosity, and for the drop (silicone oil) the corresponding values are $\tilde{\sigma}$, $\tilde{\varepsilon}$ and $\tilde{\eta}$. The flow velocity is conveniently expressed in terms of the ratios[28]:

$$R = \frac{\sigma}{\tilde{\sigma}} \qquad S = \frac{\tilde{\varepsilon}}{\epsilon} \qquad \lambda = \frac{\tilde{\eta}}{\eta} \qquad (1)$$

In this notation, the EHD flow velocity at the drop boundary is[28]:

$$v_\theta = \frac{9}{10} \frac{r\varepsilon\varepsilon_0 E^2}{\eta} \frac{R(RS-1)}{(2R+1)^2} \frac{1}{1+\lambda} \sin(2\theta) \qquad (2)$$

where r is the drop radius, θ the polar angle and E the electric field strength. Neglecting any drag on the particle, that is, assuming it follows the flow, the time required to convect a surface-adsorbed particle to the ring is $t \sim r/v_\theta$. For castor oil and silicone oil, the timescale is: $t \sim 1.7 \times 10^5 s \times (Vmm^{-1}/E)^2$

For a field strength of $E = 100 \, Vmm^{-1}$, the corresponding timescale is $t \sim 17 s$, which compares well with the experiments on PE particles, whereas in a field $E = 200 \, Vmm^{-1}$, the timescale is $t \sim 4 s$ (see also Supplementary Fig. S6 and Supplementary Fig. S7). These values are approximate and valid in the dilute limit. For higher colloidal concentration and as the ribbon becomes wider (see Supplementary Fig. S8), the EHD flow is reduced.

AC electric fields. According to the Taylor model, EHD flow in a drop is generated by surface eletrostatic stress due to buildup of free charges at the drop surface. If the AC field has a period much shorter than the Maxwell–Wagner relaxation time, there will essentially be no buildup of free charges. The Maxwell–Wagner charge relaxation time of a drop (sphere) is $\tau_{MW} = \frac{2\epsilon + \tilde{\epsilon}}{2\sigma + \tilde{\sigma}} \epsilon_0$, where ϵ and σ are the dielectric constant and electric conductivity of the surrounding liquid (castor oil) and $\tilde{\epsilon}$ and $\tilde{\sigma}$ that of the drop, taking the known values for castor and silicone oil gives $\tau_{MW} \approx 1 s$. The presence of particles will of course modify the effective conductivity and dielectric constant, but roughly the EHD flow should be absent for AC frequencies much larger than 1 Hz, and for frequencies much lower than 1 Hz one expects EHD flow with the same direction as in a DC field (the EHD is independent of the direction of the electric field), but oscillating between zero flow and a maximum flow rate at the peak of the AC field. In Supplementary Fig. S9, we show experiments of the same drop, first in 50 Hz, 1 Hz, then 0.1 Hz and field amplitude of $100 \, Vmm^{-1}$. Ring formation is only seen in the 0.1 Hz, supporting the hypothesis that ring formation is driven by EHD flow.

References

1. Pieranski, P. Two-dimensional Interfacial colloidal crystals. *Phys. Rev. Lett.* **45,** 569–572 (1980).
2. Nikolaides, M. G. *et al.* Electric-field-induced capillary attraction between like-charged particles at liquid interfaces. *Nature* **420,** 299–301 (2002).
3. Leunissen, M. E., van Blaaderen, A., Hollingsworth, A. D., Sullivan, M. T. & Chaikin, P. M. Electrostatics at the oil–water interface, stability, and order in emulsions and colloids. *Proc. Natl Acad. Sci. USA* **104,** 2585–2590 (2007).
4. Yan, N. X. & Masliyah, J. H. Adsorption and desorption of clay particles at the oil-water interface. *J. Colloid Interface Sci.* **168,** 386–392 (1994).
5. Yue, N., Xue, M. & Qiu, S. Fabrication of hollow zeolite spheres using oil/water emulsions as templates. *Inorg. Chem. Comm.* **14,** 1233–1236 (2011).
6. Tan, S. -Y., Tabor, R. F., Ong, L., Stevens, G. W. & Dagastine, R. R. Nano-mechanical properties of clay-armoured emulsion droplets. *Soft Matter.* **8,** 3112–3121 (2012).
7. Aveyard, R., Binks, B. P. & Clint, J. H. Emulsions stabilised solely by colloidal particles. *Adv. Coll. Int. Sci.* **100,** 503–546 (2003).
8. Pickering, S. U. Emulsions. *J. Chem. Soc. Trans.* **91,** 2001–2021 (1907).
9. Ashby, N. P. & Binks, B. P. Pickering emulsions stabilised by Laponite clay particles. *Phys. Chem. Chem. Phys.* **2,** 5640–5646 (2000).
10. Shah, R. K. *et al.* Designer emulsions using microfluidics. *Mater. Today* **11,** 18–27 (2008).
11. Dinsmore, A. D. *et al.* Colloidosomes: selectively permeable capsules composed of colloidal particles. *Science* **298,** 1006–1009 (2002).
12. Dickinson, E. Food emulsions and foams: stabilization by particles. *Curr. Opin. Colloid In. Sci.* **15,** 40–49 (2010).
13. Shilpi, S., Jain, A., Gupta, Y. & Jain, S. K. Colloidosomes: an emerging vesicular system in drug delivery. *Crit. Rev. Ther. Drug Carrier Syst.* **24,** 361–391 (2007).
14. Frelichowska, J. *et al.* Pickering w/o emulsions: drug release and topical delivery. *Int. J. Pharm.* **371,** 56–63 (2009).
15. Langevin, D., Poteau, S., Henaut, I. & Argillier, J. F. Crude oil emulsion properties and their application to heavy oil transportation. *Oil Gas Sci. Tech.—Rev. IFP* **59,** 511–521 (2004).
16. Cayre, O. J. *et al.* pH-responsive colloidosomes and their use for controlling release. *Soft Matter.* **8,** 4717–4724 (2012).
17. Li, J. & Stoever, H. D. H. Doubly pH-responsive pickering emulsion. *Langmuir.* **24,** 13237–13240 (2008).
18. Melle, S., Lask, M. & Fuller, G. G. Pickering emulsions with controllable stability. *Langmuir.* **21,** 2158–2162 (2005).
19. Crossley, S., Faria, J., Shen, M. & Resasco, D. E. Solid nanoparticles that catalyze biofuel upgrade reactions at the water/oil interface. *Science* **327,** 68–72 (2010).
20. Ikem, V. O., Menner, A., Horozov, T. S. & Bismarck, A. Highly permeable macroporous polymers synthesized from pickering medium and high internal phase emulsion templates. *Adv. Mater.* **22,** 3588–3592 (2010).
21. Lee, D. & Weitz, D. A. Nonspherical colloidosomes with multiple compartments from double emulsions. *Small* **5,** 1932–1935 (2009).
22. Shum, H. C. *et al.* Droplet microfluidics for fabrication of non-spherical particles. *Macromol. Rapid Commun.* **31,** 108–118 (2010).
23. Subramaniam, A. B., Abkarian, M. & Stone, H. A. Controlled assembly of jammed colloidal shells on fluid droplets. *Nat. Mater.* **4,** 553–556 (2005).
24. Nudurupati, S., Janjua, M., Aubry, N. & Singh, P. Concentrating particles on drop surfaces using external electric fields. *Electrophoresis* **29,** 1164–1172 (2008).
25. Hwang, K., Singh, P. & Aubry, N. Destabilization of Pickering emulsions using external electric fields. *Electrophoresis* **31,** 850–859 (2010).
26. Nudurupati, S., Janjua, M., Singh, P. & Aubry, N. Effect of parameters on redistribution and removal of particles from drop surfaces. *Soft Matter* **6,** 1157–1169 (2010).
27. Nudurupati, S., Janjua, M., Singh, P. & Aubry, N. Electrohydrodynamic removal of particles from drop surfaces. *Phys. Rev. E* **80,** 010402 (R) (2009).
28. Taylor, G. I. Studies in electrohydrodynamics. I. The circulation produced in a drop by electrical field. *Proc. R. Soc. Lond. A* **291,** 159–166 (1966).
29. Saville, D. A. Electrohydrodynamics: the Taylor-Melcher leaky dielectric model. *Annu. Rev. Fluid. Mech.* **29,** 27–64 (1997).
30. Deegan, R. D. *et al.* Capillary flow as the cause of ring stains from dried liquid drops. *Nature* **389,** 827–829 (1997).
31. Winslow, W. M. Induced fibration of suspensions. *J. Appl. Phys.* **20,** 1137–1140 (1949).
32. Fossum, J. O. *et al.* Intercalation-enhanced electric polarization and chain formation of nano-layered particles. *Europhys. Lett.* **74,** 438–444 (2006).
33. Salipante, P. F. & Vlahovska, P. M. Electrohydrodynamics of drops in strong uniform dc electric fields. *Phys. Fluids* **22,** 112110 (2010).
34. Rozynek, Z. *et al.* Electric field induced structuring in clay–oil suspensions: new insights from WAXS, SEM, leak current, dielectric permittivity, and rheometry. *J. Phys. Condens. Matter* **22,** 324104 (2010).
35. Jones, T. B. *Electromechanics of Particles* (Cambridge University Press, 1995).
36. Subramaniam, A. B., Wan, J., Gopinath, A. & Stone, H. A. Semi-permeable vesicles composed of natural clay. *Soft Matter* **7,** 2600–2612 (2011).

37. Quincke, G. Ueber Rotationen im constanten electrischen Felde. *Ann. Phys. Chem.* **59,** 417–486 (1896).

38. Sapozhnikov, M. V., Tolmachev, Y. V., Aranson, I. S. & Kwok, W. K. Dynamic self-assembly and patterns in electrostatically driven granular media. *Phys. Rev. Lett.* **90,** 114301 (2003).

39. Link, D. R. *et al.* Electric control of droplets in microfluidic devices. *Angewandte Chemie International Edition* **45,** 2556–2560 (2006).

40. Halsey, T. C. Electrorheological fluids. *Science* **258,** 721–834 (1992).

41. Hansen, E. L. *et al.* Swelling transition of a clay induced by heating. *Sci. Rep.* **2,** 618 (2012).

Author contributions

P.D., Z.R. and J.O.F designed all experiments. Z.R., K.H., R.C., K.K. and A.M. performed the experiments. All authors contributed to the data analysis as well as to the presentation of the results. P.D. wrote the initial manuscript and Z.R., A.M., R.C. and J.O.F. all contributed to, and took part in writing and discussions towards, the finalization of the manuscript.

Additional information

Supplementary Information accompanies this paper at http://www.nature.com/naturecommunications

Competing financial interests: The authors declare no competing financial interests.

Reprints and permission information is available online at http://npg.nature.com/reprintsandpermissions/

How to cite this article: Dommersnes, P. *et al.* Active structuring of colloidal armour on liquid drops. *Nat. Commun.* 4:2066 doi: 10.1038/ncomms3066 (2013).
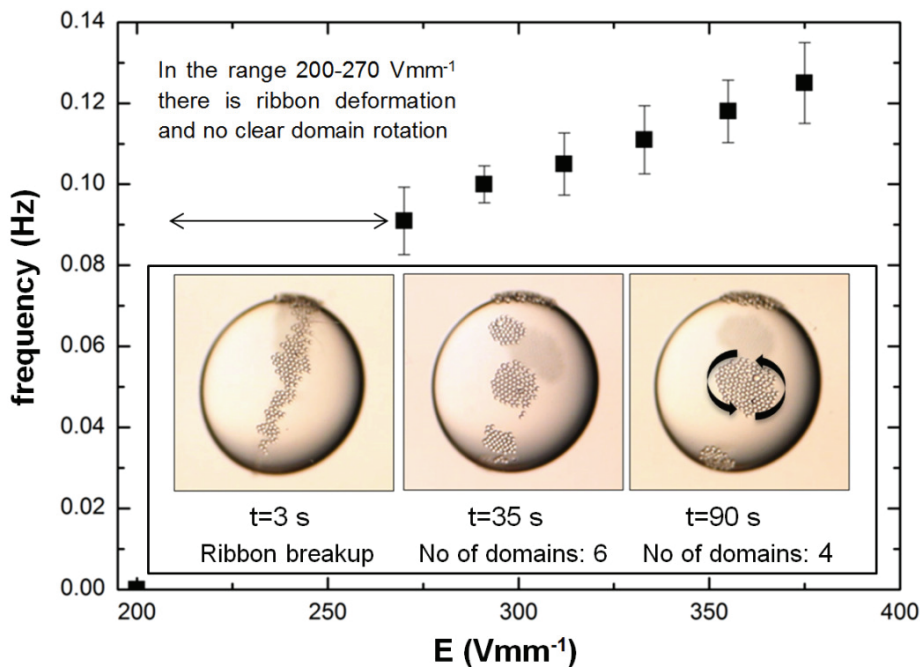
Supplementary Information
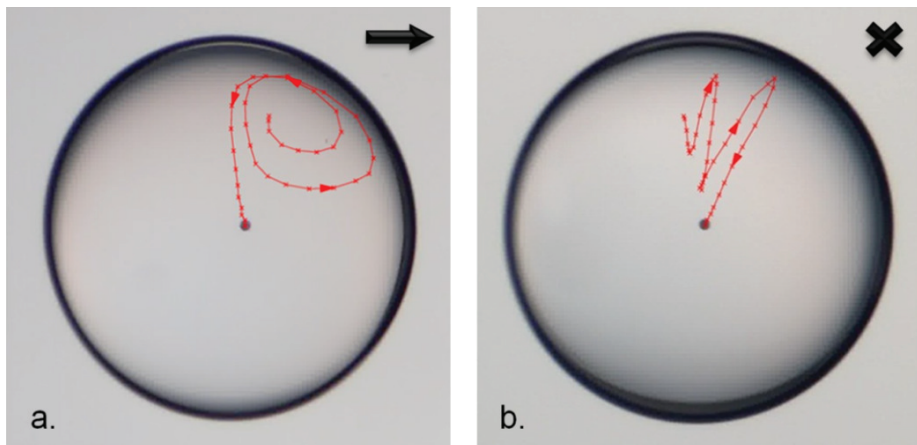
Supplementary Figure S1. Tracing of a particle inside a drop. Silicone drop of radius about 1 mm at E=160 Vmm^{-1} with PE bead used to trace the flow inside the drop. Drop imaged perpendicular (**a**) and parallel (**b**) to the direction of **E**-field. It is seen that the particle follows a spiral motion, i.e. changing between the closed Taylor loop paths as it approaches the drop surface.

No E-field   200 Vmm^{-1} 200 Vmm^{-1}
t=0 min   t=2 min   t=12 min
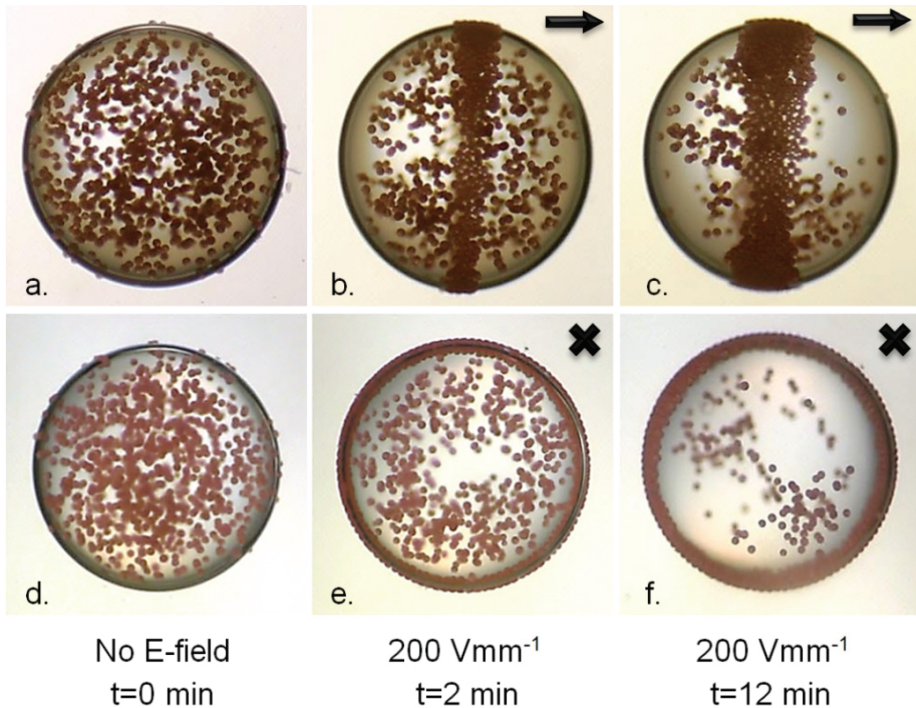
Supplementary Figure S2. Assembly of colloidal polyethylene surface ribbon. A silicone oil drop of radius around 0.75 mm with polyethylene (PE) particles initially dispersed throughout the drop. The drop is immersed in castor oil. The arrows and crosses indicate the direction of the **E**-field. The three upper panels (**a,b,c**) are viewed perpendicular to the **E**-field direction, while the three lower panels (**d,e,f**) are viewed along the **E**-field direction. (**a**) and (**d**) show the situation before the **E**-field is turned on, and (**b,c**) and (**e,f**) after a DC electric field is applied. Hydrodynamic circulation flows are observed in the drop, and after a few minutes a ribbon shaped colloidal monolayer is assembled on the drop surface. A significant number of particles are still carried by the flow in the bulk of the drop. The drop has an oblate deformation.

In the range 200-270 Vmm^{-1} there is ribbon deformation and no clear domain rotation

t=3 s
Ribbon breakup

t=35 s
No of domains: 6

t=90 s
No of domains: 4

Supplementary Figure S3. **Domain rotation frequency versus electric field strength**. At 300 V/mm the rotation frequency is of order of magnitude 0.1 Hz and increases with electric field with a rate of approximately 4×10^{-4} mmV^{-1}s^{-1} (within the range of 275 to 375 Vmm^{-1}). In the range 200 to 270 Vmm^{-1} there is ribbon deformation and the domains are not clearly defined. At even lower fields, i.e. below 200 Vmm^{-1} the ribbon is static. The inset pictures show an example of a droplet with radius about 1 mm with rotating domain structures at different times after the electric field is suddenly increased from 0 to 375 Vmm^{-1} at time t=0. The **E**-field direction is horizontal in the plane of the panels, as indicated by the arrows. This is illustrated in more detail in the Supplementary Movie 3.
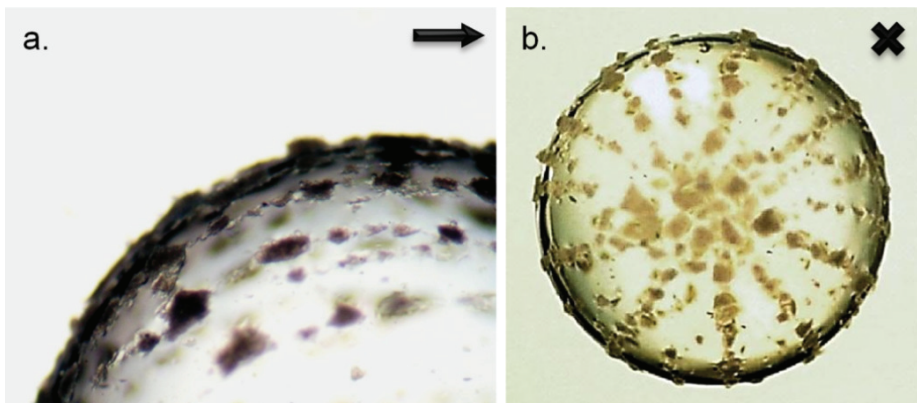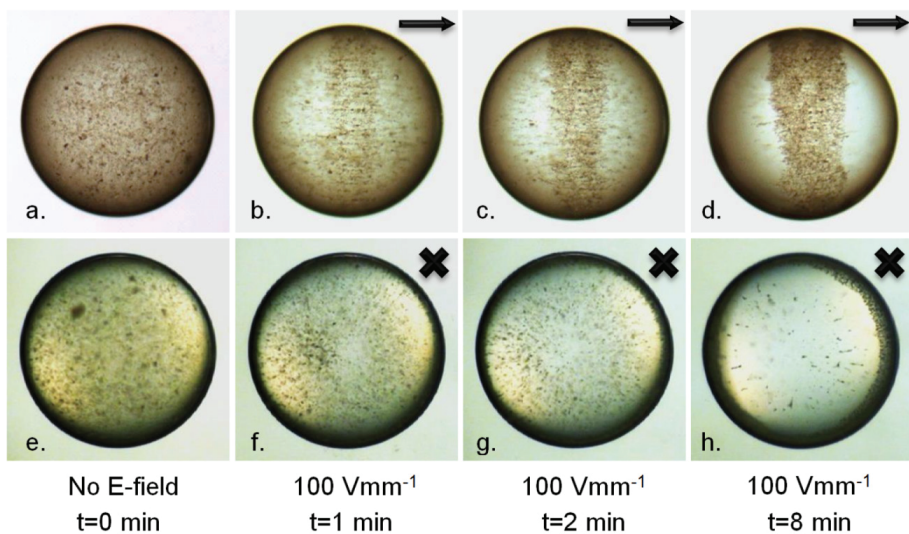
Supplementary Figure S4. Colloidal cage formed by large fluorohectorite clay platelet particles. (**a**) Detail of clay chains on drop surface. (**b**) Clay chain structures seen in the direction of the electric field. The drop radius is about 1 mm and the electric field strength is 250 Vmm^{-1}.
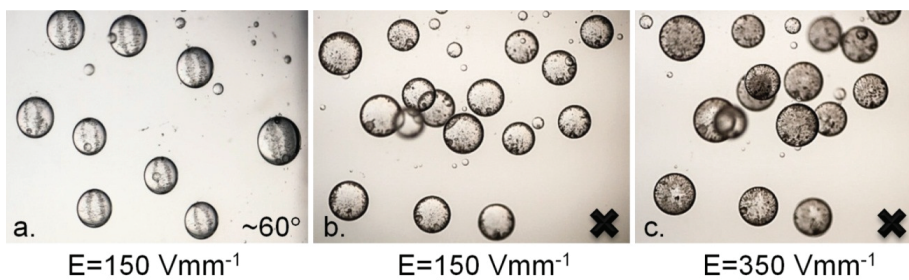
Supplementary Figure S5. Active structuring of colloidal armour on multiple drops. (**a**) Simultaneously formed ribbons of fluorohectorite clay particles at the surface of several silicone oil drops (viewed at an angle ~60° with respect to the direction of electric field). Simultaneous opening (**b**) and closing (**c**) of pupils for multiple drops. The drop radii are in the range of 0.6 to 0.8 mm.
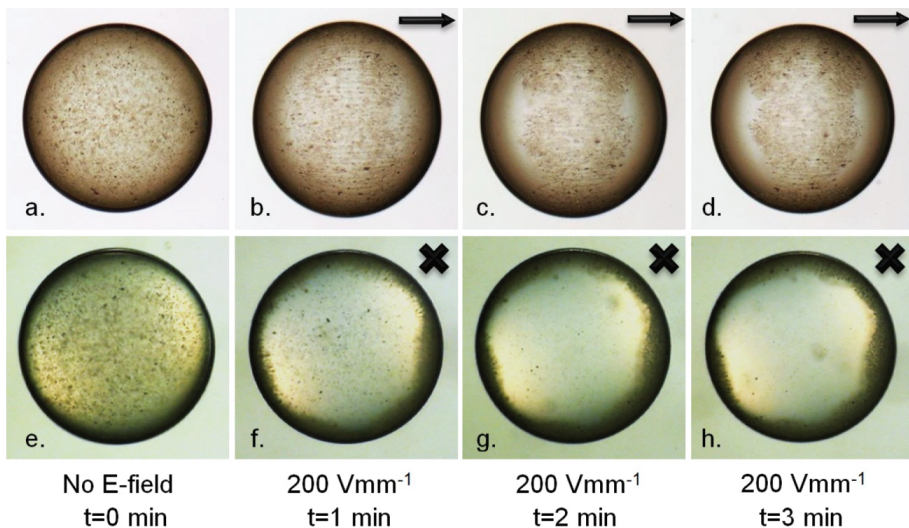
Supplementary Figure S6. Assembly of colloidal clay surface ribbon at at E=200 Vmm⁻¹. A silicone oil drop radius of 0.7 mm with fluorohectorite clay particles initially dispersed throughout the drop. The drop is immersed in castor oil. The arrows and crosses indicate the direction of the **E**-field. The four upper panels (**a,b,c,d**) are viewed perpendicular to the **E**-field direction, while the four lower panels (**e,f,g,h**) are viewed along the **E**-field direction. (**a**) and (**e**) show the situation before the **E**-field is turned on, and (**b,c,d**) and (**f,g,h**) after a DC electric field is applied.

No E-field	100 Vmm^{-1}	100 Vmm^{-1}	100 Vmm^{-1}
t=0 min	t=1 min	t=2 min	t=8 min

Supplementary Figure S7. Assembly of colloidal clay surface ribbon at *E*=100 Vmm^{-1}. The panel description is identical to the description in Supplementary Figure S6. In this case however, the time scale of the ribbon formation is significantly slower due to the lower electric field strength.
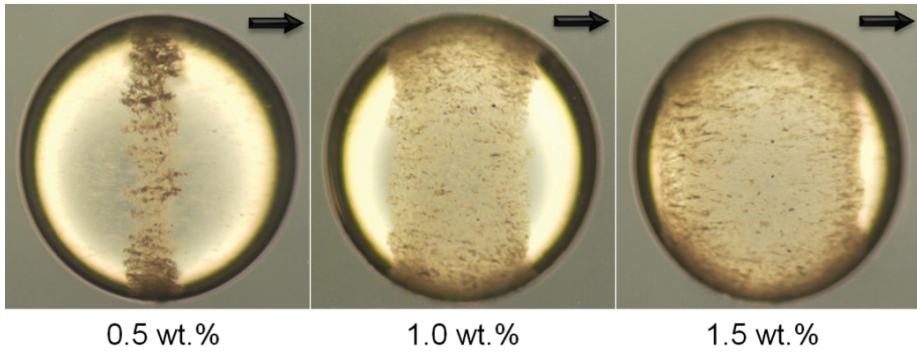
Supplementary Figure S8. Ribbon width as a function of clay concentration. For higher colloidal concentration, the ribbon becomes wider. The drop radius is about 1 mm. The **E**-field direction is horizontal in the plane of the panels, as indicated by the arrows.
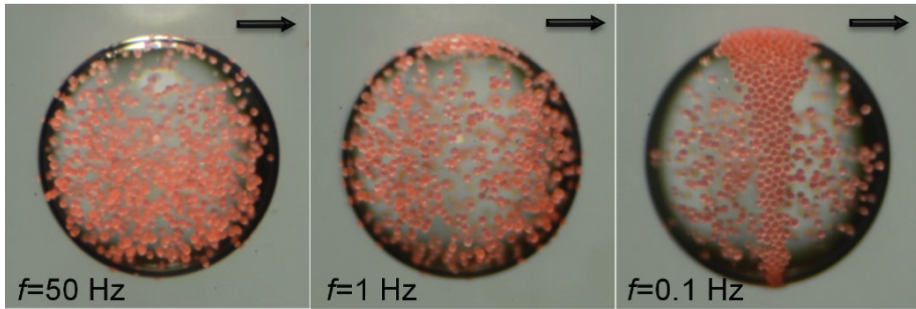
Supplementary Figure S9. Ribbon formation of PE beads at various AC field frequencies. Silicone drop of radius about 0.5 mm with PE beads in AC field at different frequencies, f. The **E**-field direction is horizontal in the plane of the panels, as indicated by the arrows.

Clay mineral	Kaolinite	Quick clay	Halloysite	Vermiculite	Na-MMT	Fe-Fh	Cu-Fh	Li-Fh	Laponite
Supplementary Table S1. **Pupil formation related to electrical conductivity.** The relative electrical conductivities of different clay powders are normalized to that of Kaolinite ($\sim 2\times 10^{-6}$ Sm^{-1}). Only clay minerals with high conductivity values display active pupil-like formation.									
Relative conductivity	1.0	1.2 ± 16 %	1.9 ± 21 %	2.7 ± 33 %	3.0 ± 27 %	12.6 ± 17 %	17.0 ± 24 %	42.6 ± 26 %	89.6 ± 28 %
Pupil formation	No	No	No	No	No	Yes	Yes	Yes	Yes